Measurement of neutron production in the very forward rapidity at LHC $\sqrt{s} = 7$ TeV p-p collision

Kentaro KAWADE

Division of Particle and Astrophysical Science,
Graduate School of Science,
Nagoya University

Abstract

Ultra-high-energy cosmic-rays "UHECRs" were observed indirectly, and their primary properties are determined by Monte Carlo simulations with hadronic interaction models. However, uncertainty of the hadronic interaction models due to lack of calibration data at energy near UHECR is associated with the large uncertainty of cosmic-ray observations. Therefore, the hadronic interaction models must be calibrated by using high energy accelerators.

The Large Hadron Collider forward (LHCf) experiment was designed to verify the hadron interaction models by using the LHC. Because the LHCf detectors were optimized to measure electro-magnetic showers, the performance of the LHCf detectors for hadron shower measurement has not been studied in detail yet. In order to measure forward neutron spectra, the performance of LHCf detectors for hadron showers was evaluated by using Monte Carlo simulations and 350 GeV test beam protons at CERN-SPS for the first time. The detection efficiency was estimated to be from 70% to 80% for neutrons with the energy from 500 GeV to 3.5 TeV. About 40% of energy resolution with less than 2% of energy scale non-linearity were achieved. The position resolutions varied from 1.3 mm to 0.3 mm depending on the incident neutron energy. The absolute energy scale was carefully checked with 3.5% accuracy at 350 GeV using SPS test beams.

In order to extract the true energy distribution from the measured energy spectra, the performance of the multi-dimensional unfolding method was studied. We confirmed that the true energy distribution can be reconstructed with 20-60% accuracy depending on the energy by the unfolding method.

Owing to the hadron shower reconstruction methods newly developed in this study, the analysis of forward neutron spectra using LHC $\sqrt{s} = 7$ TeV p-p collision data taken in May 2010 was carried out. The neutron energy spectra were measured in three different pseudo-rapidity η regions of from 8.81 to 8.99, from 8.99 to 9.22, and from 10.76 to infinity. The experimental results were compared with the MC predictions from known hadronic interaction models of DPMJET 3.04, EPOS 1.99, PYTHIA 8.145, QGSJET II-03 and SYBILL 2.1. No model could reproduce the experimental result perfectly. The experimental results show the most abundant neutron production compared to the known models.

The performance of the LHCf detectors for neutron measurement has been confirmed in this study for the first time. It was also demonstrated that it is possible to verify the hadronic interaction models using the neutron energy spectrum obtained by LHCf.

Contents

Chapter 1

Physics backgrounds

1.1 cosmic-ray observation

Cosmic-rays are very high energetic particles from somewhere in the universe. Since Victor Franz Hess had found cosmic-rays in 1912, various observations have measured cosmic-rays for a long time. The properties of cosmic-rays have been one of the interesting topics since then. For instance, their energy, chemical composition, and arrival direction are keys to understand cosmic-ray properties. With 100 years of measurements, the nature and sources of cosmic-rays have been studied. The energy spectrum of cosmic-ray is plotted for energy above 10^8 eV in Figure 1.1 [1]. The energy spectrum steepens around 10^{15} eV and flattens around $10^{18.5}$ eV again. The former structure is called as the "knee" and the latter is called as the "ankle". The differential flux of cosmic-rays can be described by Equations 1.1,

$$\frac{dN}{dE} \propto \begin{cases} E^{-2.7} & (E < E_{knee}) \\ E^{-3.0} & (E_{knee} < E < E_{ankle}) \\ E^{-2.7} & (E_{ankle} < E). \end{cases} \tag{1.1}$$

Here E_{knee} and E_{ankle} are the energies at the knee and the ankle, respectively. The energy of cosmic-rays ranges from sub-MeV to more than 100 EeV. The differences in the index of cosmic-ray flux indicate a change of its origin. For example, Super Nova Remnants (SNRs) [2] are candidates of the origin for cosmic-rays below $10^{15.5}$ eV, and gamma ray bursts (GRBs) or Active Galactic Nuclei (AGNs) are candidates for cosmic-rays below $10^{18.5}$ eV. However, the origin and acceleration mechanism of ultra high energy cosmic-rays (UHECRs) having the energies more that 10^{18} eV are unsolved problems.

The techniques of measurement are different depending on target energies. A direct measurement with balloons or satellites is sufficient for cosmic-rays

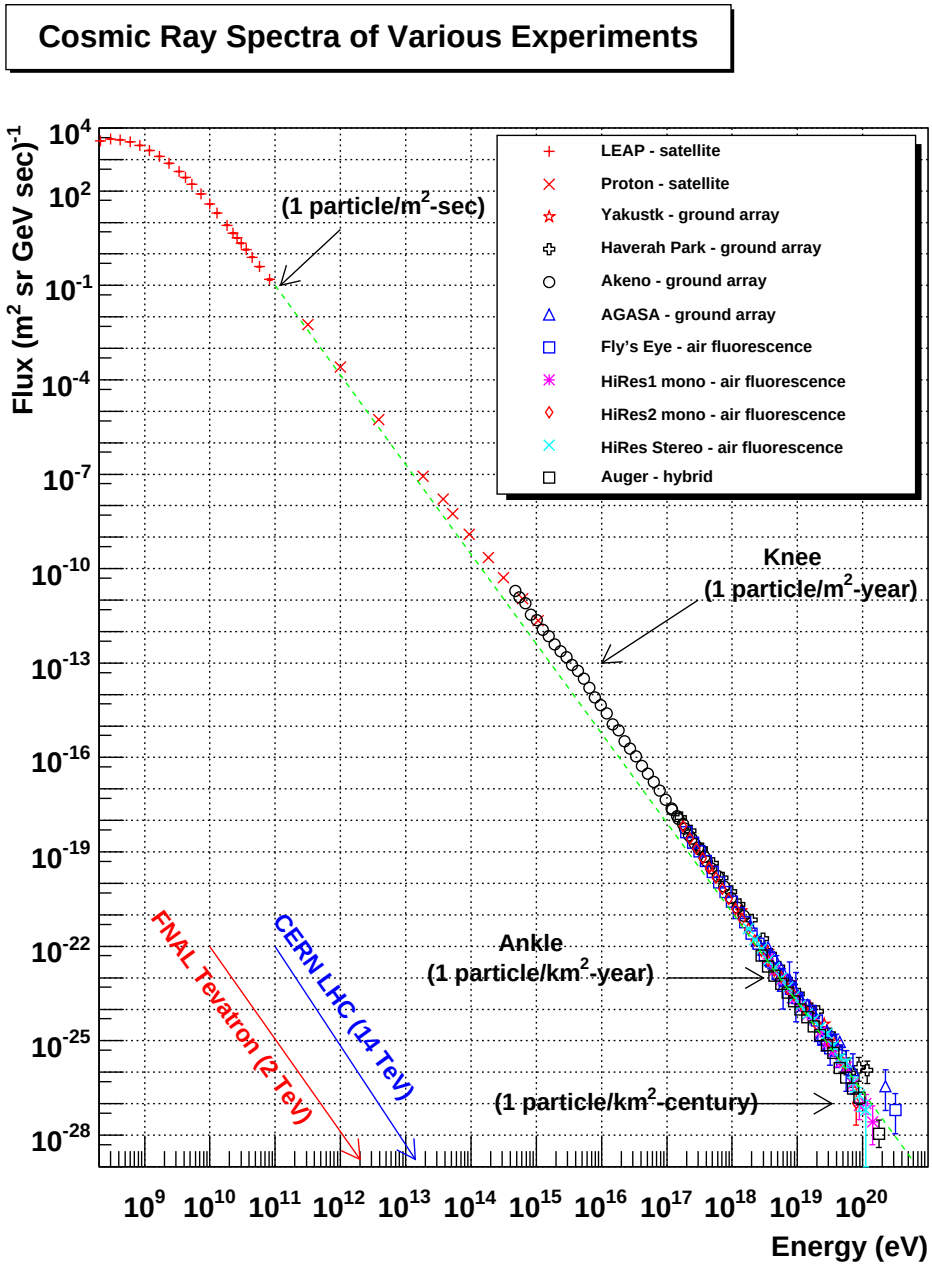

Figure 1.1: The energy spectra of cosmic-rays measured by various experiments [1].

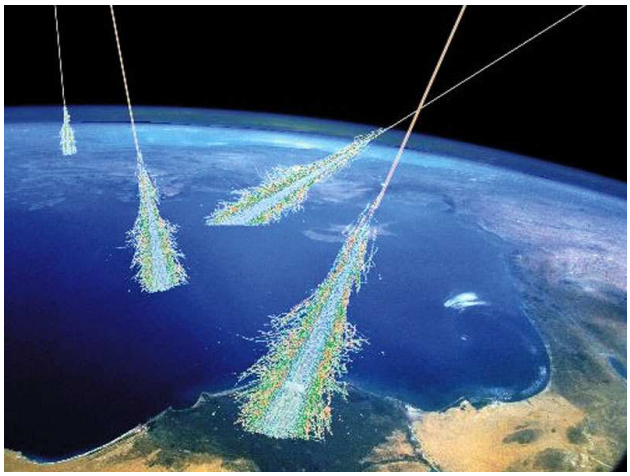

Figure 1.2: A schematic picture of cosmic-ray showers [3].

with energy below 10^{14} eV. The flux of UHECRs is quite low. For example, the flux is 1/km^2/year at 1020eV, whereas 1 particle/cm^2/sec at 100 MeV. It is no longer possible to measure UHECR directly. Therefore, an indirect measurement is the only capable to measure UHECRs. The UHECRs develop very large cascade showers associated with the interaction with atmospheric particles. Because the cascade shower widely spreads by a few km^2 and reaches the ground, UHECR can be observed indirectly as secondary particles by using ground base detectors. Figure 1.2 shows a schematic picture of cosmic-ray showers. There are mainly two types of detector to measure the showers from UHECRs. One is a surface array detector (SD) and the other is a florescence detector (FD). SD consists of a number of particle detectors which measure muons or charged particles generated by UHECRs. FD is optical telescopes and able to observe atmospheric florescence. At the present time, the Pierre AUGER Observatory (PAO) [4] and the Telescope Array (TA) experiment [5] are observing UHECRs with the hybrid technique of the SDs and the FDs.

Primary information of UHECRs, such as energy and chemical composition, are reconstructed from the observed secondaries by using simulations with hadronic interaction models. However, validity of these models is not sufficient at the energy region of UHECRs up to 10^{20} eV, because there is no calibration data at this energy region so far. It associates large uncertainty to the estimation of the energies and chemical compositions of UHECRs. Figure 1.3 shows the energy spectra of cosmic-rays of the energies more than 10^{18} eV measured by the PAO and the HiRes experiment which had a very

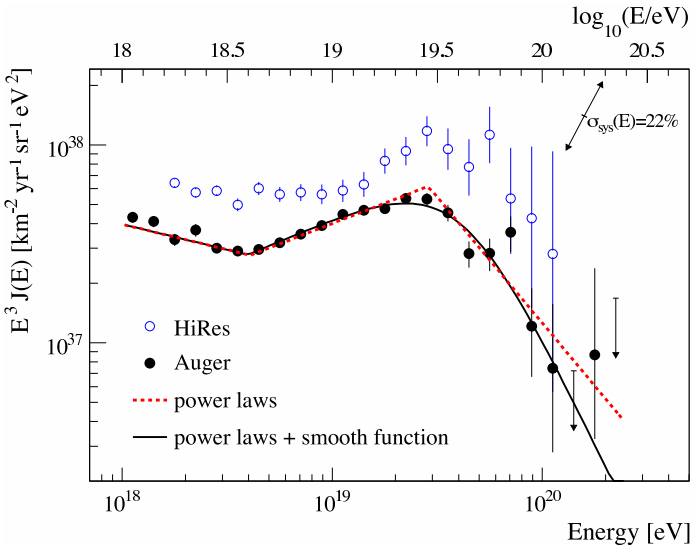

Figure 1.3: The energy spectra of cosmic-rays above 10^{18} eV measured by several experiments [6]. A cutoff around $10^{19.5}$ eV is a candidate of the predicted cut-off called GZK cutoff around this energy region. The arrows indicate the systematic uncertainty of the flux scaled by E^3 owing to the 22% of energy scale uncertainty.

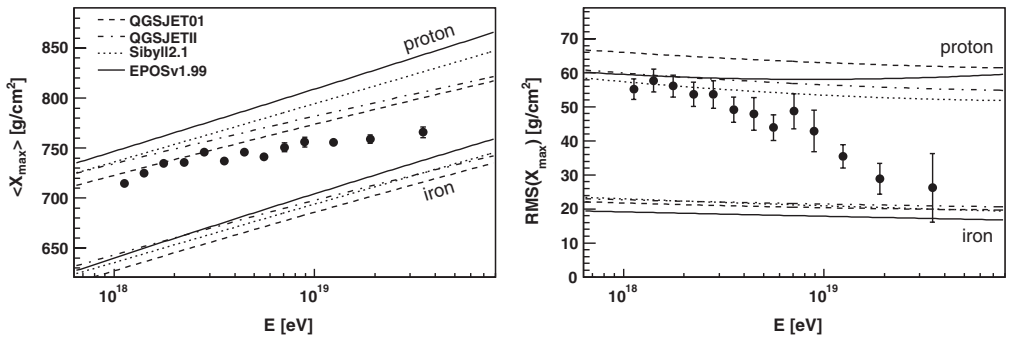

Figure 1.4: Left and right panels show the average X_{max} $\langle X_{max} \rangle$ and average rms X_{max} distributions as a function of reconstructed primary energy, respectively [10]. The lines show the predictions using different hadronic interaction models and different compositions (proton or iron).

large FD detector [7]. The arrows indicate the systematic uncertainty of the flux scaled by E^3 owing to the 22% of energy scale uncertainty. Systematical difference between the two experiments is partly explained by the uncertainty of the hadronic interaction models. Cosmic-ray protons cannot travel more than 40 Mpc (mean free path), because they effectively lose their energy by the interaction with the cosmic microwave background (CMB) photons as shown in following,

$$p + \gamma(\mathrm{CMB}) \rightarrow \Delta(1232) \rightarrow \begin{cases} p + \pi^0 \\ n + \pi^+. \end{cases} \tag{1.2}$$

A cut-off around $10^{19.5}$ eV is predicted and called Greisen-Zatspin-Kuzumin (GZK) cut-off [8, 9]. On the other hand, extremely high energy heavy ions also lose their energy due to the interactions with CMB photons such as photo-dissociation and cannot travel for a long distance.

Figure 1.4 shows the longitudinal development of cosmic-ray showers measured by the PAO and the HiRes experiment [10]. Left and right panels show the distribution of average X_{max} $\langle X_{max} \rangle$ and average rms of X_{max} as a function of reconstructed primary energy, respectively. Here X_{max} represents the atmospheric depth at which number of shower particles reaches the maximum and sensitive to the mass of the primary particle. The lines show predictions using different hadronic interaction models for different compositions (a proton or an iron). There are considerable differences among the model for predictions.

1.2 Hadronic interaction model

Forward particle production in high-energy particle collision is one of the unknown phenomenon and is important process in the development of cosmic-ray showers. Most of the particles emitted at the forward region are generated from the result of soft QCD process. QCD involves hard and soft type processes. Soft process occur when momentum transfer (Q^2) is very small ($Q^2 < 1GeV$), while hard process occur when Q^2 greater than 1 GeV. Because the coupling constant of the strong interaction diverges in the collision with very low Q^2, production of forward particles can not be calculated by the perturbation QCD theory. Therefore, phenomenological models based on the Gribov-Regge theory [11, 12] (GRT) that describes soft and semi-hard processes are very important to describe the particle production at very forward rapidity and a brief explanation is given in the next chapter. There are several interaction models frequently used in cosmic-ray observations and high energy experiments, DPMJET 3.04 [13], EPOS 1.99 [14], PYTHIA 8.145 [15, 16], QGSJET II-03 [17], and SYBILL 2.1 [18].

Measurement of forward particle production using high energy collider can provide quite important information to verify the hadronic interaction models and to understand the development of cosmic-ray showers. The key parameters of the hadronic interaction to describe the development of cosmic-ray shower are 1) the total inelastic cross section σ_{inel}, 2) the secondary particles spectra, and 3) the inelasticity k. The total cross section was measured precisely as $73.5 \pm 0.6(stat)^{+1.8}_{-1.3}(syst)$ mb by the TOTEM (TOTal Elastic and diffractive cross section Measurement) experiment [19, 20]. The secondary particle spectra can be measured by forward detectors. k is the fraction of energy of the primary cosmic-rays used to generate secondary particles and can be directly measured by the measurement of the forward leading baryon that provides $1 - k$, or elasticity.

The dependence of Mean X_{max} and rms X_{max} on the parameters were studied in [21]. Figure 1.5 shows the impact of change in hadronic interaction features on X_{max}. Upper panels show the mean X_{max} and rms X_{max} dependence on the interaction parameters (cross section, multiplicity, elasticity and charge ratio), respectively. Left and right panels correspond to proton and iron primaries, respectively. Horizontal axes f_{19} are the energy dependent re-scale parameters and modified factor $f(E, f_{19})$ is defined as,

$$f(E, F_{19}) = 1 + (f_{19} - 1)F(E), \tag{1.3}$$

with,

$$F(E) = \begin{cases} 0 & (E \leq 1PeV) \\ \frac{\log_{10}(E/1PeV)}{\log_{10}(10EeV/1PeV)} & (E > 1PeV). \end{cases} \tag{1.4}$$

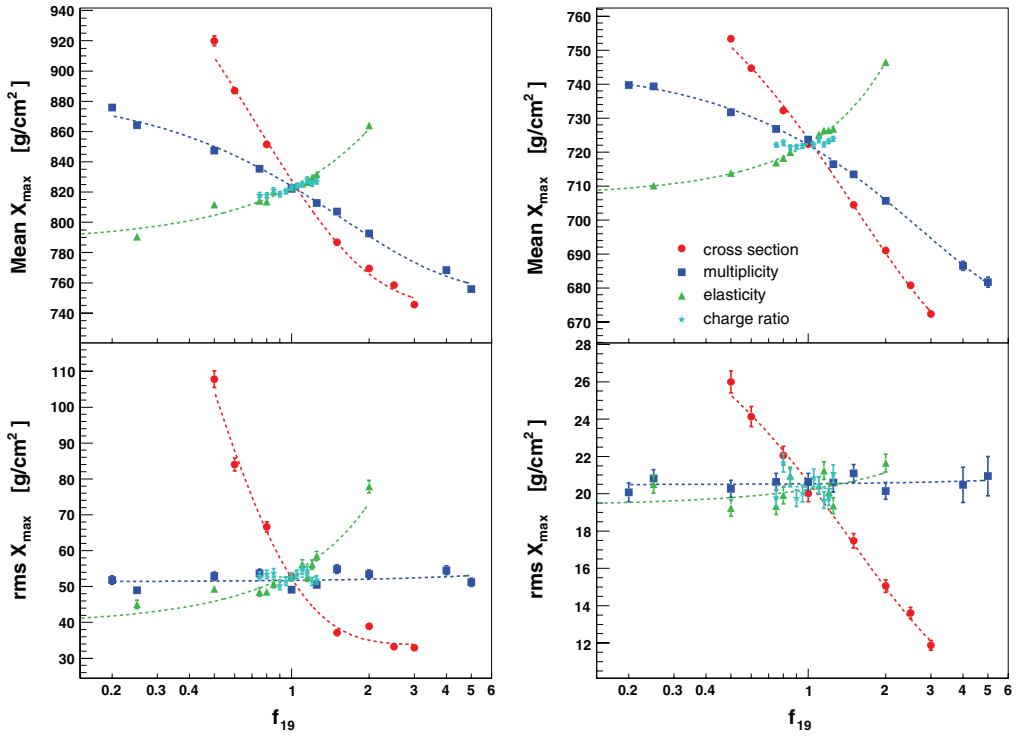

Figure 1.5: Impact of hadronic interaction features on X_{max} [21]. Upper panels show the mean X_{max} dependence and rms X_{max} dependence on the interaction parameters (cross section, multiplicity, elasticity and charge ratio), respectively. Left and right panels correspond to proton and iron primaries.

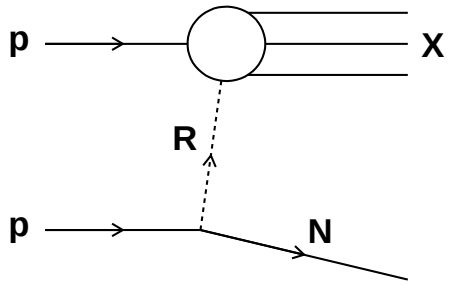

Figure 1.6: A diagram of neutron production process at proton-proton collisions in the Regge theory. p represent protons and R indicates a Regge trajectory [11, 12].

The factor $f(E, f_{19})$ is 1 at energy below 10^{15} eV (without modification). On the other hand at energy above 10^{15} eV, the deviation of $f(E, f_{19})$ from 1 increases logarithmically with energy and reach the value of f_{19} at 10^{19} eV.

Forward baryons are one of the particles generated in high energy particle collisions mainly by the fragmentation process. They play a very important roll in the development of cosmic-ray showers. Figure 1.6 shows a schematic diagram of neutron production process by the Reggeon exchange model. For instance, if forward baryons have more energy after collisions, cosmic-ray showers can penetrate deeply in the atmosphere, or if less energy, the showers can develop rapidly. However, the predictions of forward baryon production at the forward rapidity are quite different among the models due to the lack of the calibration data at the energy near UHECRs.

The muon excess is one of problems on the air shower observations. The number of muons observed by the surface detector array of the PAO is higher than the expected number that obtained using the energy determined by the FD observation with current hadronic interaction models [22]. It was suggested that the number of (anti-)baryons generated to the forward region is strongly related to the number of muons observed at the ground [23].

Therefore baryon productions in the very forward region is quite important to understand behavior of cosmic-ray showers. However, it is difficult to measure hadronic showers at the very forward region of high energy collider due to the limitation of experimental space. The detailed understand of MC simulation is also very important to estimate the detector performance for hadronic showers.

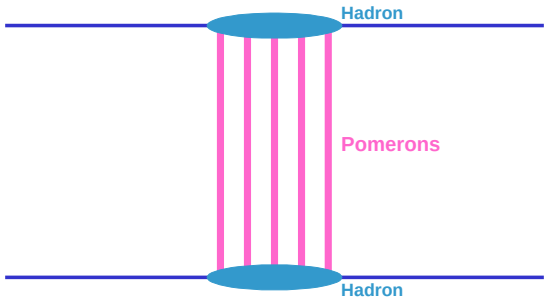

Figure 1.7: Hadron-hadron interaction in the GRT. The horizontal lines represent incoming hadrons. Each vertical line represents a Pomeron.

1.2.1 The Gribov Regge theory

The Gribov Regge theory (GRT) [24] describes multiple particle scattering by exchanging the phenomenological objects called "Pomerons". Hadron-hadron interaction in the GRT can be represented as Figure 1.7. The horizontal blue lines represent incoming hadrons, and the vertical lines correspond to Pomerons. Multiple Pomeron interactions can be occur in the GRT. The fundamental nature of Pomeron is not known and parametrized by simple parameters such as cross section which tuned by the experiment. A disadvantage of GRT is the fact that being not able to calculate cross section and particle production consistently. In order to calculate particle production, it is necessary to know how to share the energy between the multiple interactions (in case of multiple scattering). The energy conservation is not taken into account in calculation of the cross section. As another disadvantage of GRT, it is difficult to include hard QCD scattering which usually treated by the parton model.

On the other hand, the "Parton" model describe hadron-hadron hard interaction and be able to calculate the inclusive production cross section of parton jets. However, the Parton model can not predict individual interactions exclusively.

To solve these problems, the Parton-based Gribov Regge Theory which can treat consistently the cross section calculation and particle production considering energy conservation and hard scatterings was introduced. Figure 1.8 represents the schematic diagram of hadron-hadron interaction in the parton based GRT. Each small cyan circle indicates nucleon and each thin blue splitting line form nucleon shows constituent. Each thick vertical line represents a Pomeron.

Although there are some interaction models based on the Parton-based GRT such as QGSJET II-03 and EPOS 1.99, the computation of a cross-

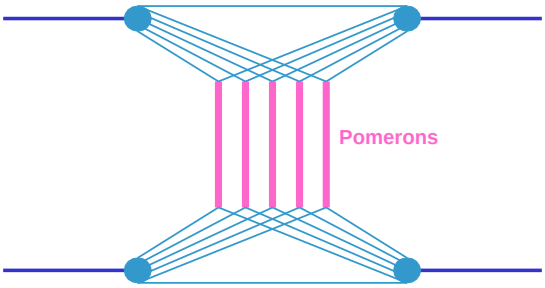

Figure 1.8: Hadron-hadron interaction in the parton based GRT. Each small circle indicates nucleon and each thin blue splitting line form nucleon shows constituent. Each thick vertical line represents a Pomeron.

section for each interaction and the amplitudes of generated particles depend on the models. Moreover, the treatment of the experimental calibration data is different among the models. The extrapolation of the interaction models to ultra high energy is strongly depend on the model, and therefore it is important to verify the model by high energy experiments.

1.3 Forward hadron measurements

Here, several forward hadron measurements previously carried out by other experiments are briefly introduced. Figure 1.9 shows the x_F distributions of forward neutrons measured by the PHENIX experiment at the $\sqrt{s} = 200$ GeV p-p collisions at the Relativistic Heavy Ion Collider (RHIC), and the ISR experiment at the $\sqrt{s} = 30.6$ to 62.7 GeV p-p collisions at the intersecting storage ring (ISR) [25, 26, 27] at the forward region. The black and the red markers correspond to the PHENIX results assuming two different p_T distributions of exponential (black) or Gaussian (red), while the colored lines correspond to the ISR results. The x_F is defined by,

$$x_F = p_L/p_{L(max)} = E_n \cos\theta_n / E_p. \tag{1.5}$$

Here p_L is the longitudinal momentum of the neutron, E_n and E_p are energies of the neutron and the proton beam, and θ_n is the polar angle of the neutron along the beam direction. The peak around $x_F = 0.8$ can be recognized in the results of both the experiments. The absolute normalization uncertainties for the PHENIX and the ISR are 9.7% and 20%, respectively. This results are indicating that the x_F distribution does not depend on the energies in these energy region (Feynman x_F scaling). It is also an interesting point that the x_F scaling is also recognized at the LHC energy.

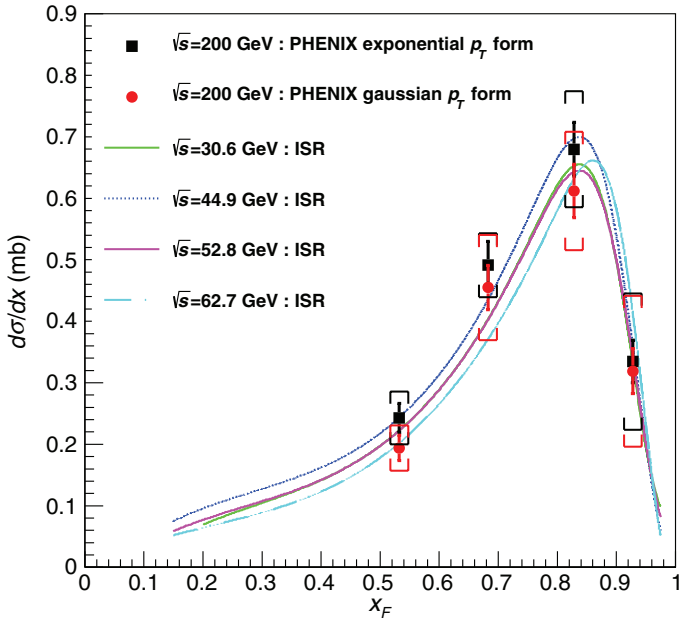

Figure 1.9: The x_F distribution of forward neutrons measured by the PHENIX experiment and the ISR experiment [25, 26, 27].

On the other hand, several forward experiments in the LHC accelerator cover the wide rapidity ranges. The Forward Hadron Calorimeters (HFs) at the CMS experiment [28] that cover the pseudo-rapidity range $3 < \eta < 5$ measure forward jets generated from the LHC collisions by using Cherenkov detectors. The CASTOR Calorimeter at the CMS experiment [29] which covers the very forward region $-6.6 < \eta < -5.2$ also measure forward particles by using a Cherenkov sampling calorimeter. The Zero Degree Calorimeters (ZDCs) and the LHCf detectors installed at zero degree collision angle cover the pseudo-rapidity range $\eta > 8.4$.

Chapter 2

The LHCf experiment

2.1 The Large Hadron Collider

The Large Hadron Collider (LHC) [30] is the largest and the highest-energy particle collider in the world. The LHC accelerator is designed to a proton-proton collider with $\sqrt{s} = 14$ TeV. The LHC main rings are contained in the circular tunnel built about 100m underground with a circumference of 26.7km as shown in Figure 2.1. The tunnel built near the boarder between Switzerland and France contains two parallel beam pipes containing the beams circulating in the opposite directions.

The designed operation parameters are summarized in Table 2.1 . Proton beams injected from the Linac2 are accelerated by the Proton Synchrotron Booster, the Proton Synchrotron (PS) and the Super Proton Synchrotron (SPS) from 50 MeV to 450 GeV. Then protons are injected to the LHC rings and accelerated up to 7 TeV. The bunches of proton-beams cross at four Interaction Points (IPs) of IP1, IP2, IP5 and IP8 and provide $\sqrt{s} = 14$ TeV proton-proton collisions at maximum. The designed maximum energy of the LHC $\sqrt{s} = 14$ TeV corresponds to 10^{17} eV at the laboratory frame.

2.2 The LHCf experiment

The Large Hadron Collider forward (LHCf) experiment was designed to use the LHC to verifying the hadronic interaction models used in cosmic-ray physics [31, 34]. It was designed to measure particles emitted in the very forward region of the LHC and to take data at very low luminosity operation with less than 10^{30} cm^{-2}s^{-1}. Thus, the LHC provide us very good opportunity to calibrate the hadronic interaction model at the energy near UHECRs. The locations where the LHCf detectors were installed covered a

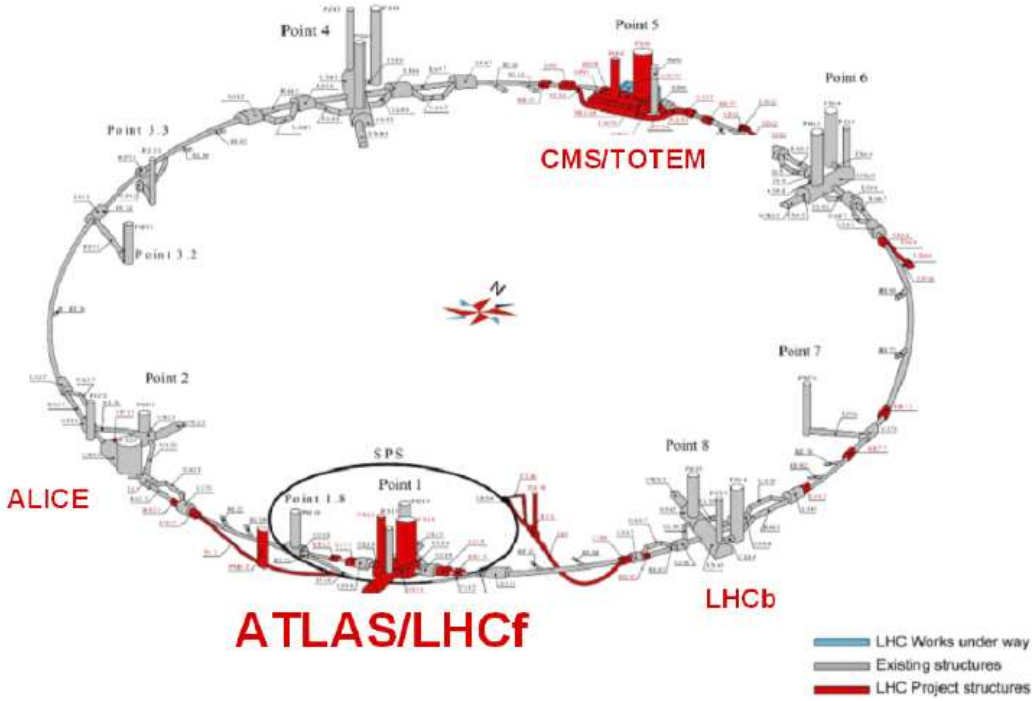

Figure 2.1: The layout of the LHC ring. The circumference is 26.7km. There are 4 interaction points and 7 experiments.

	Designed value	Early 2010 (During LHCf operation)
Circumference	26.7km	-
Number of superconducting dipoles	1232	-
Magnetic field	8.33 Tesla	4.16 Tesla
Total current	11.85 kA	5.93 kA
Beam energy	7 TeV	3.5 TeV or 0.45 TeV
Luminosity	10^{34} cm^{-2}s^{-1}	$<10^{30}$ cm^{-2}s^{-1}
Number of bunches per beam	2808	≥ 43
Number of protons per bunch	10^{11}	10^{10}
Bunch spacing	25 ns	>2 μs
Bunch size at IP	16.7 μm	-
Bunch length at IP	77 mm	-

Table 2.1: LHC beam parameters of the designed values and the values at the LHCf operations.

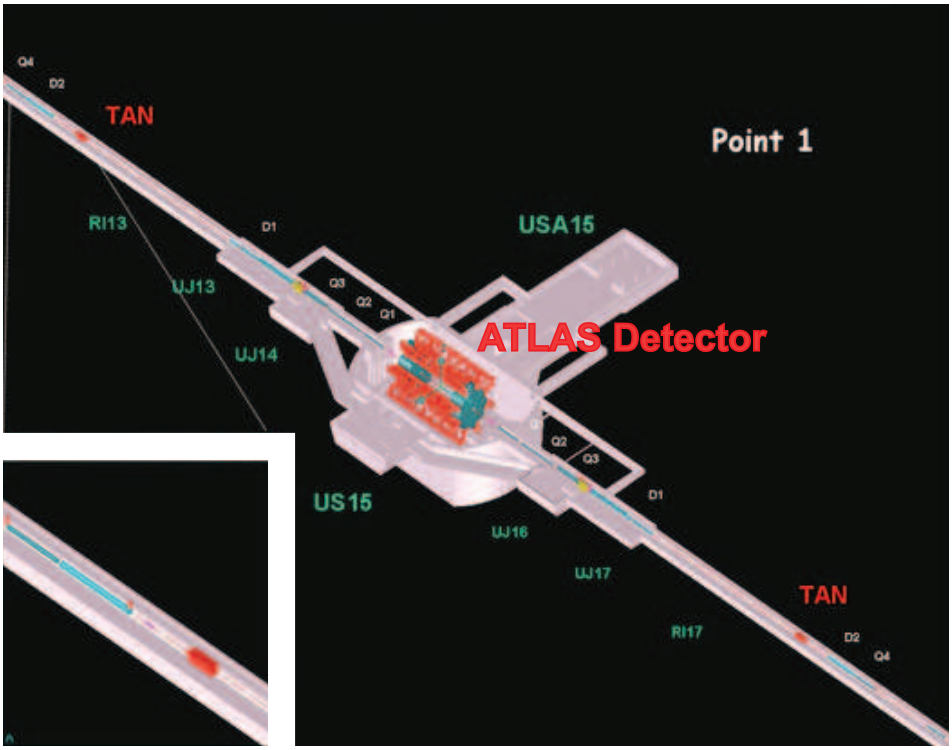

Figure 2.2: Geometrical view around the IP1 of LHC. The LHCf detectors are installed at the place indicated as TAN at the both sides of IP1.

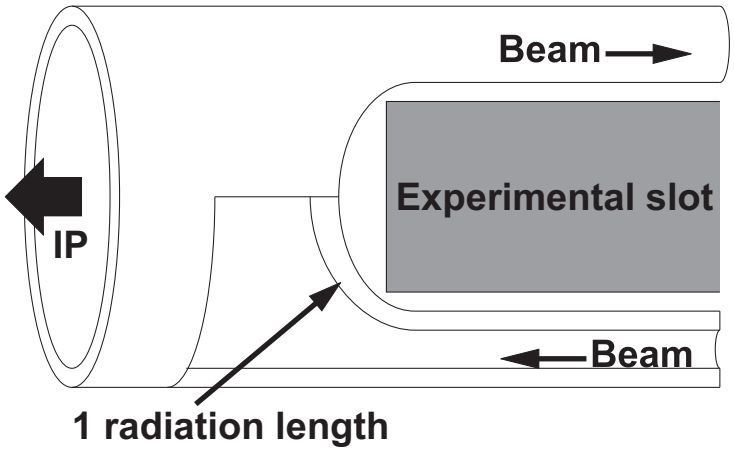

Figure 2.3: The schematic picture of the detector installation slot in the TAN. The LHCf detectors were installed in this experimental slot.

pseudo-rapidity range from 8.7 to ∞. Here, pseudo-rapidity η is defined as following equation,

$$\eta = -\ln(\tan\frac{\theta}{2}). \tag{2.1}$$

The pseudo-rapidity coverage of LHCf can be extended to 8.4 in case of the operation with the maximum beam crossing angle. Only neutral particles can reach the LHCf detectors, because charged particles which produced at the IP1 and thrown towards TANs (Neutral Beam Absorbers) are swept aside by the inner beam separation dipole (D1 magnet) before reaching the TANs. Figure 2.3 shows the schematic geometry of a small detector installation slot inside the TANs. The LHCf detectors were installed behind the beam pipe wall equivalent to 1 radiation length.

Figure 2.4 shows the particle distribution and energy flux as a function of pseudo-rapidity η at $\sqrt{s} = 14$ TeV proton-proton collisions. The dashed lines indicate neutral particles, while the solid lines indicate all the particles. The colored bands indicate the coverage of several experiments.

The first LHCf physics data taking was performed at $\sqrt{s} = 900$ GeV proton-proton collisions in the end of 2009. Then LHCf successfully carried out physics data taking at $\sqrt{s} = 7$ TeV proton-proton collisions in 2010. LHCf has already published the photon and the π^0 spectra at 7 TeV proton-proton collisions [36, 37] and the photon spectra at 0.9 TeV proton-proton collisions [38].

For the next operations, LHCf plans to take data at $\sqrt{s} = 13$ TeV proton-proton collisions after 2015. The LHCf detectors are now upgrading by using

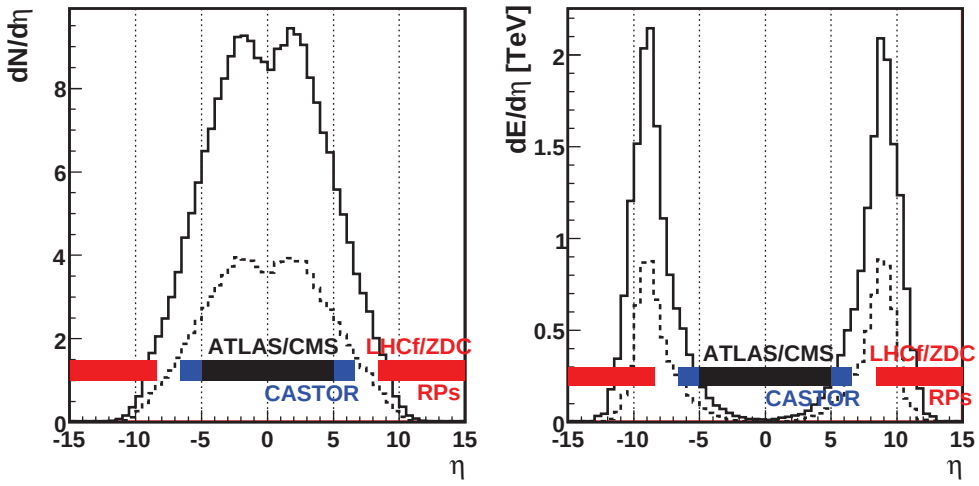

Figure 2.4: Particle distribution as a function of pseudo-rapidity η. Left shows the multiplicity and right shows energy flux for charged+neutral particles (solid) and neutral particles (dashed).

GSO scintillators [39] to improve the radiation hardness for the 13 TeV operation, because higher radiation dose is estimated.

2.3 The LHCf detectors

Two independent detectors named "Arm1" and "Arm2" were installed in TANs located at both sides of 140m away from the IP1. The Arm1 detector was installed in counter-clockwise direction from the IP1 (IP8 side), while the Arm2 detector was installed at opposite direction (IP2 side). Both the detectors have two different tower shape calorimeters. Each calorimeter consists of sampling and imaging calorimeter composed of 16 layers of tungsten absorber, 16 sampling layers of 3 mm thick plastic scintillators and 4 layers of transverse position sensitive detectors. The transverse sizes of small and large calorimeter, small tower and large tower hereafter, were 20 mm $\times$ 20 mm and 40 mm $\times$ 40 mm for Arm1, and 25 mm $\times$ 25 mm and $\times$ 32 mm $\times$ 32 mm for Arm2. The small tower calorimeters were designed to cover the zero degree collision angle. Upper and bottom of Figure 2.5 show the transverse cross section of the Arm1 and Arm2 detectors, respectively. The blue ellipses indicate the elliptical beam pipe located in the dipole magnets 55m far from the TAN.

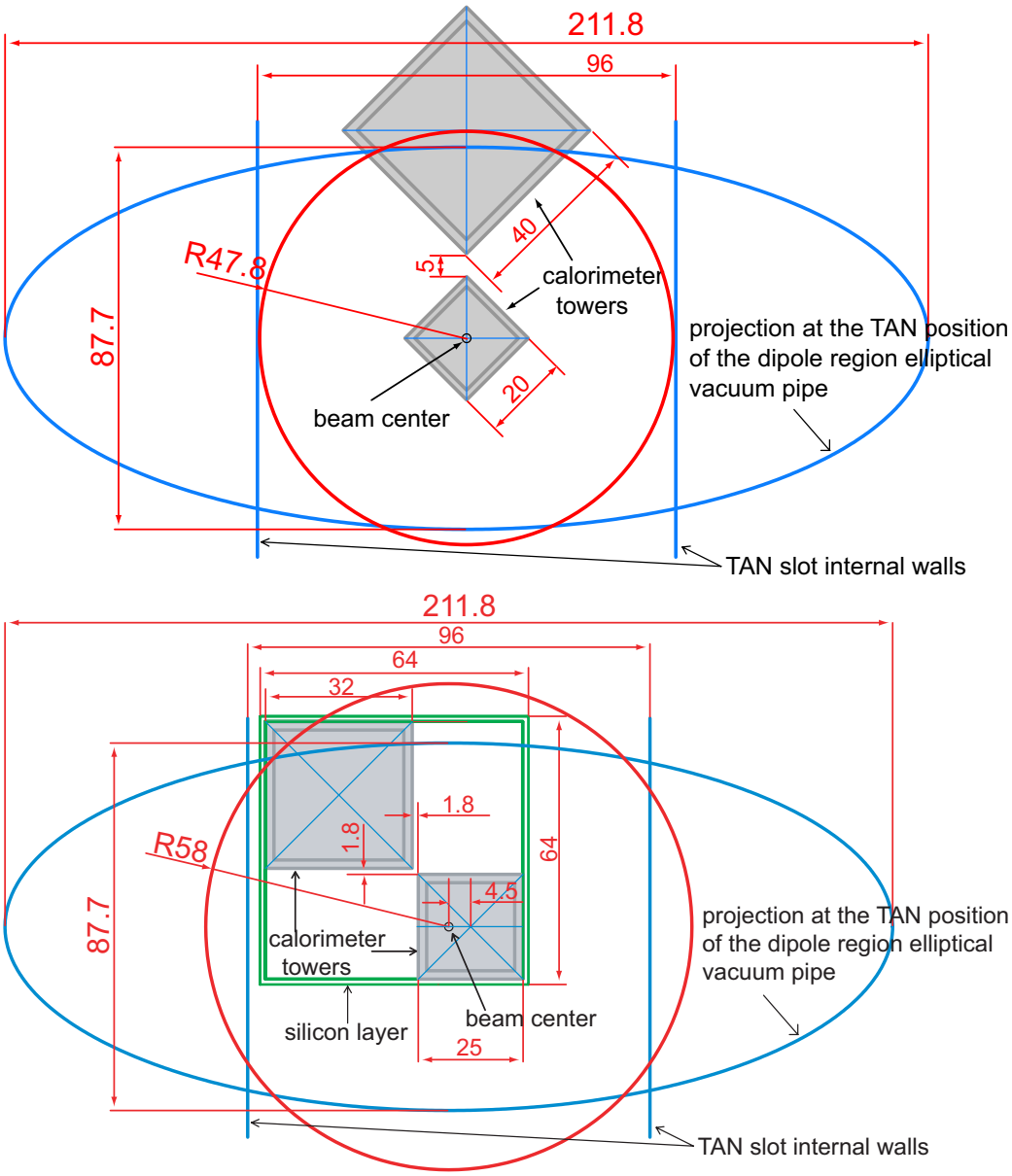

Figure 2.5: The schematic picture of transverse projection of the Arm1 (upper) and arm2 (bottom) detectors. The blue ellipse are the elliptical beam pipe located in the dipole magnets 55m far from the TAN.

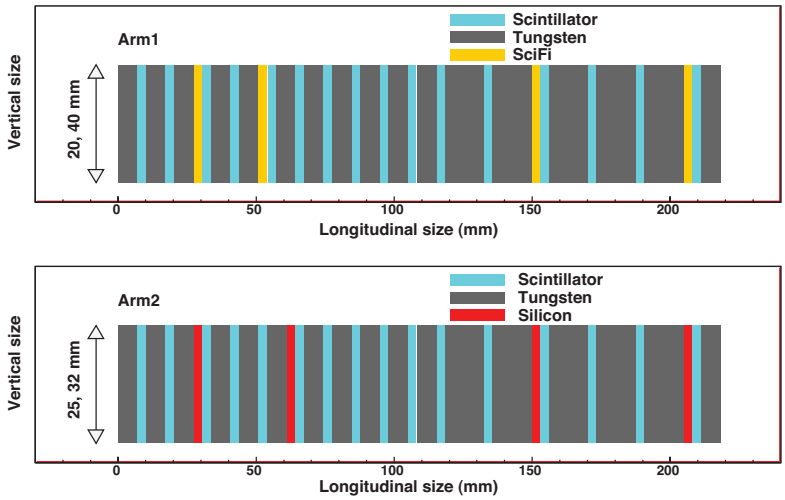

Figure 2.6: The longitudinal structures of the Arm1 detector (upper) and the Arm2 detector (bottom). Gray and cyan layers indicate the tungsten absorber and scintillators, respectively. Orange and red layers indicate the position sensitive layers (SciFi for Arm1 and silicon strip for Arm2).

Figure 2.6 shows the longitudinal structure of the LHCf calorimeters. Upper and bottom panels correspond to Arm1 and Arm2, respectively. The total depth of the calorimeters were 44 radiation length (r.l., X_0) and 1.6 hadronic interaction length (1.6 λ). The gray and the cyan layers indicate the tungsten absorber and scintillators, respectively. Plastic scintillators used for the sampling layers were attached to acrylic light guides and acrylic optical fibers, and then read out by the R7400 (Hamamatsu) photo-multipliers (PMT). The orange and the red layers indicate the position sensitive layers. Four X-Y pairs of the transverse position sensitive detectors were inserted at the depth at 6, 10, 30, and 42 r.l. for Arm1, and at 6, 12, 30, and 42 r.l. for Arm2. Scintillating Fiber (SciFi) detectors were used for Arm1 and silicon micro-strip sensors were used for Arm2. Readout pitches of the SciFi detectors and the silicon sensors were 1 mm and 0.16 mm, respectively.

The calorimeter together with readout PMTs and the front end circuit (FEC) for multi-anode-photo-multipliers (MAPMTs) for the SciFi detectors and the silicon detectors were assembled in the small aluminum boxes. Figure 2.7 shows the pictures of the Arm1 (left) and Arm2 (right) detectors. The dimensions of the detectors are 92mm $\times$ 280mm $\times$ 620mm and 90mm $\times$ 280mm $\times$ 620mm for Arm1 and Arm2, respectively.

In order to enhance the acceptance for any charged particles from IP1

Figure 2.7: Pictures of the LHCf detectors. Left panel shows the Arm1 detector, and right shows the Arm2 detector.

the very thin sub-detectors called front counters (FCs) with the cross section of 80 mm $\times$ 80 mm were installed in front of both the LHCf detectors. The acceptances of the FCs were about 5 times larger than the LHCf calorimeters. The FCs were also important to determine the absolute luminosity [32]. Figure 2.8 shows the schematic picture of the FC. Each front counter consists of two layers of thin plastic scintillator plate (2.0 mm for Arm1 and 2.5mm for Arm2) and a thin copper plate (0.5 mm). The scintillators and copper plates were assembled in the aluminum boxes and the total thickness of FCs was 8 mm corresponding to 0.057 radiation length for Arm1 while 9 mm corresponding to 0.061 radiation length for Arm2. The scintillation light through the acrylic light guides was detected by H3164 PMTs (Hamamatsu). The FC signals were also used as a part of the DAQ triggers.

2.4 Data acquisition (DAQ)

2.4.1 DAQ overview

The data acquisition (DAQ) system of the LHCf experiment was designed to take data at the LHC operations with less than 43 bunches crossing and the

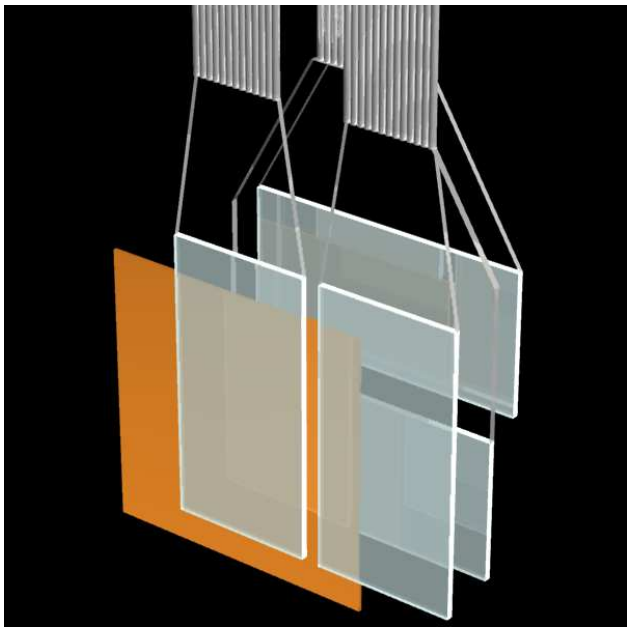

Figure 2.8: The schematic picture of the front counter.

luminosity of less than 10 ^{29}cm^{2}s^{-1}. In this operation condition, the bunch crossing interval is greater than 2 s and the trigger rate of each detector is about 1 kHz. The DAQ system was installed at a space in USA15 (the ATLAS counting room in the tunnel), and we could remotely operate from a operation room on the ground. Figure 2.9 shows the schematic diagram of the DAQ system at the LHC. The PMT signals from the detectors were amplified by the pre-amplifiers (Technoland N-SE 810;Gain $\times$4.8) installed on the top of the TAN. The amplified signals were sent to USA15 through 200 m coaxial cables with 50 Ω impedance. Each signal was divided by FANOUT modules (Technoland N-SE820iP) into the two outputs. One with a single gain was inputted to the charge integrated ADC (CAEN V965). The CAEN V965 can measure charge with two different dynamic ranges;((0.2 pC/ADC count) and (0.025 pC/ADC count) by a 12 bit ADC. The pedestal fluctuation of each ADC channel during the LHC operation due to electric noise was about 20 ADC counts. The other with a quadruple gain was used to generate experimental trigger after passed through the low-pass filter (LHCFLPF001) and the discriminator (CAEN V814B). The cut-off frequency of the low-pass filter was 100 MHz and could reduce the spike noise.

Trigger signals were generated at three levels by the GPIO logic module (KEK GNV-250). Figure 2.10 shows the schematic trigger logic during the

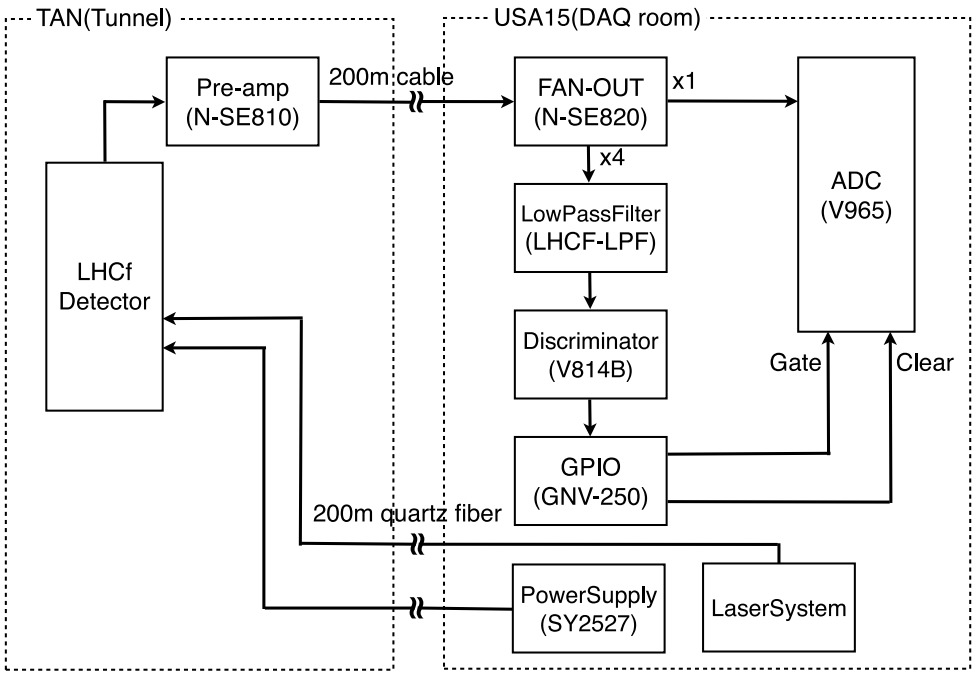

Figure 2.9: The schematic diagram of the DAQ system at the LHC.

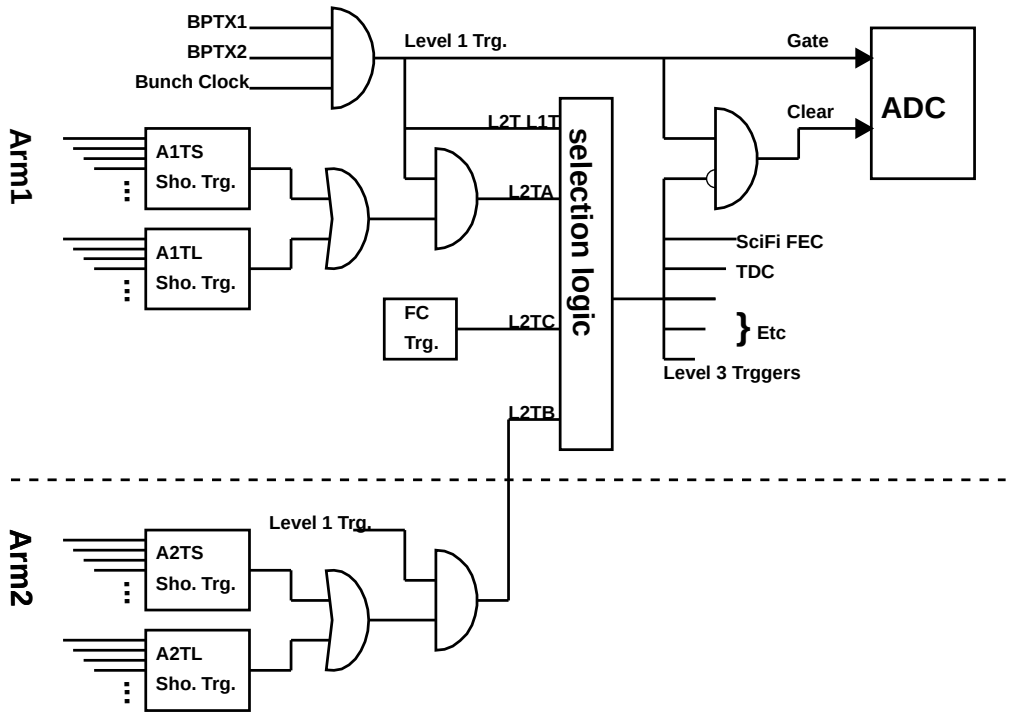

Figure 2.10: The schematic trigger logic diagram during the LHC operations.

	EJ260	BC404	GSO	BGO	PWO	NaI
Density [g/cm^3]	1.02	1.03	6.71	7.13	8.28	3.67
Radiation length [cm]	14.2	14.2	1.38	1.12	0.92	2.59
Decay constant [ns]	9.6	2.2	30-60	300	10-50	230
Relative light yield	20	22	20	10	0.3	100
Wave length λ_{em}[nm]	490	408	430	480	430	410
Refractive index @ λ_{em}	1.58	1.58	1.85	2.15	2.20	1.85

Table 2.2: The properties of EJ260 scintillator together with general scintillators.

LHC operations.

The first level trigger (L1T) was generated from the beam pickup signals (BPTX) when a beam bunch passed IP1. The shower trigger was generated when the signals from any three successive scintillation layers in any towers exceeded a predefined threshold. The threshold was chosen to achieve more than 99% efficiency for more than 100 GeV photon incidents. Then the second level trigger for shower events (L2TA) was issued unless the data acquisition system was busy. The other second level triggers were also generated by using the shower trigger of the other detectors (L2TB), the front counters (L2TC), pedestal, the laser calibration, and etc. Third level triggers were generated by the coincidence of all the second level triggers. The data taking were performed independently for Arm1 and Arm2.

2.5 Pre-calibrations of the detectors

The pre-calibrations of the LHCf detectors previously performed [33, 34] were summarized in this chapter. Each component of the detector was calibrated before assembling.

2.5.1 Scintillator calibration

As mentioned before, the 3 mm thick plastic scintillators of EJ260 (Eljen technology) were used in the sampling layers. The properties of the EJ260 scintillator were summarized in Table 2.2 together with various scintillators. The EJ260 scintillator has long decay constant (9.6 ns) and relatively high light yield. Owing to the long decay constant of the EJ260 scintillator, we could reduce the PMT peak current.

The light yields in the scintillator plates were read by the PMTs through

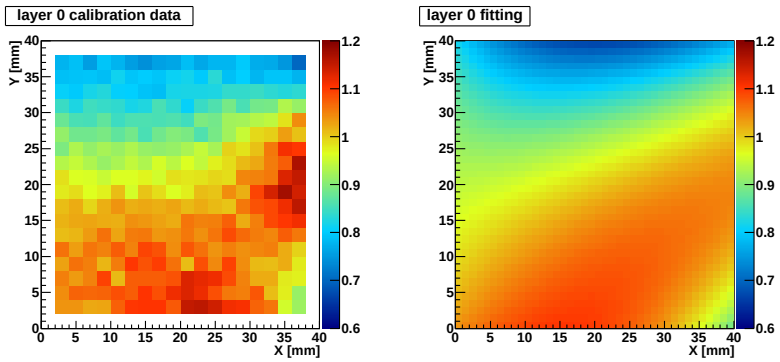

Figure 2.11: The Left panel shows measured relative light yield as a function of incident position. The right panel shows fitting results by using a function in Equation 2.2.

the acrylic light guides and the acrylic optical fibers. The light guides have fish-tail shape and were connected a side of the scintillator plates. Because the optical pass is different depending on the particle incident position, the light yield measured by the PMTs was different even if the same energy was deposited in the scintillator. Therefore, in order to estimate incident energy, the position dependence of light yield must be surveyed as a function of incident position.

The position dependence of the light yield in the scintillators was measured by using 2.2 MeV beta-ray source (^{90}Sr) as shown in Figure 2.11. The Left panel shows the measured relative light yield as a function of incident position. The x and y axes show the position where the beta-ray source was placed. The two dimensional calibration tables were obtained by fitting the measured data with function;

$$F(x,y) = C_0 + C_1 x + C_2 y + C_3 x^2 + C_4 y^2 + C_5 xy + C_6 x^3 + C_7 x^2 y + C_8 x y^2 + C_9 y^3. \quad (2.2)$$

The right panel in Figure 2.11 shows a sample of fitting results by using the function as Equation 2.2

The fitting results for all layers in Arm1 are shown in Figures 2.12 (small tower) and 2.13 (large tower). These calibration tables were used as the correction of light collection efficiency in the analysis and MC simulations.

2.5.2 PMT linearity

We used the customized R7400U PMT (Hamamatsu) in order to achieve wide dynamic range. The linearity of each PMT was measured by using the N_2

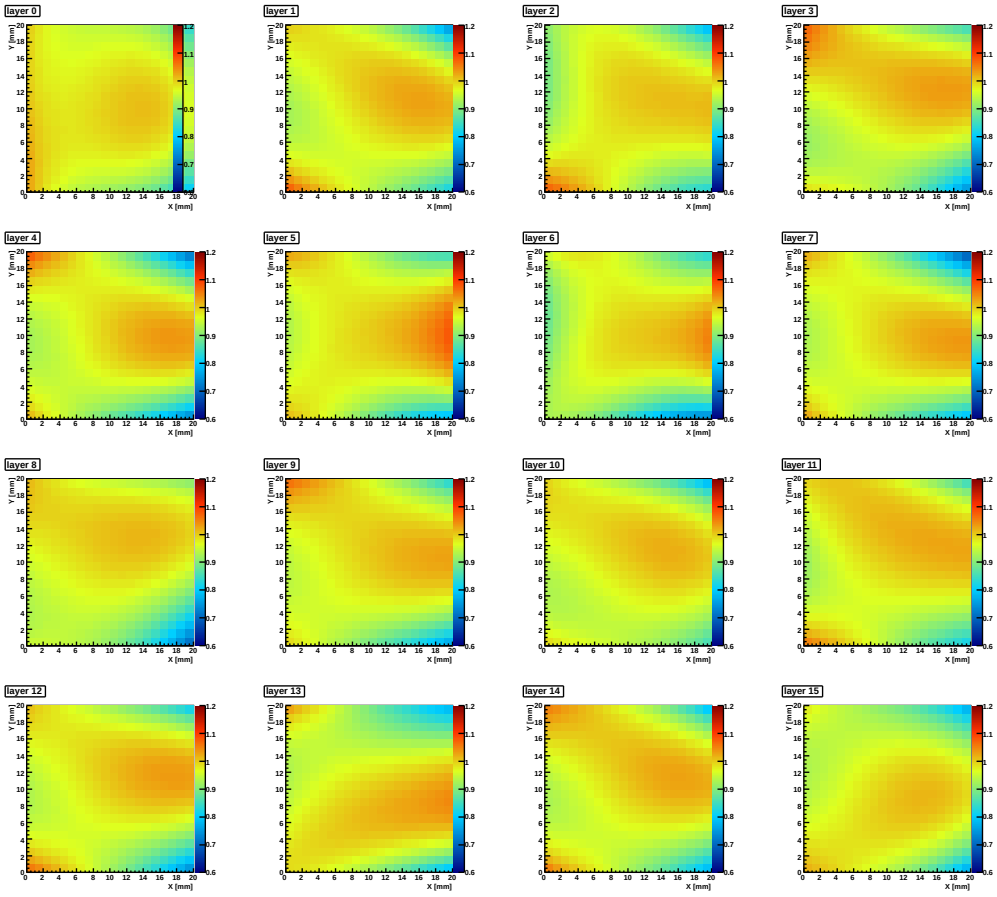

Figure 2.12: The correction functions defined by equation 2.2 for light corrective efficiency. All the 16 layers of the Arm1 small tower are shown from left to right and top to bottom.

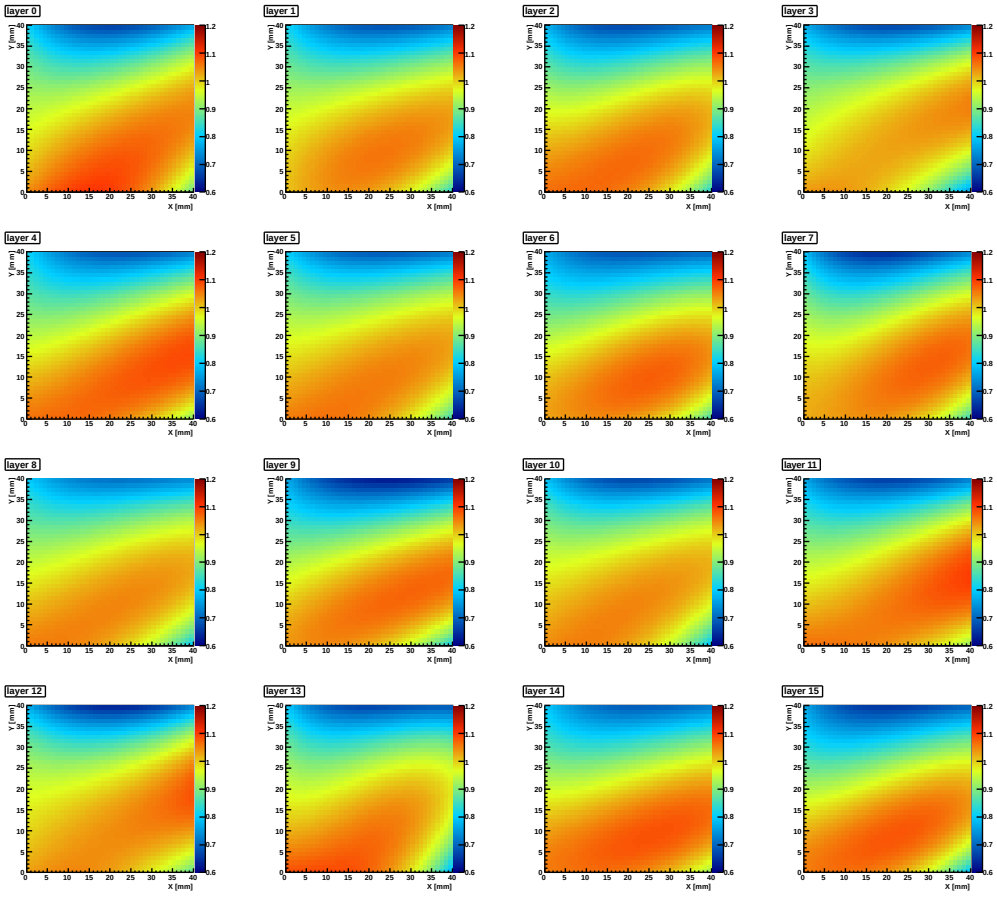

Figure 2.13: The correction functions defined by equation 2.2 for light corrective efficiency. All the 16 layers of the Arm1 large tower are shown from left to right and top to bottom.

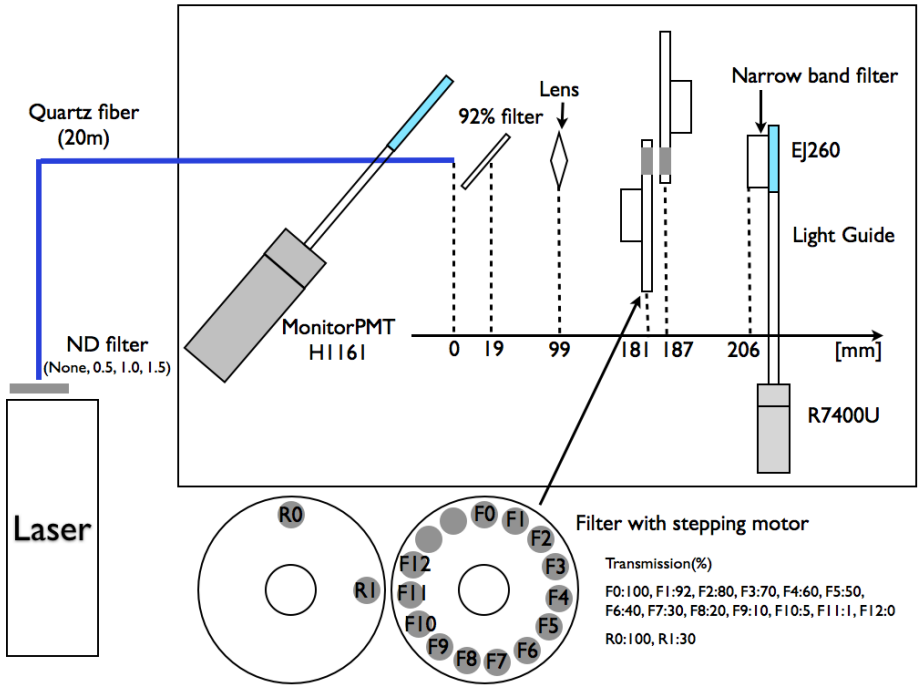

Figure 2.14: The experimental setup of the PMT linearity measurement. The detail is described in the text.

(nitrogen) laser system KEN-1020 (Usho, UV 337.1 nm) with a stable and fast light output. About 300 ps width of the laser pulse was fast enough to compare to the time constant of EJ260 scintillators (9.6 ns). The 337.1nm UV light can directory excite the fluorescent emitter in the EJ260 scintillators. Therefore, the laser system was suitable to calibrate the linearity of the PMTs.

Figure 2.14 shows the experimental setup. The UV light emitted from the KEN-1020 was attenuated by several combination of ND filters, and then entered to the scintillators. Only laser light was selected by the narrow band-pass filter put in front of the EJ260 scintillator. Then the light yield was read by the R7400U PMT.

A part of the UV laser was sampled with the monitor PMT (H1161, Hamamatsu) by using a sampling filter (92% transmittance) for checking the instability of laser output. It was assumed that the monitor PMT has good linearity so that linear output can be keep throughout this measurement. The intensity of the the laser at maximum was equivalent to the light yield by 10 TeV photon shower maximum (100,000 minimum ionising particles

Filter combination	% transmittance	Filter combination	% transmittance
R0 + F00	100.0	R1 + F00	29.3
R0 + F01	95.0	R1 + F01	27.9
R0 + F02	81.7	R1 + F02	24.2
R0 + F03	73.0	R1 + F03	21.3
R0 + F04	62.9	R1 + F04	18.1
R0 + F05	50.2	R1 + F05	14.4
R0 + F06	41.9	R1 + F06	11.9
R0 + F07	29.8	R1 + F07	8.8
R0 + F08	21.6	R1 + F08	6.1
R0 + F09	11.1	R1 + F09	3.1
R0 + F10	6.7	R1 + F10	1.8
R0 + F11	1.3	R1 + F11	0.3

Table 2.3: The list of the combinations of the filters [35]. R* and F* correspond to the filter shown in bottom of Figure 2.14. The transmittance of R0 + F00 defined as 100%.

(MIPs) in the LHCf detector).

The transmittance of the ND filters varied by changing combinations of the front and rear filters as shown in Figure 2.14. They are summarized in Table 2.3 The transmittance of each combination was precisely calibrated in advance. The transmittance of the combination of the filter R0+F00 was defined as 100%, and in case of others they were defined as the ratio to the R0+F00.

The high voltages supplied to the R7400U PMTs were following; 375, 400, 425, 450, 475, 500, 550, 600, 800, 1000 or 1100 V. The PMT linearity was measured in each supplied HV.

Figure 2.15 shows the linearity of PMTs put for the 1st, 2nd, 3rd and 4th layers of the Arm1 small tower. The horizontal axes show the PMT signal value measured by ADC, and the vertical axes show the arbitrary light intensity estimated by the filter density. The black markers indicate the measured results for the PMT supplied HV of 375, 400, 425, 450, 475, 500, 550, 600, 800, 1000 and 1100V (from bottom to top). The cyan lines represent the linear fitting function for each HV. In case of the supplied HV of 450 V which is the typical HV at LHC operations, the deviation from the linear was measured to be less than 5% for even the PMTs which used for the layer in which electromagnetic shower reaches a maximum of the light intensity equivalent to 70,000 MIPs.

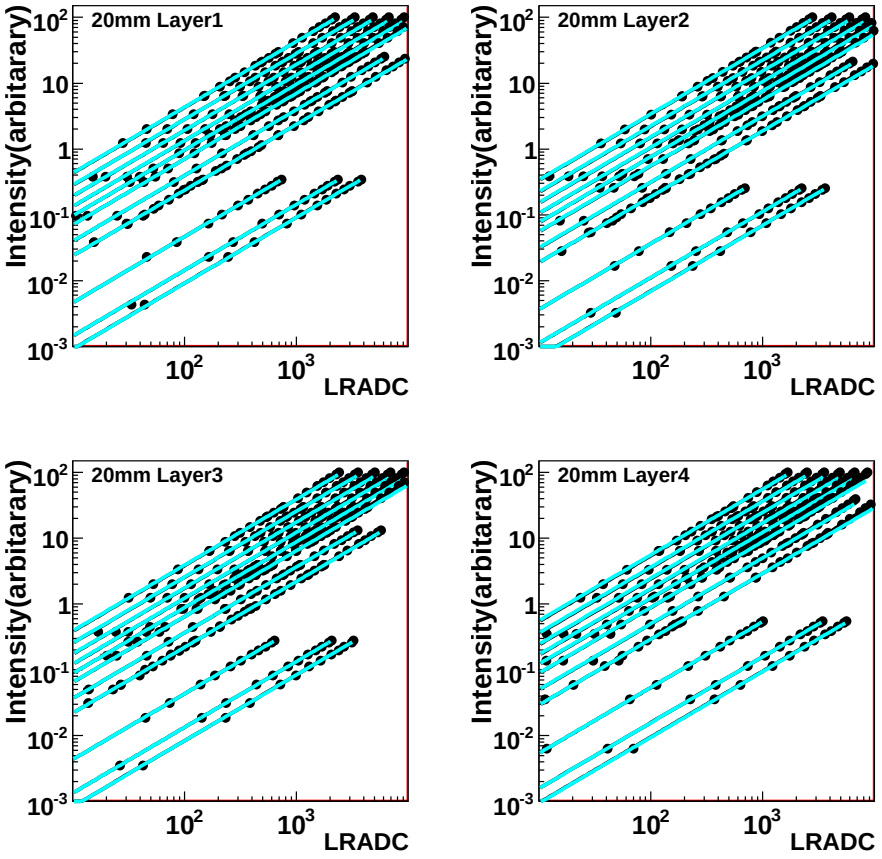

Figure 2.15: Typical samples of the linearity of PMTs (including the EJ260 scintillators) that used for the 1st, 2nd, 3rd and 4th layers of the Arm1 small tower [35]. The horizontal axes show the ADC (Low-Range ADC; LRADC) value, while the vertical axes indicate the intensity of the N_2 laser (arbitrary). The black markers indicate the data results by each HV supplied. The cyan lines represent the linear fitting functions for 375, 400, 425, 450, 475, 500, 550, 600, 800, 1000 and 1100V from the bottom to the top.

2.5.3 Gain calibrations

The conversion factors from measured ADC charge to deposited energy, the energy scale, and energy resolution of the LHCf detectors were calibrated by using the electron and muon beams at CERN-SPS North Area H4 beam line [33]. The electron beams of 50-200 GeV and muon beams of 150 GeV were used in the test. The experimental results were compared with the prediction of MC simulations that was used to estimate the performance at the LHC energy region. Figure 2.16 shows the ADC distributions, that scaled to number of Minimum Ionizing Particles (MIPs) predicted by the MC simulations. The conversion factors of ADC counts to MIPs for the 2nd to 10th scintillator layers in case 180GeV/c electrons were injected [33]. The crosses indicate the experimental results, while the histograms represent the MC predictions. Figure 2.17 shows the ADC distributions, that scaled to number of MIPs predicted by the MC simulations. The conversion factors of ADC counts to MIPs for the 1st and 11th to 16th scintillator layers in case 150GeV/c muons were injected [33]. The crosses also indicate the experimental results while the histograms represent the MC predictions. In these figures, the deposited energies were scaled to the number of MIPs with a coefficient of 0.453 GeV/MIP which corresponds to the most probable energy deposited by a 150 GeV muon passing through the 3 mm thick EJ260 scintillator.

The ADC distributions for electron showers were used for the 2nd to 10th layers of each calorimeter tower. Owing to the sufficient energy deposited by shower particles in these layers, it was possible to determine the conversion factor by using electron beams precisely. The uncertainty in the conversion factor was about 2% for the 2nd to 10th layers. On the other hand, the ADC distributions for muon beams were used in the 1st and the last 6 layers. The uncertainty was about 6% for these layers due to the difficulty of measurement caused by very poor signal amplitude of muon beam.

2.5.4 Calibration method during the LHC operation

The gain of each scintillator and PMT was monitored by using the N_2 laser installed in USA15 during the LHC operations. Laser pulses were transmitted from the USA15 through a long multi-core quartz optical fiber to each detector. Then the light was distributed to each scintillator. A part of the laser pulse (1%) was monitored by two PMTs (R7400U) in the USA15. The gain of one of the PMTs was monitored by using an light pulsar (241Am; α-ray) attached in front of the photo-cathode. The signals from the monitor PMTs were also used to generate one of the first level triggers for the DAQ. The stability was confirmed to be less than 3% during $\sqrt{s} = 7$ TeV

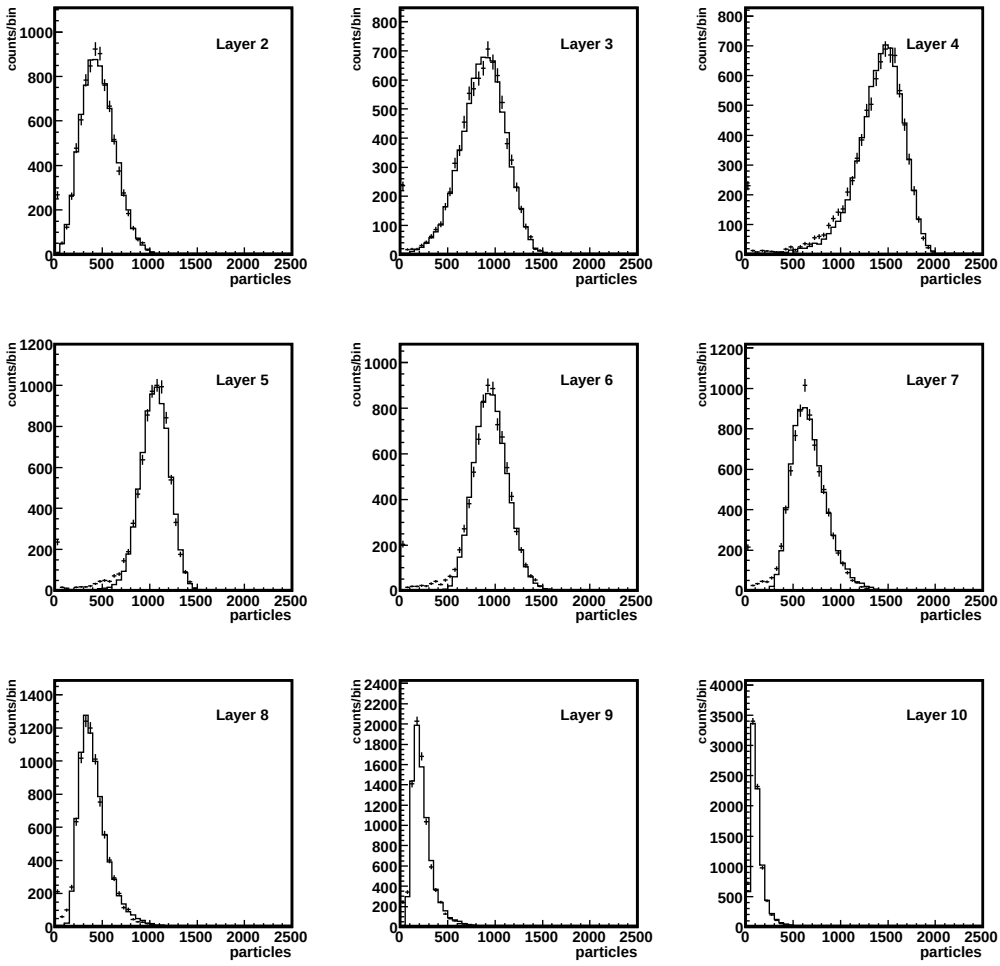

Figure 2.16: The ADC distributions, that scaled to number of particles predicted by the MC simulations, for the 2nd to 10th scintillator layers in case 180GeV/c electrons were injected [33].

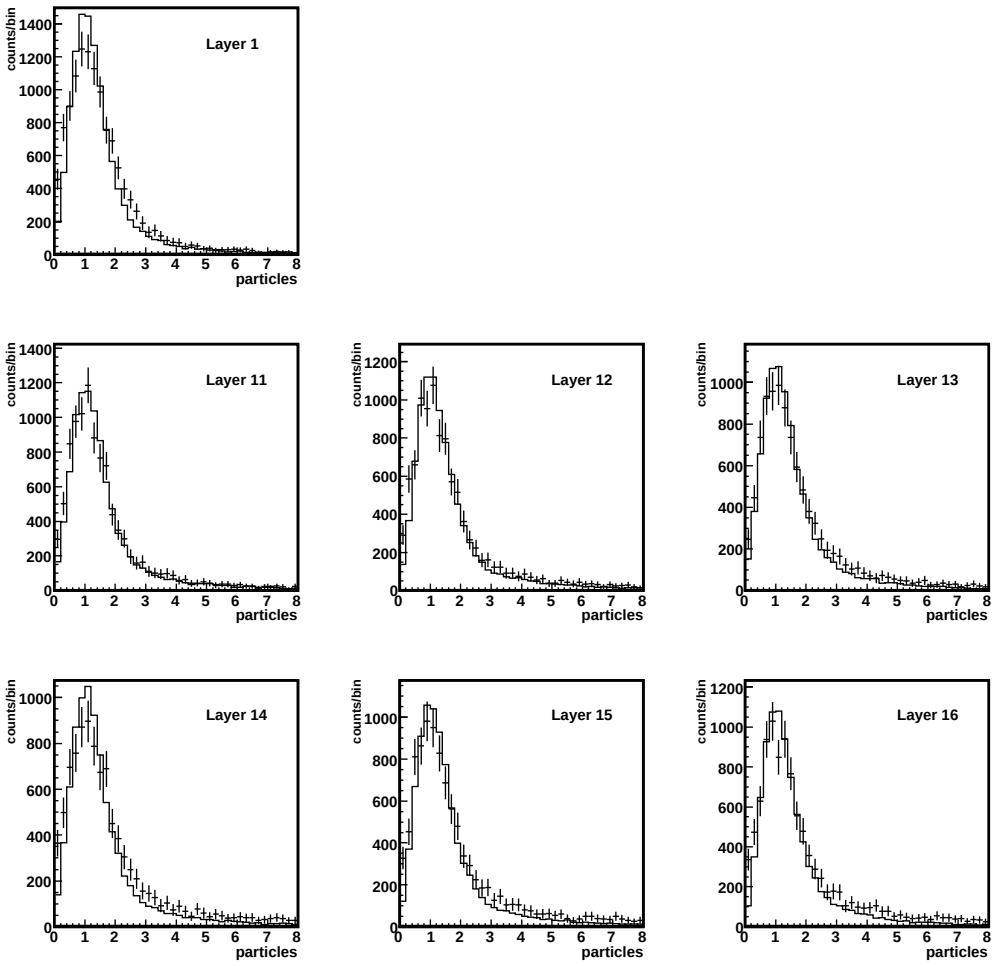

Figure 2.17: The ADC distributions, that scaled to number of particles predicted by the MC simulations, for the 1st and 11th to 16th scintillator layers in case 150GeV/c muons were injected [33].

Particle	Ratio [%]	Ratio (Energy>1000GeV)
photon	43.1	12.1
π	0.6	0.1
K	1.7	1.2
Neutron	51.9	81.9
Λ	2.7	4.7
others	<0.1	<0.1

Table 2.4: Particles observed at the Arm1 small tower simulated with the EPOS 1.99 model.

p-*p* operation in 2010 [35].

2.6 Neutral baryon measurement at LHC forward region

As discussed before, the measurement of forward baryons at the very forward region on high energy hadronic interactions is important to verify the hadronic interaction models. Neutrons are main components of observed forward baryons in the region of the LHCf detectors. Table 2.4 shows the numbers of particles observed at the Arm1 small tower predicted by the EPOS 1.99 model. Except photons, neutrons are dominant particles in the LHCf acceptance especially for the particles of energies more than 1 TeV. Because we cannot separate hadronic showers induced by neutrons or others, neutral baryons including neutrons, Λ's and the others were called simply neutrons hereafter. It is because forward leading baryons are relevant to air shower development. However, in order to carry out the measurement, the detail understanding of the detector performance for hadronic showers that have not been studied in detail so far was indispensable. The performance of the LHCf detectors for photons [33, 42] have been already studied in detail, while the detector performance for hadronic showers is studied precisely in this study for the first time. The performances of the LHCf detectors for hadronic showers were studied by using 350 GeV proton beams at CERN-SPS and for neutrons of energies of up to 3.5 TeV neutrons using MC simulations. The validity of the performance estimated by the Monte-Carlo simulations were tested by comparing the results of SPS beam test and the MC simulations. The results of the MC simulations were reported in Chapter 3.1 and the results of the SPS beam test were reported in Chapter 3.2. The spectrum unfold method to obtain initial energy distribution from the smeared

spectrum was presented in Chapter **??**. The neutron analysis results of $\sqrt{s}$ = 7 TeV proton-proton collisions were described in Chapters 5, 6.

Chapter 3

The performance of the LHCf detectors for neutron measurements

3.1 Performance study based on MC simulation

3.1.1 Overview

Since the visible energy in the calorimeters, the transverse width of the showers, and the typical longitudinal depth of the showers are completely different between the hadronic showers induced by neutrons and electro-magnetic shower induced by photons, it was necessary to estimate the detector response for the measurement of hadron. The performance of the LHCf detectors for neutrons was studied with Monte-Carlo (MC) simulations using the COSMOS (v7.49) and EPICS (v8.81) [40] libraries which are used in the simulation of air shower development and detector response. In addition, QGSJET II-03 [17] has been used as a hadron interaction model in the detector simulations for particle energies greater than 90 GeV and DPMJET 3.04 [13] for particle energies less than 90 GeV. In order to estimate the dependence of the detector simulation on the choice of the interaction model, we compared the results obtained by the QGSJET II-03 + DPMJET 3.04 (called QGSJET II-03, hereafter) model and the DPMJET 3.04 model only with experimental test beam results as discussed in Chapter 3.2.

Because the total hadron interaction length of the LHCf calorimeters is 1.6 λ (while the radiation length is 44 r.l.), some of neutrons pass through the detector without interactions. Therefore, the visible energy of hadronic

showers has a large fluctuation. In order to estimate energy and position resolution and detection efficiency of the LHCf detectors, neutrons with energy in the range 100 GeV to 3500 GeV were injected to the center of the small tower and the large tower. Neutrons with energy of 1 TeV were uniformly injected to the calorimeter to estimate the position dependence of calorimeter and effects of transverse shower leakage.

To analyze the MC data as same as the experimental data, the analysis procedure of the MC data is as below. At first, true information in the MC simulation such as energy deposited in the scintillators, SciFi layers or Silicon detectors were smeared with realistic pedestal fluctuation to reproduce experimental situation. Then, energy deposited in each channel was converted to number of MIPs (minimum ionizing shower particles) so that same analysis procedure can be used as same as the data analysis. After that, the transverse hit position and longitudinal shower shapes were reconstructed. Finally, the energy and transverse momentum were reconstructed by using the number of particles observed in each sampling layer after the Particle Identification (PID) process.

3.1.2 Detection efficiency

Since the depth of the LHCf detectors is only 1.6 hadron interaction lengths, some neutrons pass through the detectors without interaction as mentioned before. An offline event selection criterion has been applied for neutron analysis in addition to an experimental trigger condition. The neutron events were selected for analysis when the energy deposited in three successive scintillation layers exceeds the energy deposited by 200 MIPs. The energy deposit equivalent to 1MIP is defined as 0.453MeV determined by the muon calibration at CERN-SPS.

The detection efficiency of the Arm1 detector for neutrons are shown in Figure 3.1 as a function of neutron energy. The black and red symbols correspond to the efficiency for the Arm1 small and large towers, respectively. After offline event selection, the detection efficiency plateaus at a nearly constant 70% to 80% above 500 GeV.

3.1.3 Transverse hit position resolution

Transverse hit position is one of the important observable not only for the determination of the transverse momentum p_T but also for the estimation of the energy. Because the transverse sizes of the LHCf detectors are limited, some fraction of shower particles leaks out from the calorimeters. The effect of the leakage will be discussed later.

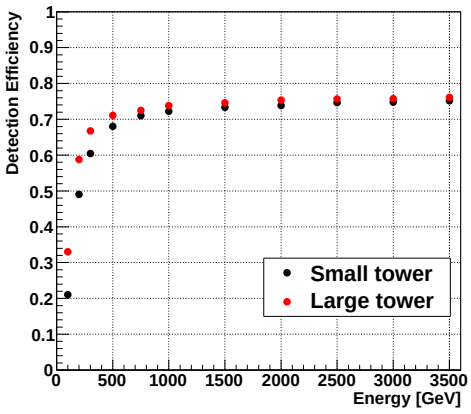

Figure 3.1: Detection efficiency of the Arm1 detector for neutrons at the detector center as a function of energy. The black (red) markers correspond to the efficiency of the Arm1 small (large) tower.

The LHCf detectors had the transverse hit position sensors as mentioned before. For the Arm1 detector, the SciFi detectors composed of bundles of 1mm×1mm scintillation fiber were used. On the other hand, the silicon micro strip detector were used for the Arm2 detector [41]. The performance of position determination for electromagnetic showers were well measured [34, 42], but it did not studied for hadronic showers yet. In this chapter the energy dependence of position resolution and its position dependence were evaluated by using the MC simulation.

Figure 3.2 shows a typical hadron-like event recorded by the SciFi detector. The black and the red histograms correspond to signal of X and Y axes, respectively. The thick vertical lines represent reconstructed hit positions for each axis. The algorithm of hit position reconstruction is described as follows. Firstly, the peaks of the hit-maps of SciFi layers were searched. Then, the number of peaks corresponding to the number of incident particles were determined. If the height of secondary peak exceeded 10 % of the height of the primary peak, such events were reconstructed as the multi-hit events. Finally hit-map of the SciFi or the silicon sensor were fitted with a function, and the transverse hit positions were obtained from the fitting center in both of the X and the Y layers. The transverse hit position reconstructed in the layer which had the largest signal among the four layers was selected.

The energy dependence of position reconstruction was evaluated by the MC with various energy incident at the detector center; $(x, y) = (8.86,\ 11.13)$ for small tower and $(x, y) = (19.29,\ 20.71)$ for large tower. Figure 3.3 shows

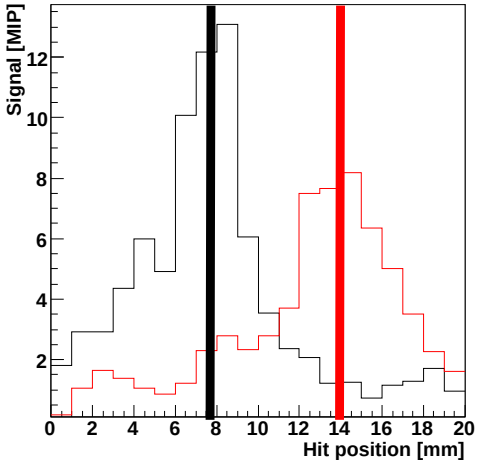

Figure 3.2: Typical signal of a neutron event candidate recorded by the SciFi detector. The horizontal axis shows the hit-position on the SciFi detector, and the vertical axis shows the signal output of the SciFi detector. The black and the red histograms correspond to the signal of X and Y axis, respectively. Thick vertical lines represent reconstructed hit positions for each axis.

the reconstructed position distribution for each energy incident with energies from 100 to 3500 GeV. The black and the red histograms correspond to the reconstructed position of X axis and Y axis, respectively. In each energy, position was well reconstructed. The position resolution was defined as the FWHM of these distributions ,and summarized in Figure 3.5. The left panel corresponds to the small tower and the right panel corresponds to the large tower. In these figures, the blue cross corresponds to the X axis, and the magenta cross corresponds to the Y axis. It clearly depends on the energy, but the resolution itself is less than 1 mm above 1 TeV and is quite sufficient. The main difference between the X and the Y axes was caused by the dead channels of SciFi detectors and the difference of longitudinal positions.

3.1.4 Energy response and linearity

The energy of incident neutrons were estimated from the deposited energy in the calorimeters. Owing to constant shower size in transverse direction, the transverse leakage effect can be corrected. Details of shower leakage are explained in Chapter 3.1.6.

The total energy deposited in the calorimeter was used as an estimator of

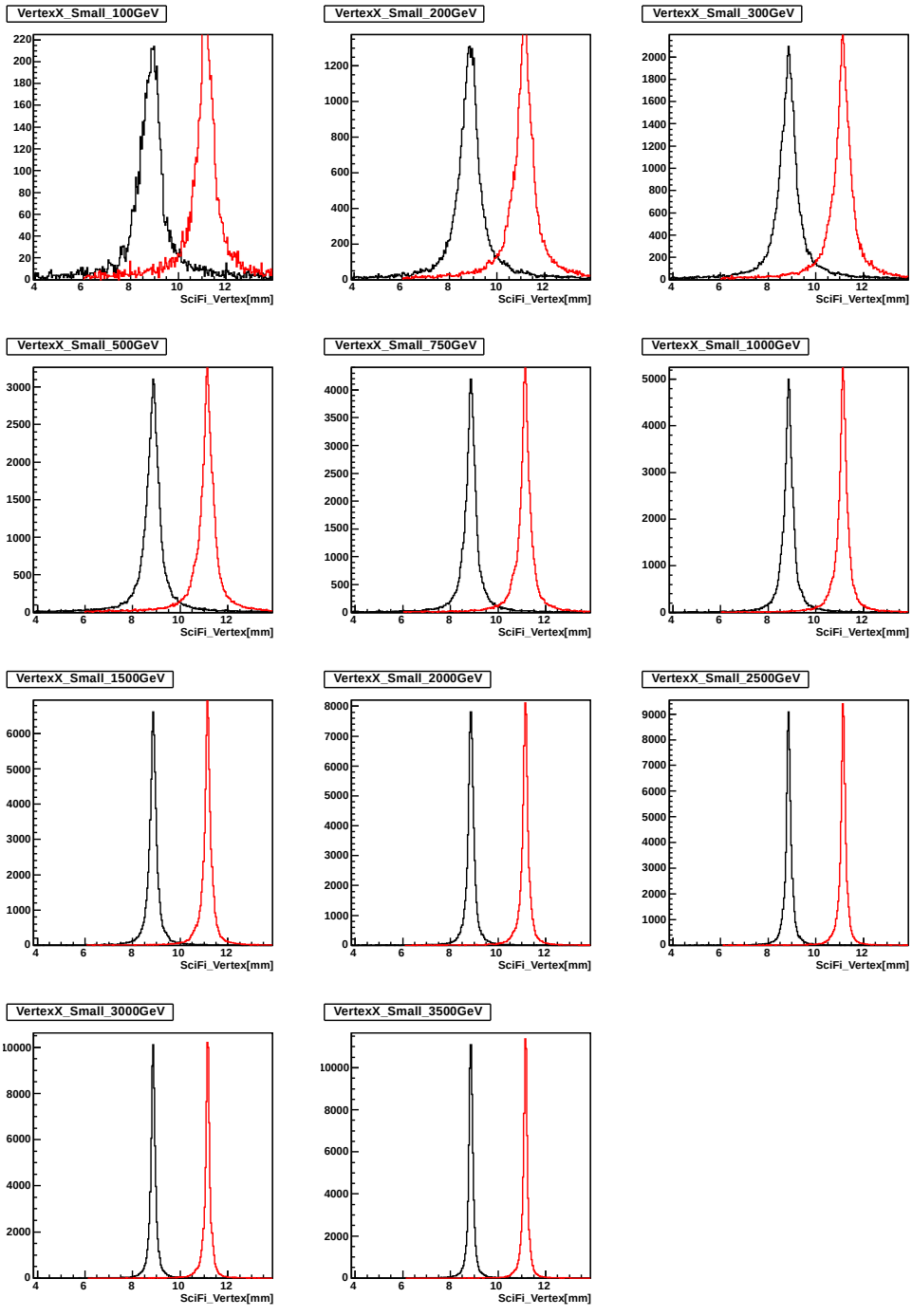

Figure 3.3: The reconstructed shower incident position distributions at each energy incident for the Arm1 small tower. The black histograms show the vertex X and the red histograms show the vertex Y. They are distributed around the true incident positions.

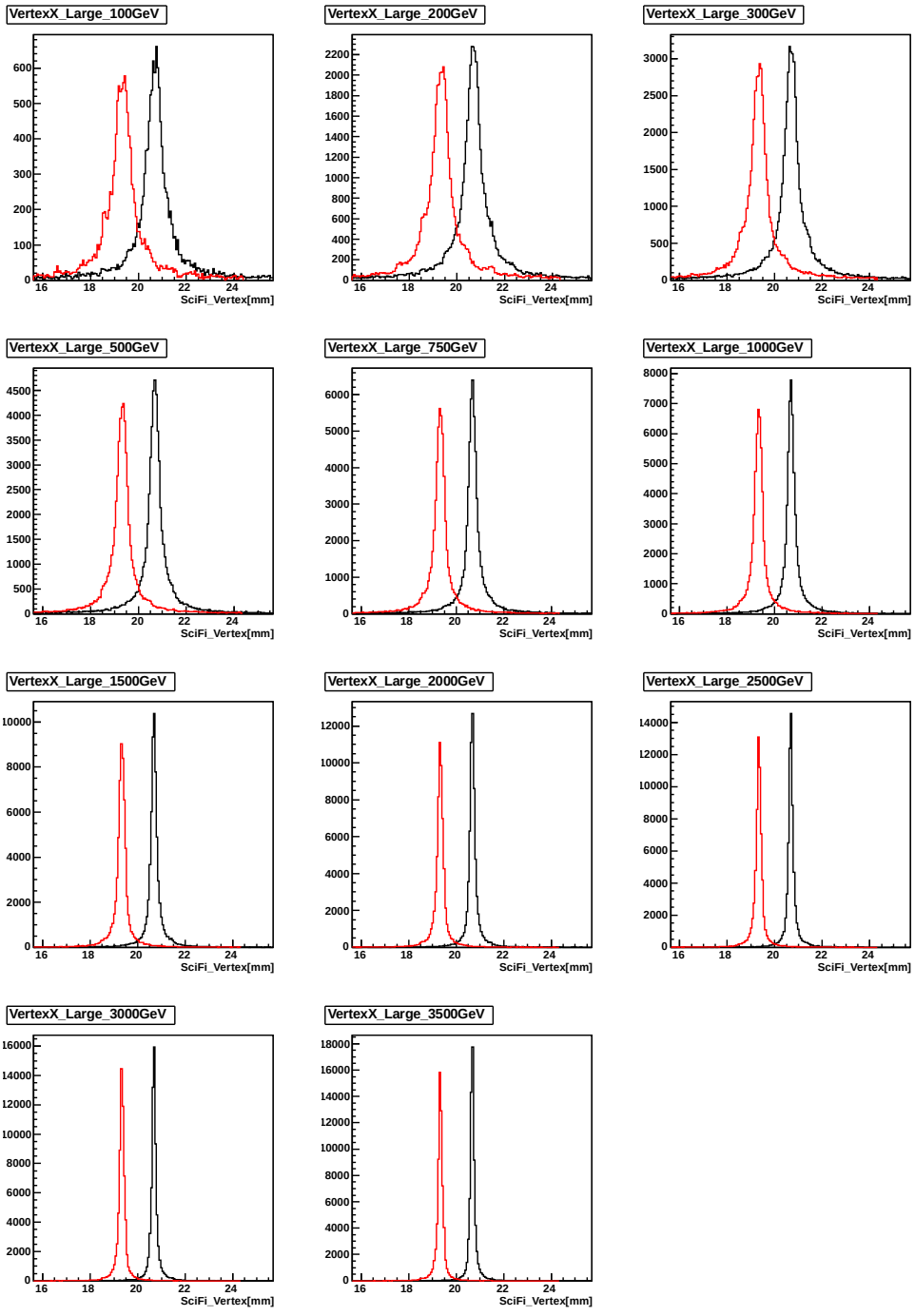

Figure 3.4: The reconstructed shower incident position distributions at each energy incident for the Arm1 large tower. The black histograms show the vertex X and the red histograms show the vertex Y. They are distributed around the true incident positions.

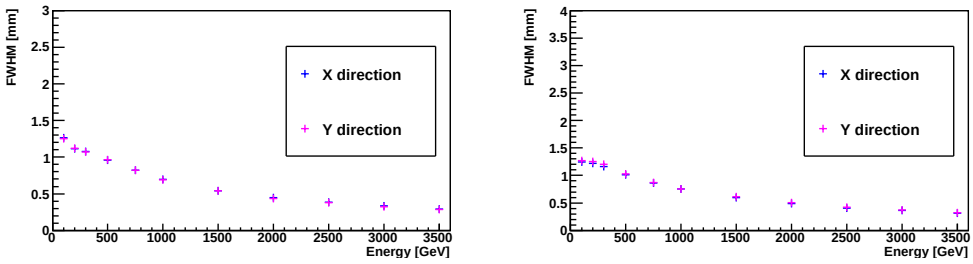

Figure 3.5: The FWHM values of the reconstructed incident position distributions as a function of incident energy. The blue cross corresponds to the X axis, and the magenta cross corresponds to the Y axis. The left and the right correspond to the position resolution of the small and the large tower of Arm1, respectively

the incident neutron energy. An energy estimator named sumdE is defined as,

$$\text{sumdE} = \sum_{i=2}^{15} n_{step} \times dE_i.$$

On the other hand, sumdE for photon-like events (sumdE_γ) is defined as,

$$\text{sumdE}_\gamma = \sum_{1}^{12} n_{step} \times dE_i. \tag{3.1}$$

Here dE_i is the energy deposited in the i-th sampling layer, and n_{step} is chosen as $n_{step} = 1$ for the 2nd to the 10'th layers, and $n_{step} = 2$ for the 11'th to the last layers proportional to the thickness of the tungsten. Figure 3.6 shows the sumdE distribution when 1000 GeV neutrons were injected to the center of the small tower.

An energy response function was determined by the relationship between the incident energy E and sumdE for each tower as shown in Figures 3.7 and 3.8. Neutrons with the energies from 100 GeV to 3500 GeV were injected at the center of the calorimeters in this study. The horizontal axis corresponds to the energy of incident neutrons (E) and the vertical axis represents the average value of sumdE ($\langle\text{sumdE}\rangle$). The response functions were derived from the MC with empirical polynomials. A quadratic function as Equation (3.2) was used as the energy response function for all the towers except the Arm1 small tower as;

$$\langle\text{sumdE}\rangle = f(E) = \alpha E^2 + \beta E + \gamma. \tag{3.2}$$

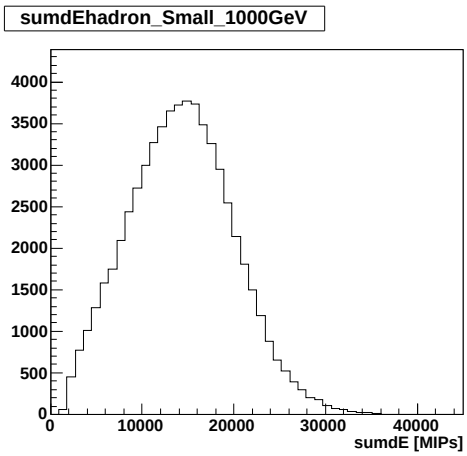

Figure 3.6: sumdE distribution in case that 1000 GeV neutrons were injected to the center of the Arm1 small tower.

For the Arm1 small tower, the function as Equation (3.3) given below was used;

$$\langle \text{sumdE} \rangle = f(E) = \begin{cases} \alpha E^2 + \beta E + \gamma & (\text{E} < 500\text{GeV}) \\ \delta E + \epsilon & (500\text{GeV} < \text{E}). \end{cases} \tag{3.3}$$

The parameters expressed by the function shown as Equation (3.3) were chosen to smoothly connect the data at 500 GeV. The bottom graphs in Figures 3.7 and 3.8 show residuals from the fitting result with Equations 3.2 and 3.3. The non-linearity was found to be less than $\pm 2\%$ for all the towers. The error bars indicate the statistical errors only.

3.1.5 Energy resolution

The energy deposited by neutron induced showers have large fluctuations due to the limited length of the calorimeters. Figures 3.9 and 3.10 show the reconstructed energy distributions of each energy for the Arm1 detector. Hadron-like events were discriminated from photon-like events by using a PID (Particle Identification) algorithm as discussed later in Chapter 5.2.1. Because visible energies in the calorimeter are quite different between neutron and photon with the same energy, the energy estimation depends on the PID results. Of course all the events in this MC study are neutron events, but we selected only those that would pass the hadron-like selection for calculation of the neutron energy resolution. The black and the red histograms in Figures 3.9 and 3.10 show the reconstructed energy distributions after PID selection

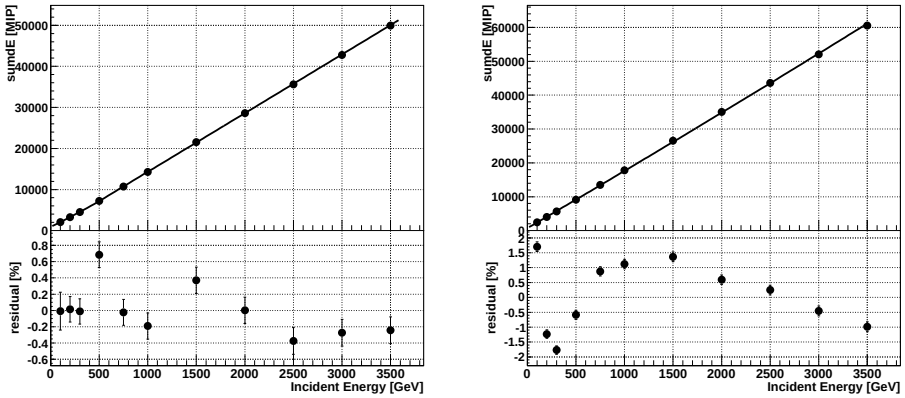

Figure 3.7: The energy response function for the Arm1 detector obtained by MC simulation with QGSJET II-03. The left and the right figures correspond to the small tower and the large tower, respectively. The upper panels show the relations between the incident energy and the average of sumdE. The black curves are the results of fitting. The bottom panels show the residuals from the fitting.

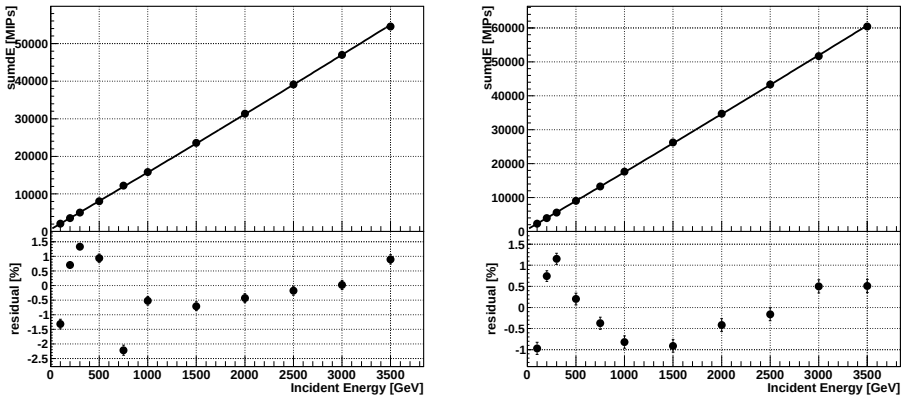

Figure 3.8: The energy response function for the Arm2 detector obtained by MC simulation with QGSJET II-03. The left and the right figures correspond to the small tower and the large tower, respectively. The upper panels show the relations between the incident energy and the average of sumdE. The black curves are the results of fitting. The bottom panels show the residuals from the fitting.

for hadron-like events (black) and photon-like events (red) at each incident energy, respectively.

The energy resolution was defined as the standard deviation of the reconstructed energy distribution. Figure 3.11 shows the expected energy resolutions of the small tower and the large tower as a function of the incident energy. The left panel and right panel correspond to the energy resolutions of the Arm1 detector and the Arm2 detector, respectively. From the results of these MC calculation, the energy resolutions are about 40% for all the calorimeter towers.

3.1.6 Shower leak out correction

The shower leakage reduces visible energy in the calorimeters and affect estimation of energy. In order to obtain better energy resolution, the shower leakage effects should be corrected. To estimate the effects from the shower leakage, a study by using MC simulation in which 1,000 GeV neutrons were uniformly injected to the detector was carried out.

The top panels of Figure 3.12 shows the position dependence of average of sumdE $\langle$sumdE$\rangle$ for the small and the large calorimeters, respectively. The vertical and horizontal axes shows the reconstructed hit position, and the color contour shows the $\langle$sumdE$\rangle$ normalized to the value at the center.

If more than two particles hit the detector at the same time, the shower leakage affects each other. This effect is called the shower leakage-in effect. The leakage-in has significant effect on measurement of π^0 mesons. It also make some effect for the neutron measurement. The bottom panels of Figure 3.12 show the fraction of energy deposit observed in the neighbor tower. The X and Y axes indicate the incident position of neutrons in the small (large) tower, and the color contour corresponds to the fraction of energy observed in the large (small) tower at the left (right) panel. These effects can be calculated by the equations below;

$$M^{TS} = L_{out}^{TS} T^{TS} + L_{in}^{TL} T^{TL}, \tag{3.4}$$

$$M^{TL} = L_{in}^{TS} T^{TS} + L_{out}^{TL} T^{TL}. \tag{3.5}$$

Here, T^{TS} and T^{TL} represent the actual sum of the energy deposited in the small tower and the large tower, respectively. L_{out} and L_{in} correspond to the leak-out factor and leak-in factor as functions of hit position, respectively. M^{TS} (M^{TL}) represents the measured energy deposited in the small tower (large tower).

Because the energy resolution gets worse due to the leakage effect, we applied leakage correction as functions of the hit position using equation

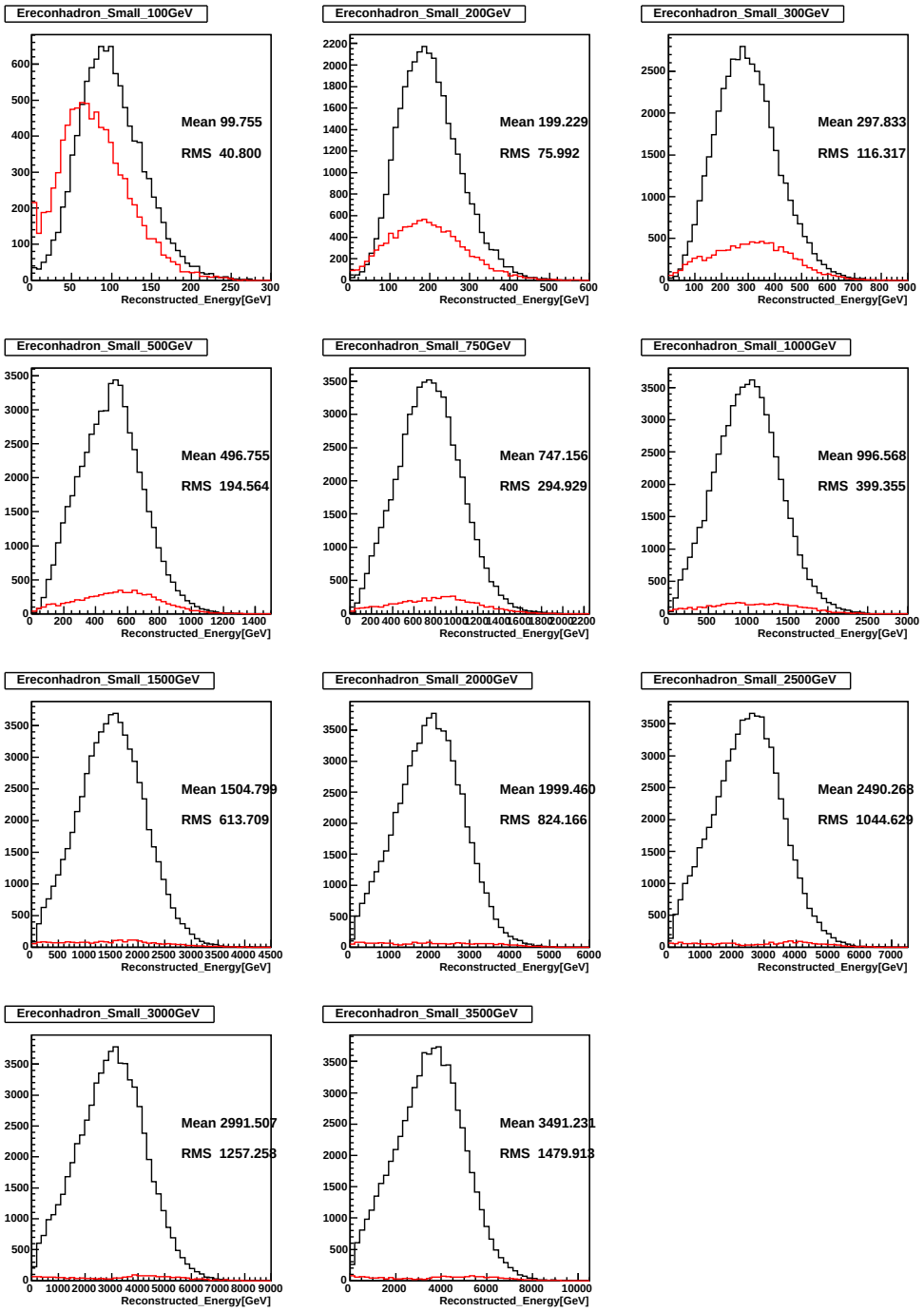

Figure 3.9: Reconstructed energy distributions in the Arm1 small tower for neutron incident with energy 100, 200, ..., 3500 GeV. The black and the red histograms show the hadron-like and photon-like events, respectively.

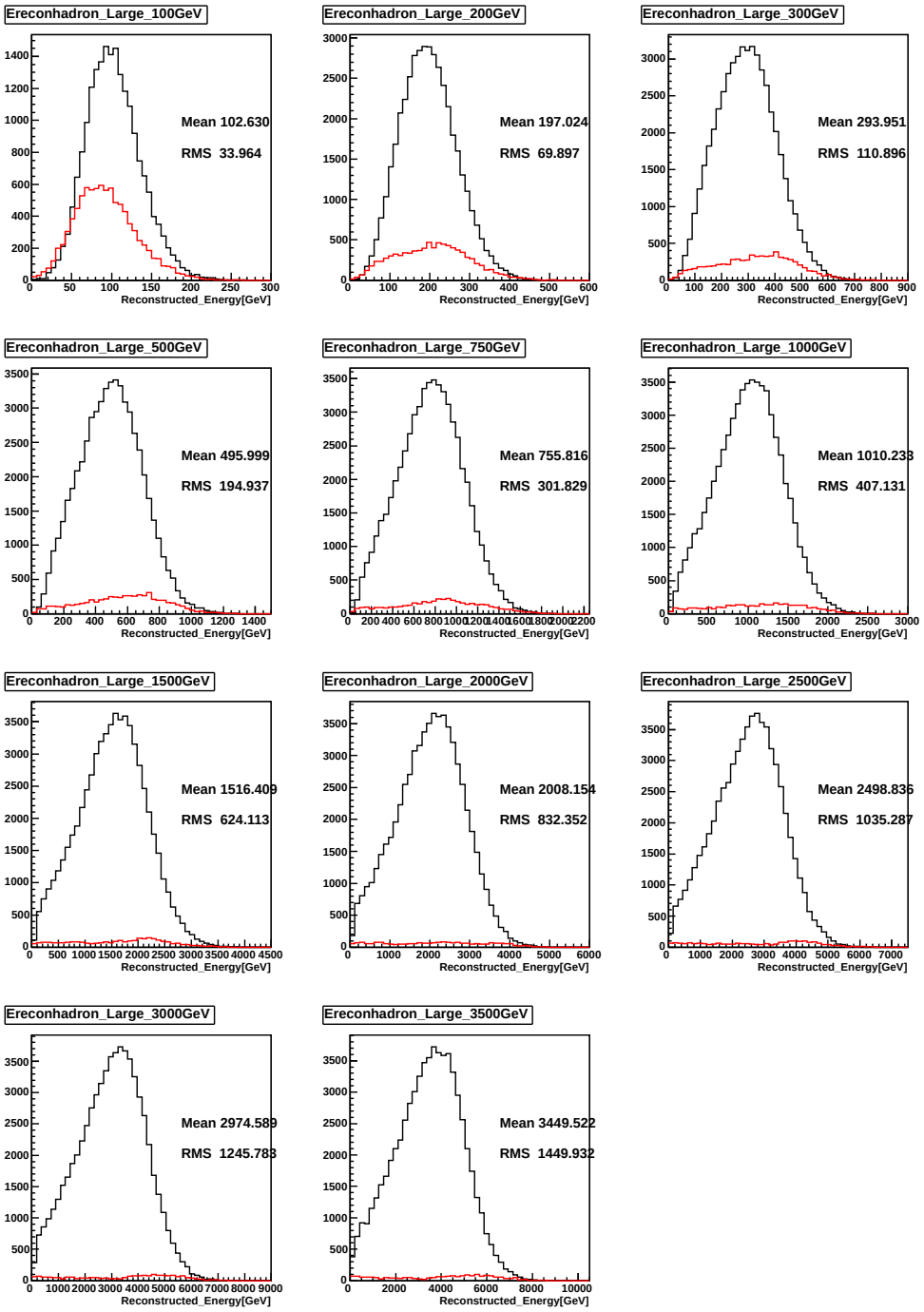

Figure 3.10: Reconstructed energy distributions in the Arm1 large tower for neutron incident with energy 100, 200, ..., 3500 GeV. The black and the red histograms show the hadron-like and photon-like events, respectively.

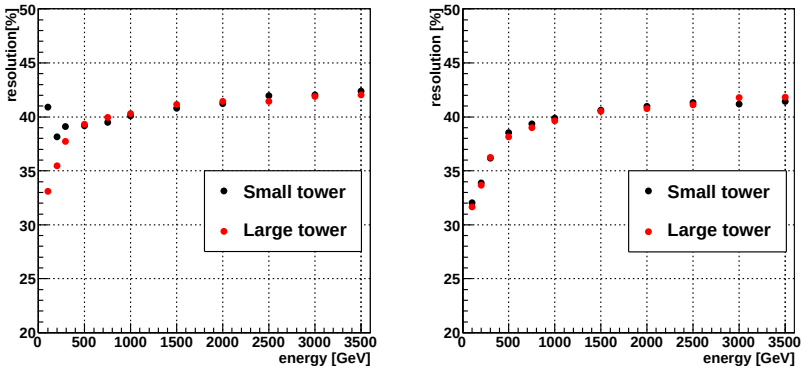

Figure 3.11: The energy resolution of the small tower (black) and the large tower (red) for neutrons as a function of energy. The left panel is for the Arm1 detector and the right panel for Arm2.

Table 3.1: The average values of the reconstructed energy divided by its true energy with leakage correction and without leakage correction as shown in Figure 3.13.

	Mean	RMS	RMS/Mean
W correction	**0.998**	0.418	0.419
W/O correction	**0.891**	00.381	0.428

below;

$$T^{TS} = \frac{L^{TL}_{out} M^{TS} - L^{TL}_{in} M^{TL}}{L^{TS}_{out} L^{TL}_{out} - L^{TS}_{in} L^{TL}_{in}}, \tag{3.6}$$

$$T^{TL} = \frac{L^{TS}_{out} M^{TL} - L^{TS}_{in} M^{TS}}{L^{TS}_{out} L^{TL}_{out} - L^{TS}_{in} L^{TL}_{in}}. \tag{3.7}$$

They are the solution of the simultaneous equations shown as in Equation 3.4 and 3.5

Because the energy resolution for the events hitting within 2 mm from the edge of the calorimeters has a large fluctuation, they were removed from the analysis. Figure 3.13 show the result of the leakage correction. The black and the blue (hatched) histograms correspond to the reconstructed energy divided by its true energy with the leakage correction and without the correction, respectively. Neutrons with uniform energy from 100 GeV to 3500 GeV were uniformly injected to the detector in this study. The average values of the distribution are summarized in Table 3.1. The average of the

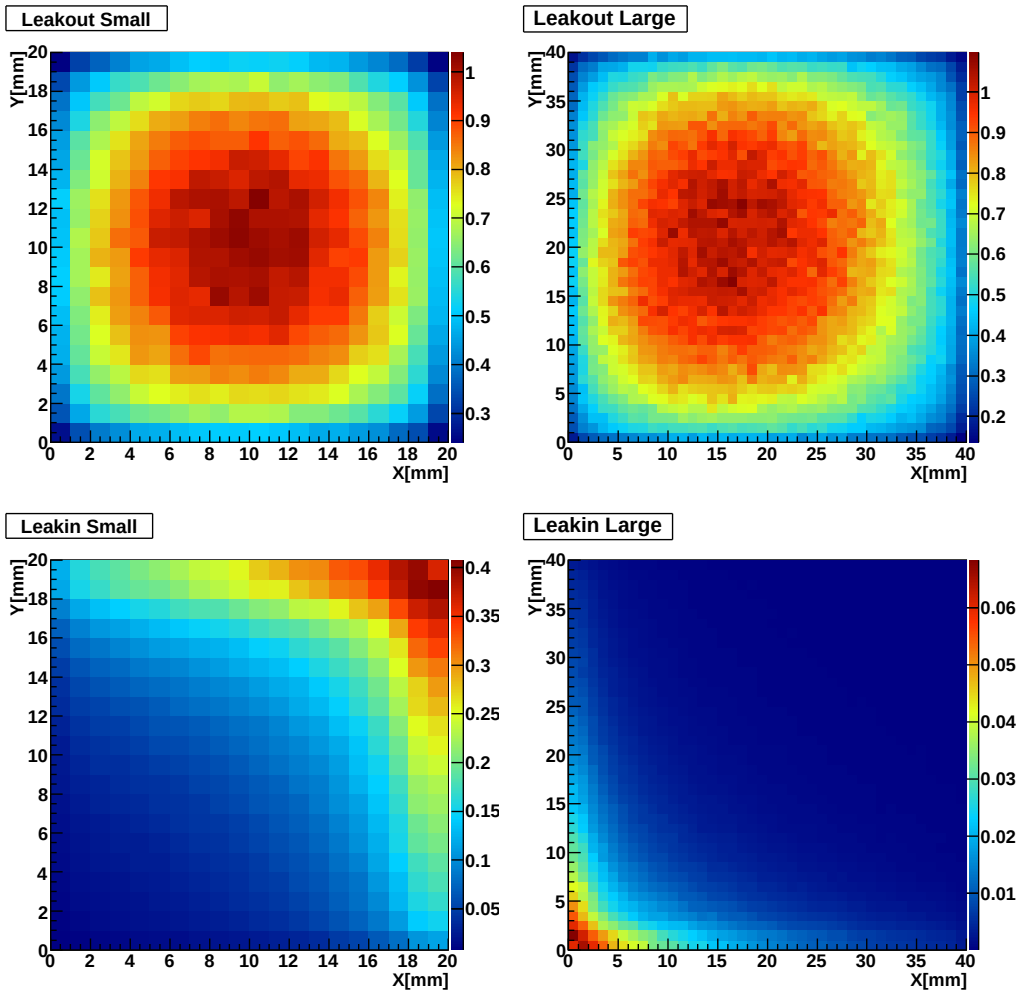

Figure 3.12: The top panels show the position dependence of fraction of energy deposit. The X and the Y axes show the incident positions. The color contours show the relative values normalized to the value at the center. The bottom panels show the fraction of energy deposit observed in the neighbor tower.

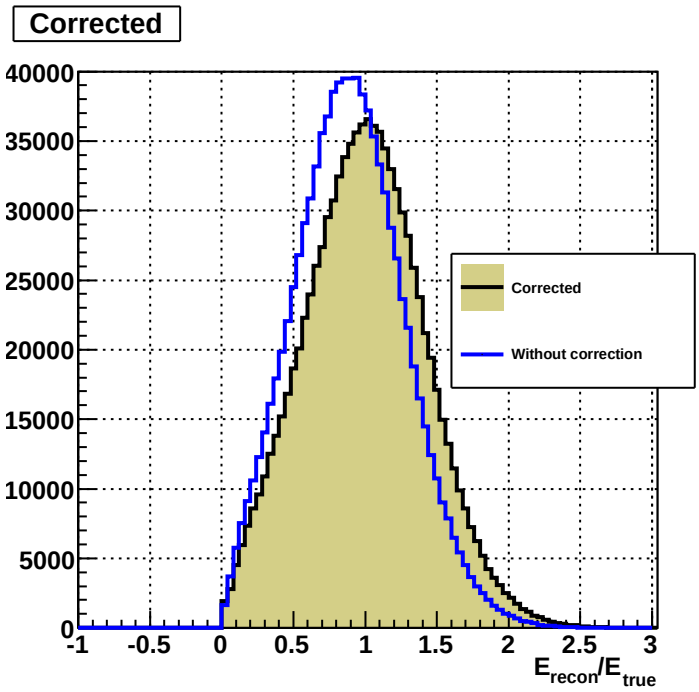

Figure 3.13: The result of the leakage correction. The blue histogram shows the reconstructed energy divided by its true energy without the leakage correction. The hatched histogram shows the one with the leakage correction. The incident neutrons with energy from 100 GeV to 3500 GeV were uniformly injected to the calorimeters.

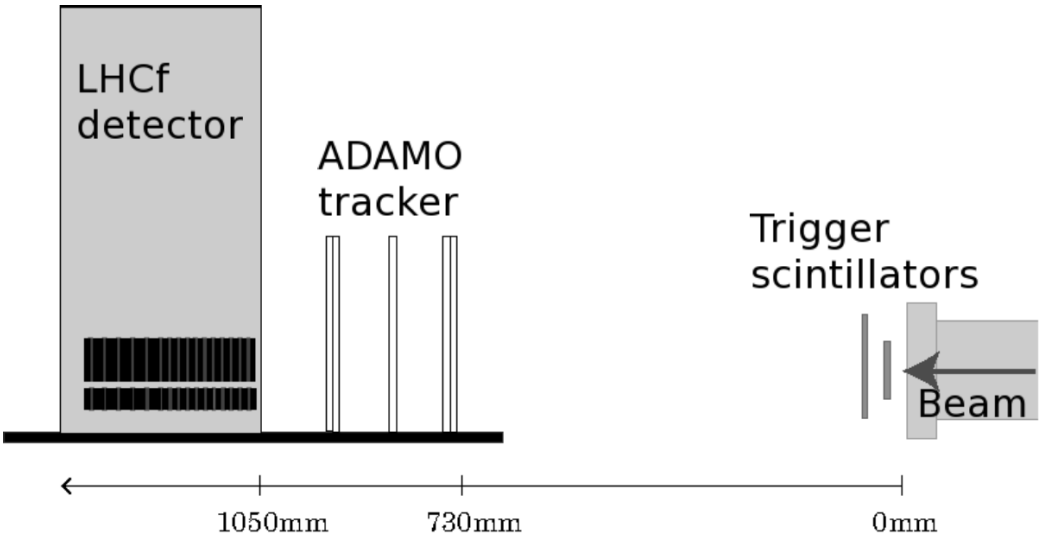

Figure 3.14: The setup of the SPS experiment. The trigger signals were generated by using small scintillators at the exit of beam pipe. The detector was mounted on a movable table together with the ADAMO tracker to scan the calorimeter through the beams.

ratios is almost 1 (0.998). This indicates that the leakage correction surely worked.

3.2 Detector performance tested at CERN SPS

3.2.1 Overview

The performance of the calorimeters for the measurement of hadronic showers was studied in 2007 and 2010 by using 350 GeV proton beams at the CERN-SPS H4 beam line. The Super Proton Synchrotron (SPS) is the second largest accelerator in CERN. The SPS has nearly 7km in circumference and operates at up to 450 GeV. The consistency of the MC simulations was also checked by comparing them with the results of the beam tests.

For the MC simulations, we used the COSMOS and EPICS packages as explained in Chapter 3.1. Figure 3.14 shows the experimental set-up of the SPS test beam experiment. The trigger signals were generated by using the small scintillators (20 mm $\times$ 20 mm and 40 mm $\times$ 40 mm) placed behind the thin beam exit window as shown in the Figure. Then, precise transverse hit positions of the test beam particles were measured by using the ADAMO

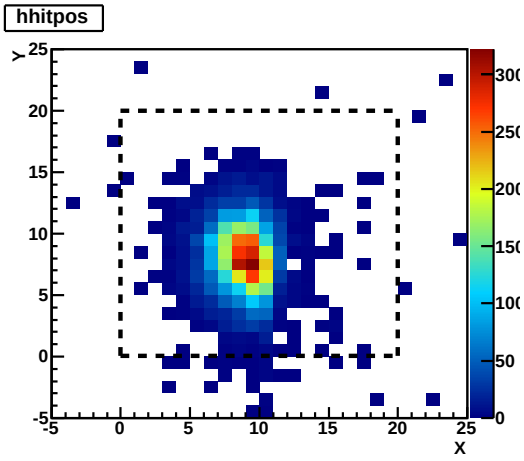

Figure 3.15: The sample of beam profile measured by the ADAMO detector. A dashed line indicates the edge of the 20mm scintillator.

tracker [43] installed in front of the LHCf detector. The ADAMO tracker was composed of silicon strip sensors with position resolution less than 20 μm and had enough resolution to determine the position resolution of the LHCf detectors. The LHCf detector and ADAMO tracker were mounted on a movable table to allow scanning the position of calorimeters through the test beams. The beam position determined by the ADAMO tracker was used for analysis of the data. Figure 3.15 shows the measured beam profile when 350GeV protons were injected. The X and Y axes represent the transverse position coordinates of the ADAMO tracker. To simplify the analysis only the calorimeter leakage-out corrections were applied, but the leakage-in corrections were ignored. For this operation, the high voltages of the PMTs used in the LHCf calorimeters were set at the low gain mode (400-475V). This is similar to the setting of the PMT high voltages during the operation at the LHC.

To reproduce experimental situations, specific MC events were simulated by using the COSMOS7.49/Epics8.81 packages. Neutron incidents of energy 350GeV were used instead of proton beams. The neutrons were injected to the center of Arm1 small tower. The experimental data and the MC simulations were compared after applying the leakage correction.

3.2.2 Analysis procedure

The data analysis was carried out in the following way both for the experiment and the MC simulations. The raw data (measured ADC counts) were

converted into the numbers of MIPs passing through the scintillation layers of the calorimeters after subtracting the pedestal. Conversion of charge measured by the ADCs to the number of MIPs was based on the conversion factor obtained by using electron and muon beams [33].

Pedestal fluctuations due to the electric noises were subtracted for each observed value. The transverse hit position and the longitudinal shower shape described by the $L_{20\%}$ and $L_{90\%}$ parameters were reconstructed. Because it is difficult to reconstruct the events hit at the edge of calorimeter due to large fluctuation of energy resolution, events hit within 2 mm from the edge were removed from the analysis. The offline event selection was applied when the energy deposited in three successive scintillation layers exceeded the energy deposited by 200 MIPs. The PID selection was performed with the method as discussed later in Chapter 5.2.1. Finally, as same as previously discussed for the MC analysis, the energy and transverse momentum was reconstructed.

The accurate hit positions were determined by the ADAMO detector in the experimental analysis. The difference of the cable attenuation effect between the operations at SPS and LHC was also taken into accounts.

3.2.3 Results

In this section the analysis results of the Arm1 detector only were described, but we confirmed that the results of Arm2 analysis were also consistent with those of Arm1.

Position resolution of SciFi

To correctly understand the performance of position determination is very important to measure the p_T dependence of the neutron production. The position resolutions obtained from the experimental data were compared with MC predictions.

The black points in Figure 3.16 show the distribution of the difference between the SciFi measured hit position and the beam hit position determined by the ADAMO tracker. Histograms correspond to the position resolution estimated by the MC simulations. The left (right) panel shows the results for the X (Y) coordinate. The resolution of the ADAMO tracker due to the readout pitch (20 μm) was not considered in this plot. In the neighborhood of the peaks the data and MC simulations are consistent, but the experimental data contains more tail component which does less appear in the simulations. These tail component affect fiducial area definition. The difference of tail component between the data and the MC was taken into account as systematic error as shown in Chapter 5.3.5.

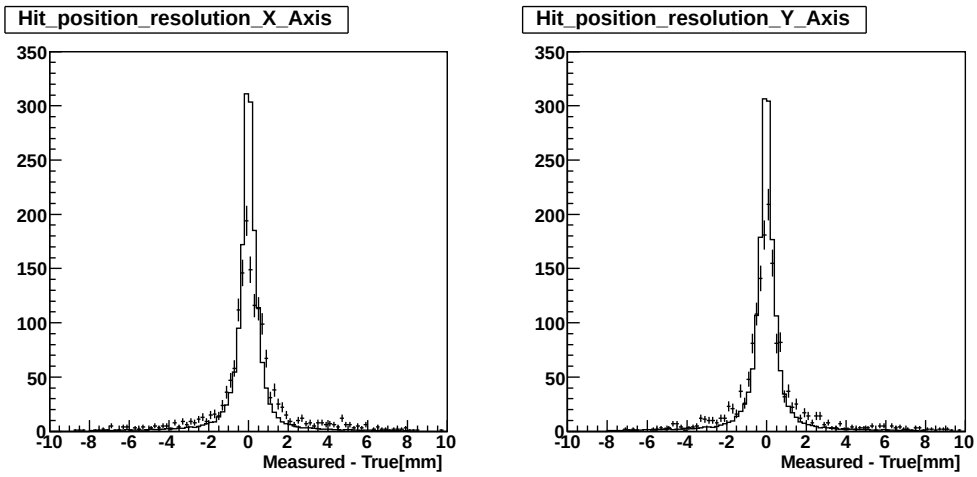

Figure 3.16: The difference between the SciFi measured hit position and "true" hit position measured by the ADAMO tracker in the case of a 350 GeV proton beam for the Arm1 small tower. The left(right) panel is the result for the X (Y) axis. The data points correspond to the experimental data, while the histograms correspond to the MC simulations. For the experimental data, the hit position determined by the ADAMO tracker used as true hit position.

Energy Reconstruction

In case of photon measurement, the absolute energy scale can be calibrated by using two photon invariant mass [37]. However, there is no natural calibration source for hadron measurement in p-p collisions at the LHC except lower energy beams such as the 350 GeV proton beams at CERN-SPS. Hence, consistency between the MC simulations and the beam experiment have to be confirmed.

The energy deposited in each scintillation layer were compared with the MC prediction. To reproduce the actual experimental conditions, the measured pedestal fluctuations were considered in the MC simulations. Figure 3.17 shows the deposited energy distribution in the scintillation layers of the small tower for the 350 GeV proton beam data and for 350 GeV neutrons simulated by MC calculations. The MC results reproduced the experimental results well. The difference between the data and the MC prediction is summarized in Table 5.3. In this table, the Ratio for i-th layer r^i was calculated as,

$$r^i = <dE^i_{Ex}>/<dE^i_{MC}>, \tag{3.8}$$

where $< dE^i_{EX} >$ and $< dE^i_{MC} >$ are the average energy deposit in the i-th layer for the experiment and the MC, respectively. Possible reason for the differences in the r^i from unity is uncertainty of the hadronic interaction length of the tungsten plates or the gain calibrations performed in the previous study [33].

Figure 3.18 presents comparison of the sumdE distribution for the 350 GeV SPS proton beam data and MC simulation of 350 GeV neutrons. The black symbols are the experimental data, while the red and blue histograms are the MC predictions with the DPMJET 3.04 and QGSJET II-03 model, respectively. The mean, standard deviation (σ) of sumdE and their ratio (σ/mean) are summarized in Table 3.3. The ratios of the mean values of the MC with respect to the experimental data are also shown. The QGSJET II-03 model has the mean and standard deviation of the sumdE similar to those for the experimental data. On the other hand, the DPMJET 3.04 model clearly underestimates the width of the distribution especially at the high energy tail. From this fact, we concluded that the QGSJET II-03 model was more appropriate model to simulate hadronic interactions in the detector simulation.

The +3.5% (-6.5%) difference in sumdE for Arm1 (Arm2) between the experimental 350 GeV proton data and the MC simulation with the QGSJET II-03 model will be included as a part of the systematic uncertainties when we reconstruct the incident energy based on the functions as shown in Equations 3.2 and 3.3.

3.2.4 Longitudinal shower development

The parameters, $L_{20\%}$ and $L_{90\%}$ that represent the longitudinal development of showers [36], were obtained from the shower transition shape. Here, the $L_{20\%}$ and $L_{90\%}$ parameters are the calorimeter depths in which containing 20% and 90% of the total deposited energy, respectively. A two dimensional PID selection with $L_{20\%}$ and $L_{90\%}$ parameters was employed to perform PID more efficiently with less contamination. An optimized parameter L_{2D} defined as $L_{2D} = L_{90\%} - 1/4 \times L_{20\%}$ was introduced. Hadronic showers are more penetrating than electromagnetically induced showers so that contamination by electrons would show up as an excess of events with low values of the L_{2D} parameter. The detail of the PID process was discussed in later Chapter 5.2.1. Figure 3.19 shows the distribution of the L_{2D} parameter for the 350 GeV proton data (the black markers) and the MC simulation (the hatched histogram). The agreement between the MC prediction and the experimental data is quite satisfactory, χ^2/NDF is about 31.5/28 taking into account the statistical uncertainties). Therefore there seems to be no significant contamination in the proton beam by positrons. Dashed red line shows L_{2D} distribution of pure photons. The arrow at $L_{2D} = 21$ indicates the PID selection criteria.

3.3 Summary

In order to carried out the analysis for neutron events from the LHC $\sqrt{s} =$ 7 TeV *p*-*p* collisions data, the performance of the LHCf detectors for hadron shower measurement were studied by using 350 GeV proton test beams and MC simulations. We compared two different MC configurations using DPMJET 3.04 or QGSJET II-03 hadronic interaction models, and found that the QGSJET II-03 model can reproduce the experimental test beam result at CERN-SPS more precisely. The detection efficiency is greater than 70% for neutrons above 500 GeV for both towers of the Arm1 and Arm2 detectors. The incident energy of neutrons can be estimated by using the total energy deposited in the calorimeters with the energy resolution about 40% above 500 GeV and $\pm$2% non-linearity of the energy scale is confirmed. The resolution on the transverse hit position is less than 1 mm above 500 GeV and decreases slowly with increasing energy. The absolute energy scale was checked by comparing the sumdE distribution of the SPS data with the MC simulations. The 3.5% and 6.5% difference in sumdE between the experimental result and the MC prediction with the QGSJET II-03 model was found, and it was included as a part of systematic uncertainties.

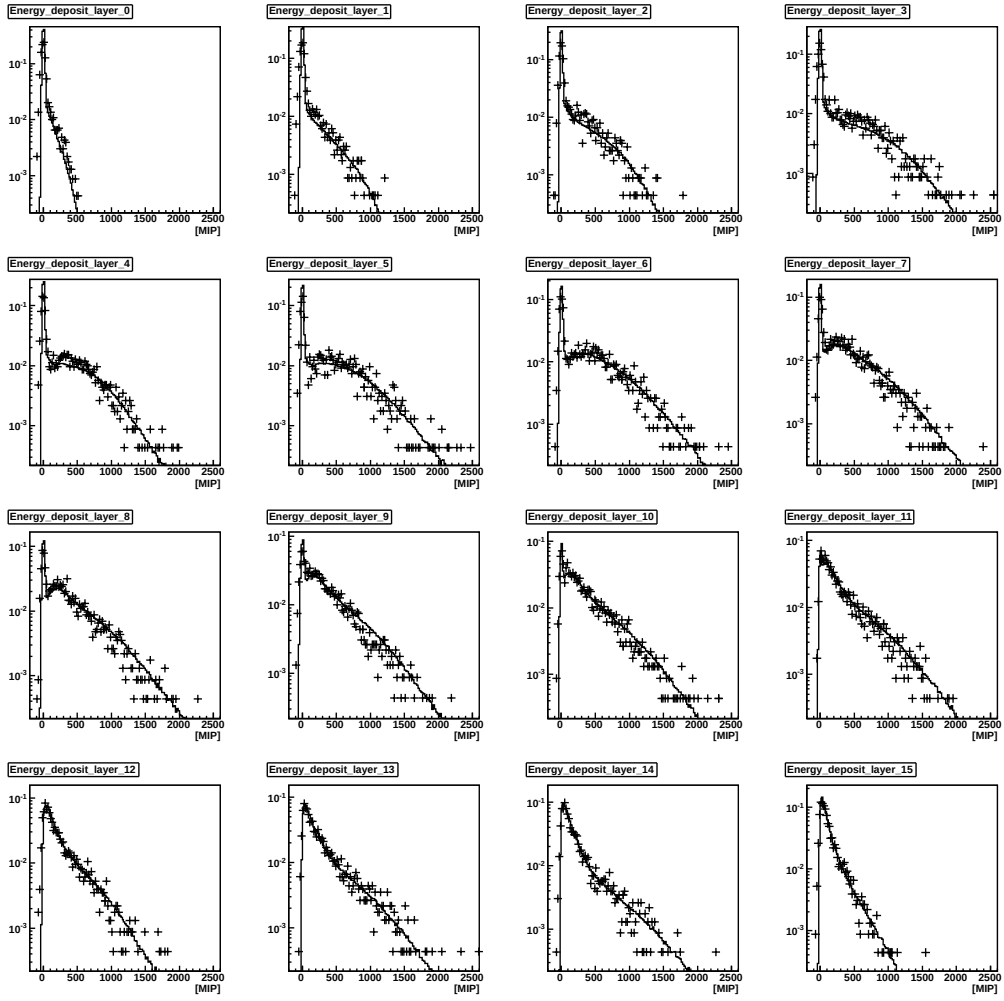

Figure 3.17: The deposited energy distribution in each scintillation layer of the Arm1 small tower for the 350 GeV SPS proton test beam. The black data points indicate the experimental results. For comparison MC simulations for 350 GeV neutrons are overlaid as solid black line histogram.

Table 3.2: The ratios of measured energy deposited by 350 GeV SPS protons to the MC simulation of energy deposited by 350 GeV neutrons for all the layers of Arm1 small tower.

Layer	Ratio	Layer	Ratio	Layer	Ratio	Layer	Ratio
0	1.1577	4	1.0370	8	0.8726	12	0.9064
1	0.9998	5	0.9965	9	0.8483	13	0.9785
2	1.0336	6	0.9625	10	0.9117	14	0.8842
3	1.0262	7	0.8904	11	0.8582	15	0.8942

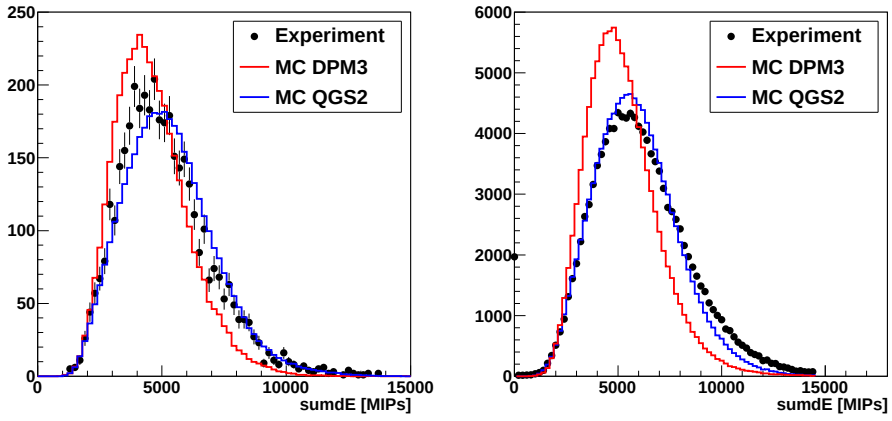

Figure 3.18: Comparison of the sumdE distributions for the 350 GeV proton data and 350 GeV neutron MC simulations. The black symbols are the experimental data. The red and the blue histograms represent the MC results with the DPMJET 3.04 model and the QGSJET II-03 model, respectively. The left (right) figure corresponds to the result of the Arm1 (Arm2) small tower.

Table 3.3: Mean, σ, σ/Mean and Ratio (MC/Experiment) of sumdE distributions for the experimental 350 GeV proton data and the MC results for 350 GeV neutrons with the DPMJET 3.04 and QGSJET II-03 hadronic interaction models.

		Mean [MIPs]	σ	σ/Mean	Ratio
Arm1	Experiment	5116	1840	0.360	-
	MC DPMJET 3.04	4590	1484	0.323	0.897
	MC QGSJET II-03	5294	1822	0.341	1.035
Arm2	Experiment	6022	2379	0.395	-
	MC DPMJET 3.04	4968	2010	0.405	0.825
	MC QGSJET II-03	5631	2284	0.406	0.935

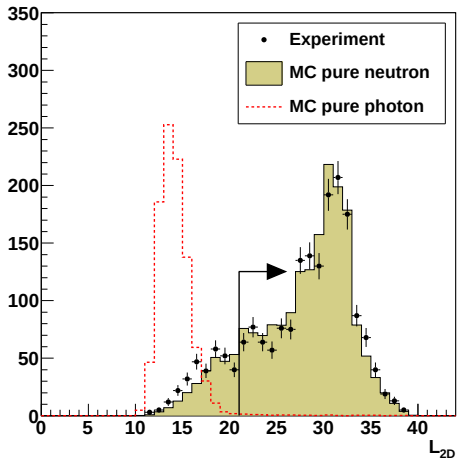

Figure 3.19: Comparison of the L_{2D} distribution for the 350 GeV proton test beam and the MC prediction for the Arm1 small tower. Black crosses show the experimental data and the histogram shows the MC prediction. Dashed red line indicates L_{2D} distribution of pure photons. Arrow shows the PID selection criteria in this analysis.

Chapter 4

Spectrum unfolding method

4.1 Overview

The measured observable are different from the true values due to the finite resolution of detectors in any experiments. The energy distribution of neutrons measured by the LHCf detectors were also smeared by the energy resolution of about 40%. Of course the absolute neutron yield is one of the important parameters to calibrate the hadronic interaction models, but it does not provide detail features of the neutron production process. If we can reveal the production spectra, it may give reliability to the models to extrapolate them to higher energy. In order to extract the true distributions, unfolding detector resolutions and biases is quite an important process.

Here a brief explanations of unfolding method is described in the standard unfolding methods. Assuming the measured distribution $\vec{M} = M_i$ can be expressed by a linear combination of the original distribution $\vec{T} = T_j$ as below,

$$\vec{M} = R\vec{T}. \tag{4.1}$$

Here, $R = (R_i^j)$ is a response matrix. The matrix element R_i^j represents the probability that T_j is measured as M_i due to the resolution effect. The aim of unfolding is to obtain true distribution $\vec{T}$ by using the measured distribution $\vec{M}$ and the response matrix R. The response matrix can be derived by using a training simulation. Firstly, R is diagonalized into D by using a transformation matrix U as $D = U^{-1}AU$. Then Equation 4.1 can be expressed using D, $\vec{m} = U^{-1}\vec{M}$ and $\vec{t} = U^{-1}\vec{T}$,

$$\vec{m} = D\vec{t}. \tag{4.2}$$

Here components of D and each of the column of U are the eigenvalues ϵ_j and the eigenvector of the matrix A, respectively. Thus each coefficient m_i

and t_i in Equation 4.2 can be expressed by,

$$m_i = \epsilon_i \cdot t_i. \tag{4.3}$$

Finally, each component of $\vec{t}$ which includes true information can be expressed by the relation of $t_i = m_i/\epsilon_i$. This method is called the invert matrix method. However, in case that the resolution is not small, such as the LHCf neutron measurements, the results are very sensitive to small change of ϵ. Statistical fluctuations are also ignored in this explanation. The treatment of the statistical fluctuations is also important issue because the statistical fluctuation associates with a instability on the unfolded results. In order to overcome these problem, we used the multi-dimensional spectra unfolding method based on the Bayesian theory [44] as discussed in the next section.

4.2 Two dimensional unfolding method

The performance of the multi-dimensional unfolding method for the LHCf neutron analysis was studied. The method consists of the training and the test processes. The detector response matrix was estimated by using specific MC simulations at the training process. Then, using the obtained response matrix the measured spectra was unfolded at the test process.

We found that the unfolding results slightly depend on the initial distribution of the training samples. Figure 4.1 shows the unfolded neutron spectra at the LHCf Arm1 small tower by using different training samples (DPMJET 3.04, EPOS 1.99, PYTHIA 8.145, QGSJET II-03, and SYBILL 2.1). The tested sample was preliminary neutron spectra measured by the Arm1 small tower as discussed later in Chapter 5. The colored points represent the difference of the training sample. The neutron energy distributions generated by the several interaction models were employed as the training sample. The black points correspond to the average of the all models. The right panel shows the ratio to the averaged sample. It was found that the unfolded spectra had a similar shape with the training sample. Although the dependence on the training sample were about 20%, it associated with small model dependence (or bias) for the final conclusion. In case that the actual neutron energy distribution is completely different with the model predictions, it is difficult to estimate the systematic effects from the unfolding process.

To unfold the measured spectra with minimum biases, specific MC simulations with neutrons of energy ranged from 50 to 3500GeV and with uniform transverse hit positions were generated. They were used as the actual training sample for the unfolding method in the analysis of $\sqrt{s} = 7$ TeV p-p collision

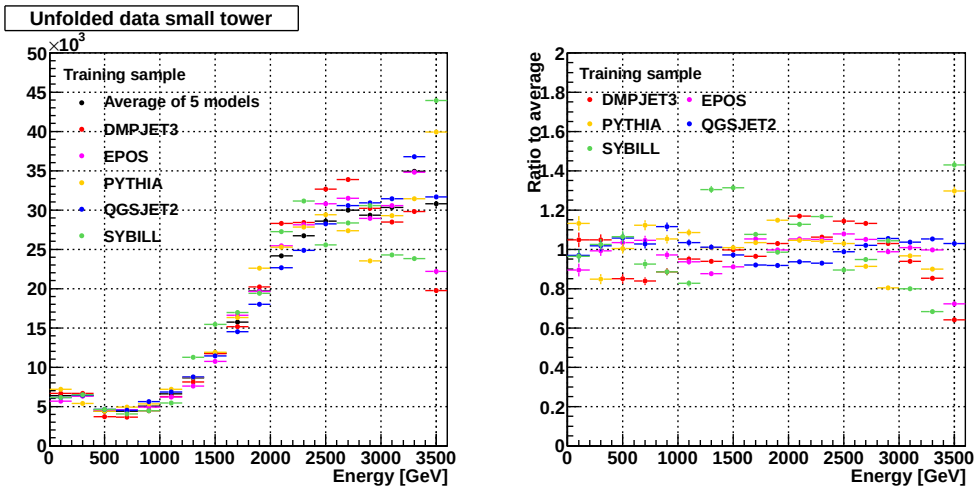

Figure 4.1: Unfolded neutron spectra measured by the arm1 small tower with different training sample (left). The black points correspond to the average of the five models. Right panel shows the ratio to averaged spectra.

data. The events in the training samples taking full detector response into considerations were reconstructed as the same manner as the data analysis. The same event selections, such as the offline trigger, the fiducial area selections and the reconstructed energy selection corresponding to 100 GeV were applied. Figure 4.2 shows the energy and p_T distributions for the training sample. Upper panels show the scatter plot of the energy and p_T, while the middle panel and the bottom panels are the projections to both the X and Y axes. The full detector response was considered in the left three panels. On the other hand, MC true values were used in the right three panels. The energy distribution in the plot was not uniform, because the detection efficiency depending on the incident energy was taken into account, although the generated energy distribution was uniform.

We checked the performance of the unfolding method by applying this method to the MC spectra taking into account the full detector response. Figures 4.3, 4.4, and 4.5 show the unfolded spectra (markers) and its true spectra (histogram) for each model for each fiducial area as explained in Figure 5.1. Each bottom panel shows the ratio of unfolded spectra to the true spectra. Note that the error bars are statistical only.

We found unfolding biases due to the difference of the initial energy and the p_T distributions between the training sample and the tested samples. The discrepancy between the unfolded spectra and true spectra is about 10-100% for each model. Because the training sample much harder than each

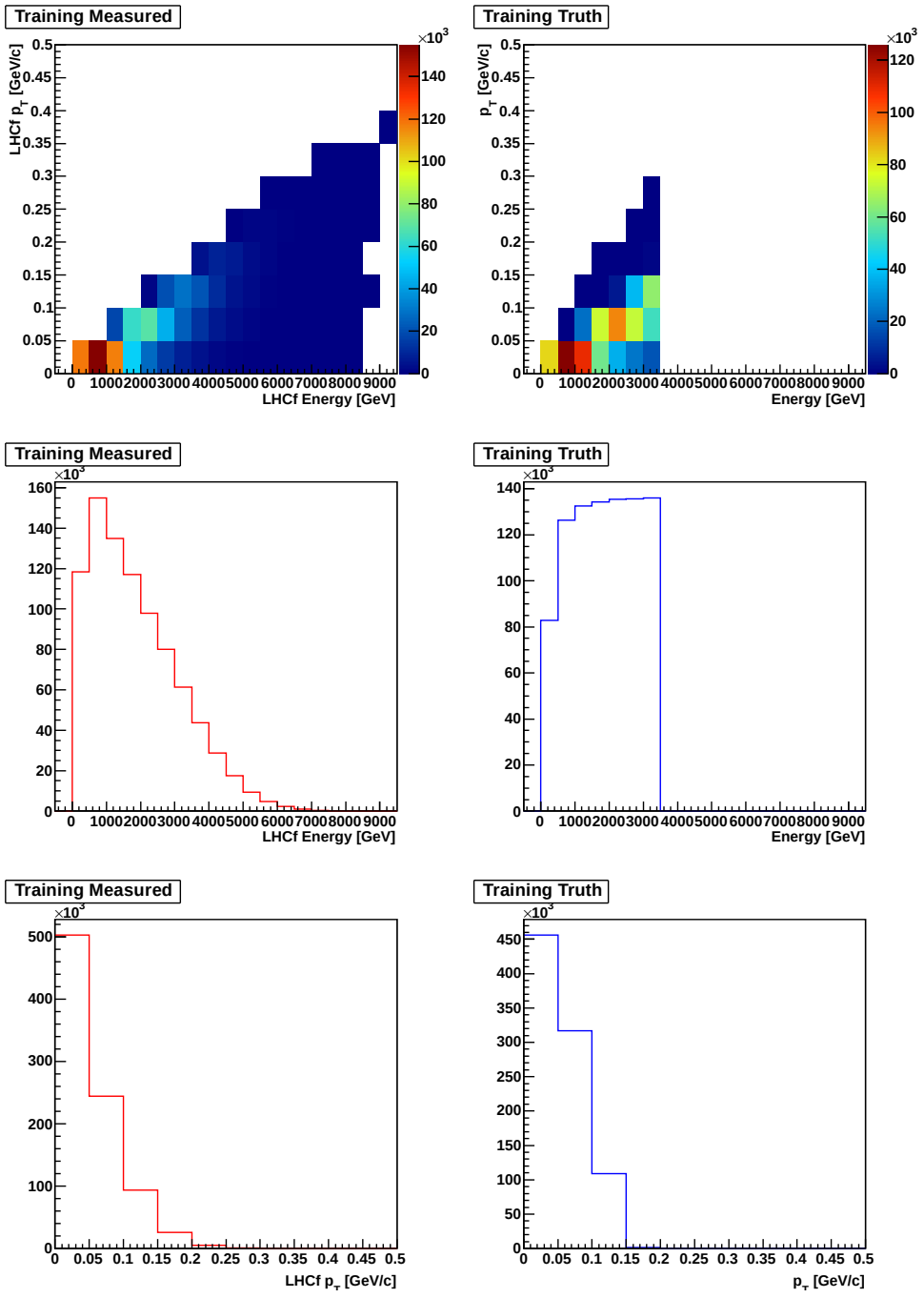

Figure 4.2: The training sample used in this study. The left panels show the measured energy and p_T distribution and the projections to the X (middle) and the Y (bottom) axes of the training sample. The right panels show the true energy and p_T distribution and the projections to the X (middle) and the Y (bottom) axes of the training sample.

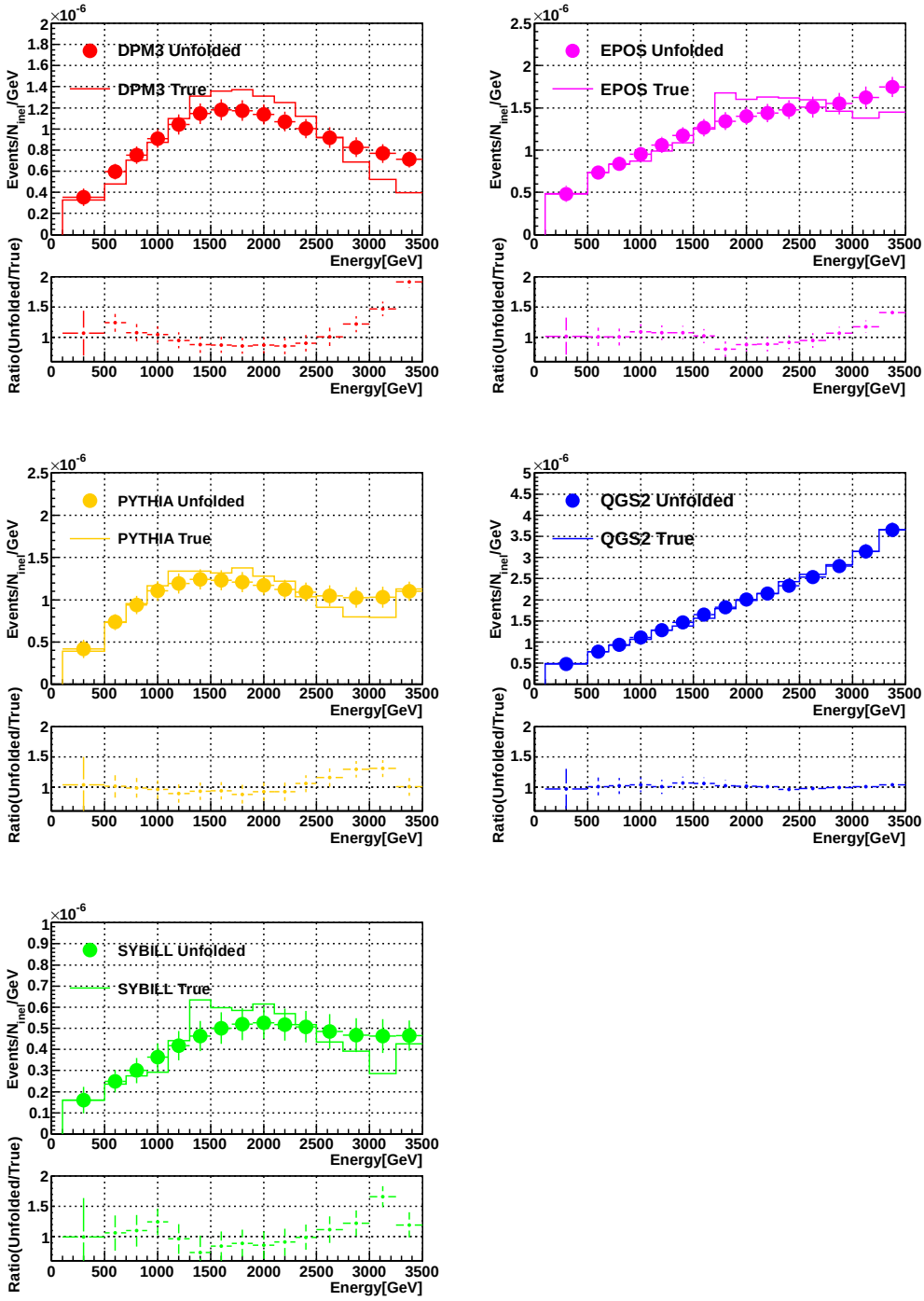

Figure 4.3: The unfolded spectra and the true spectra for the DPMJET 3.04, the EPOS 1.99, the PYTHIA 8.145, the QGSJET II-03, and the SYBILL 2.1 models at the small tower of Arm1. Bottom panels show the ratio to the true spectra.

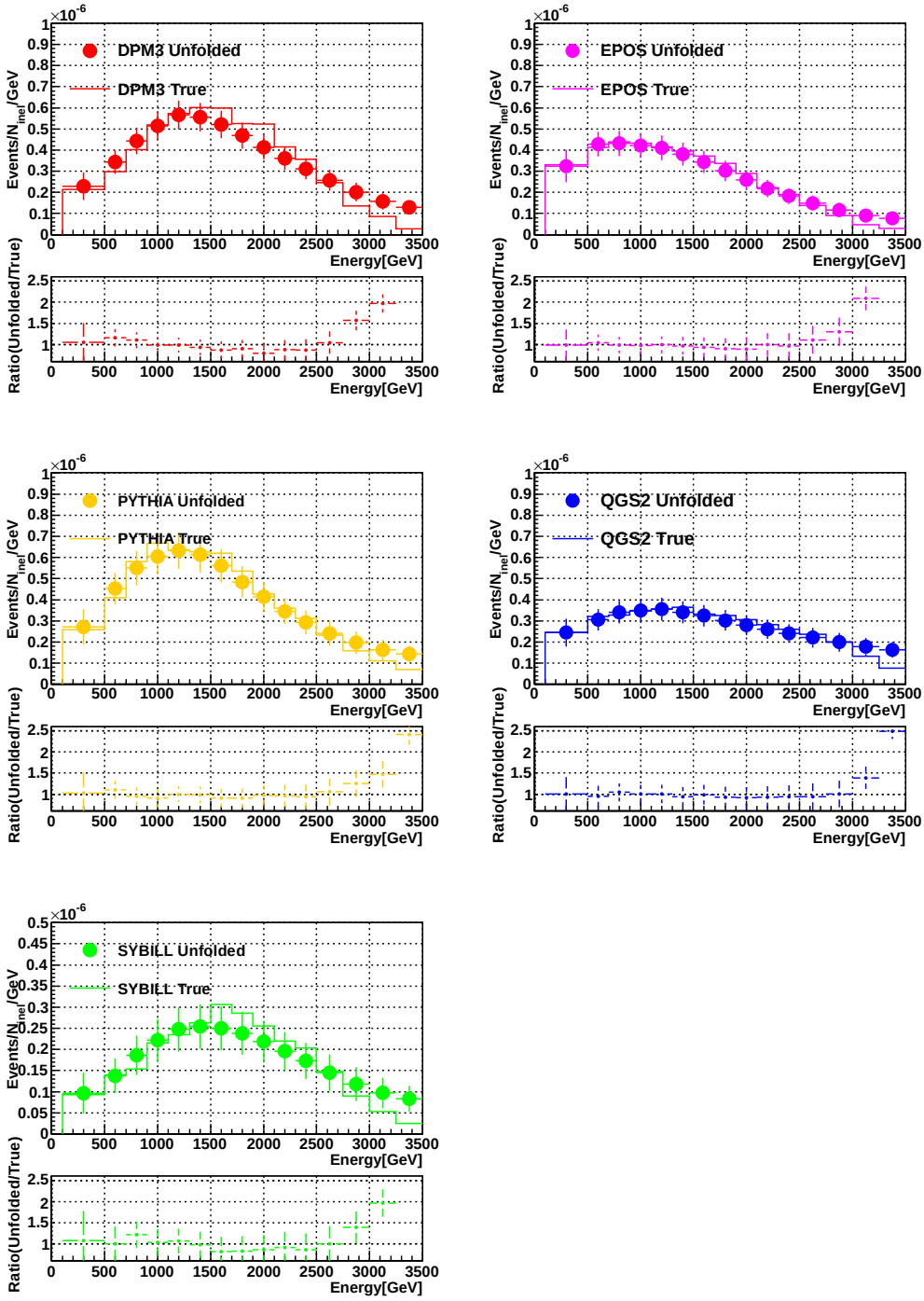

Figure 4.4: The unfolded spectra and the true spectra for the DPMJET 3.04, the EPOS 1.99, the PYTHIA 8.145, the QGSJET II-03, and the SYBILL 2.1 models at the large tower A of Arm1. Bottom panels show the ratio to the true spectra.

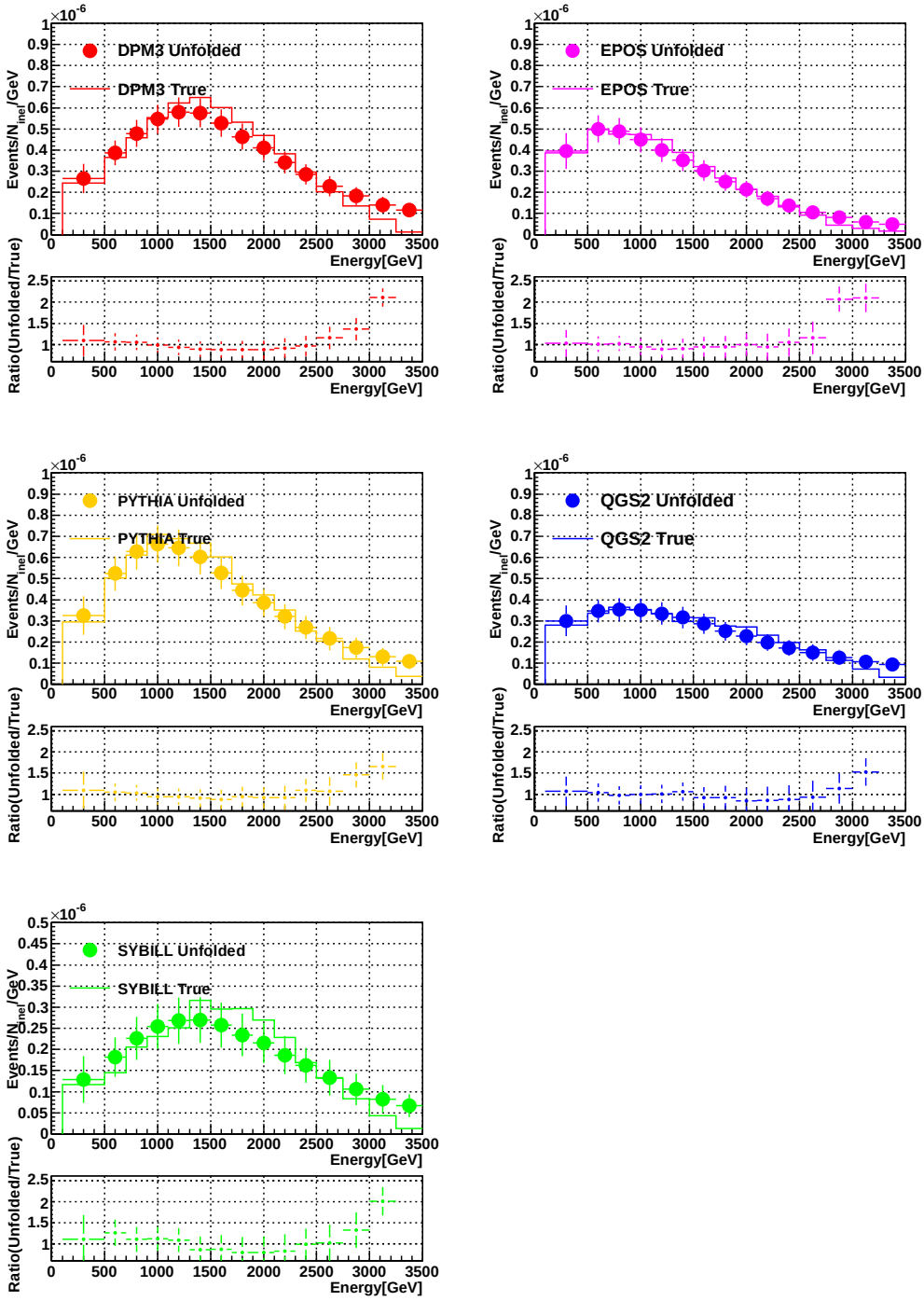

Figure 4.5: The unfolded spectra and the true spectra for the DPMJET 3.04, the EPOS 1.99, the PYTHIA 8.145, the QGSJET II-03, and the SYBILL 2.1 models at the large tower B of Arm1. Bottom panels show the ratio to the true spectra.

Table 4.1: The Mean and RMS values for the true spectra and unfolded spectra.

	Mean	RMS
True spectra	**2778**	365
Unfolded spectra	**2790**	396

model in this study, the unfolded results indicated large deviation in the highest energy bin. It is also found that to reproduce small peaks such a sharp peak near 3.5TeV predicted with several models using finite statistics of the unfolding sample is difficult, because of the large fluctuation of energy resolution. However, the discrepancy between the unfolding results and its true spectra was not strongly depend on the models. Hence, the average of the discrepancy of each model was considered as the bias correction.

Figures 4.6, 4.7, and 4.8 shows the bias corrected unfolding spectra together with its true spectra. The vertical bars represent the model to model fluctuations calculated as standard deviation of the discrepancies in each binning, and these were considered as unavoidable systematic uncertainties caused by unfolding processes. By applying the bias correction, it is possible to reconstruct the true distribution with 10-60% accuracy depending on the energy.

4.3 Energy resolution upper limit

When comparing the LHCf results with the results of previous experiments such as the results of PHENIX experiment which has a sharp structure in the spectra, an important issue is whether we are able to reconstruct a sharp peak correctly by the unfold method used in this study, because this unfolding method cannot reproduce a sharp structure due to the large energy resolution of about 40%. In order to estimate the performance of this unfolding method with respect to the reconstruction of a sharp peak, it was tested by using the artificial spectra which have a sharp peak as same as the PHENIX results. The blue histogram in left panel of Figure 4.9 shows the artificially generated energy spectra according to the ISR-like PDF (probability density function), and the red histogram in the right panel shows the measured spectra simulated with the full detector response. The red points in the left panel shows the unfolded result by using the two dimensional unfolding method. The mean and rms of both the true spectra and unfolded spectra are summarized in Table 4.1. We found that the unfolding method

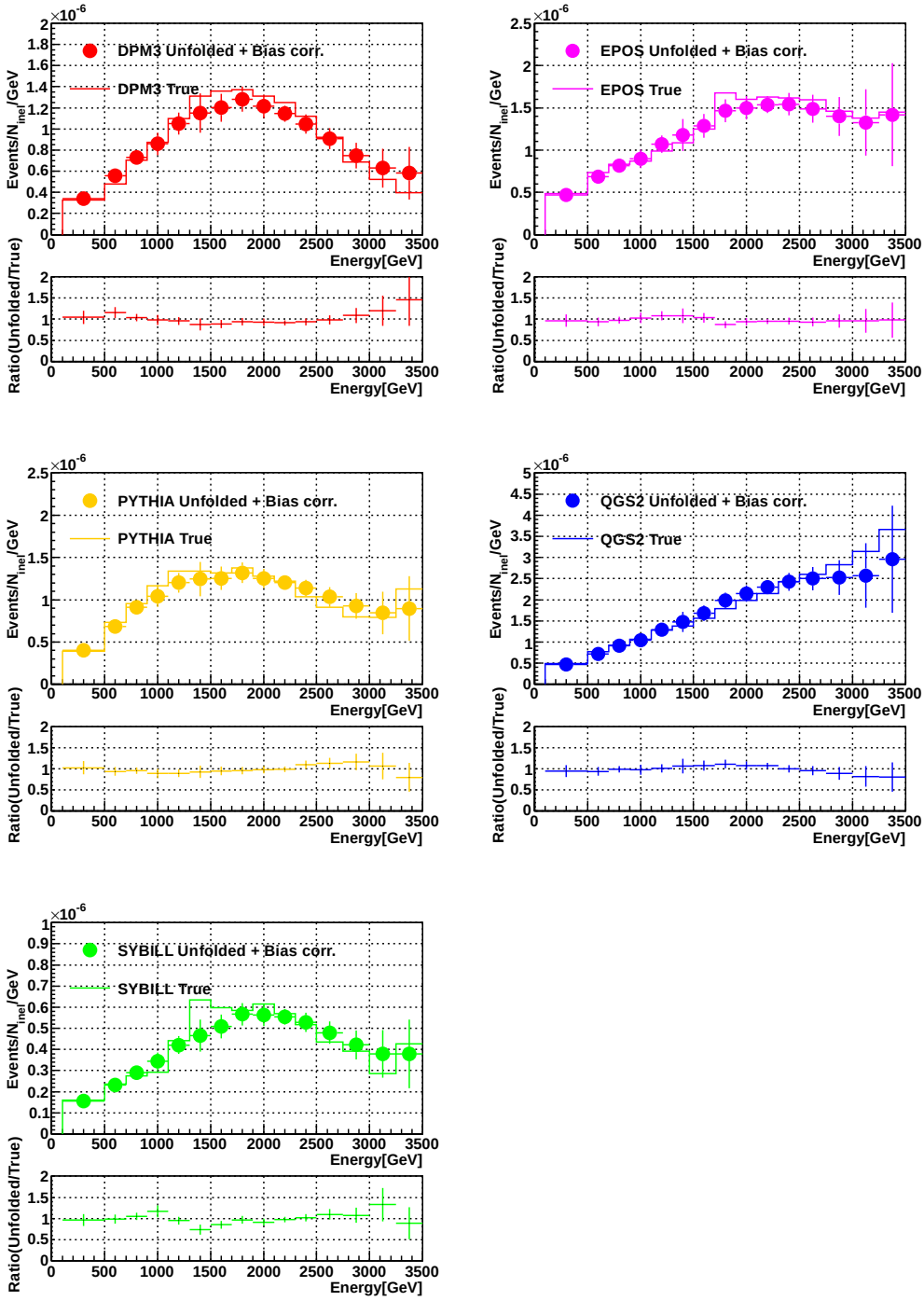

Figure 4.6: The unfolded spectra applying the bias correction and the true spectra for the DPMJET 3.04, the EPOS 1.99, the PYTHIA 8.145, the QGSJET II-03, and the SYBILL 2.1 models at the small tower of Arm1. Bottom panels show the ratio to the true spectra.

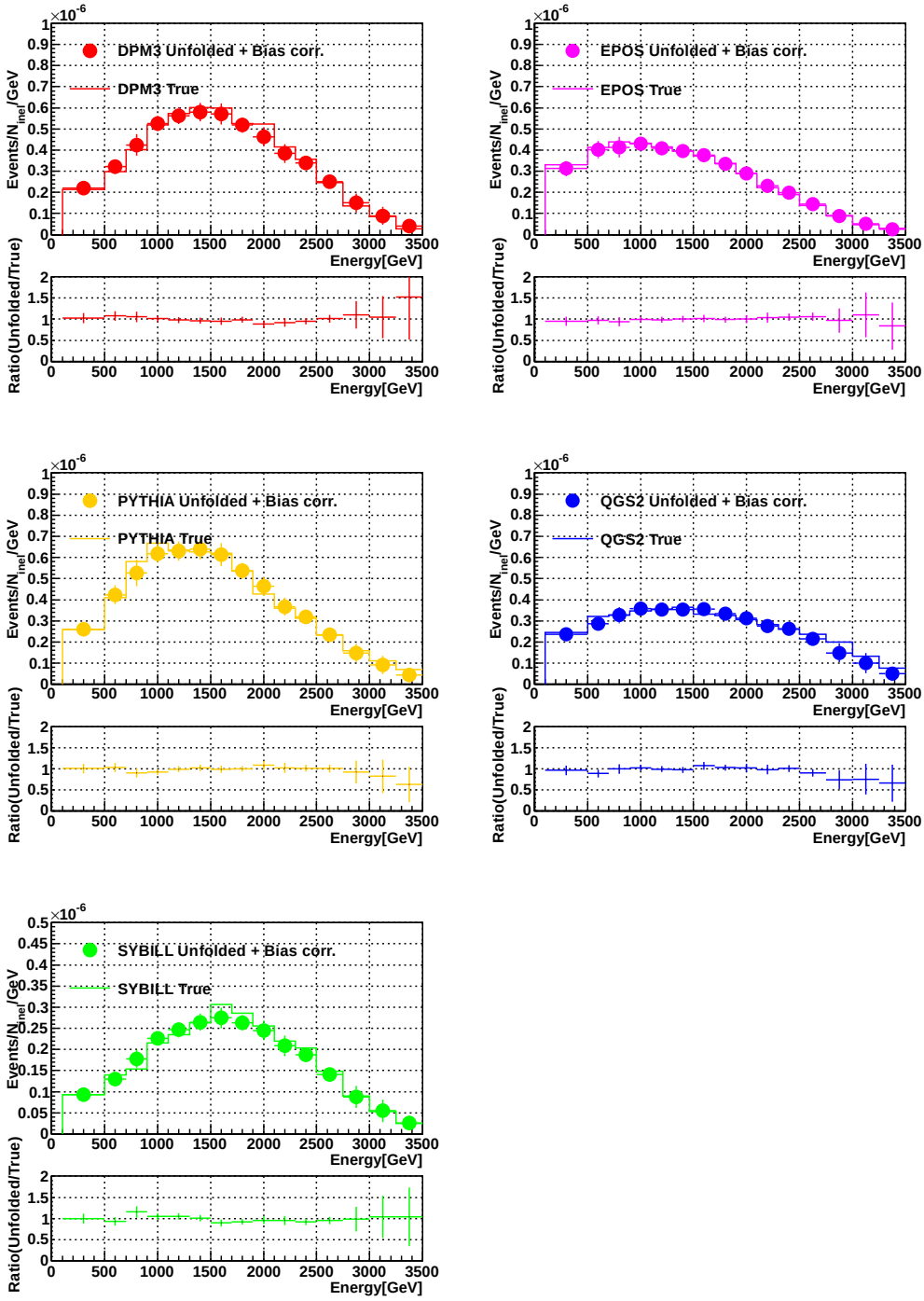

Figure 4.7: The unfolded spectra applying the bias correction and the true spectra for the DPMJET 3.04, the EPOS 1.99, the PYTHIA 8.145, the QGSJET II-03, and the SYBILL 2.1 models at the large tower A of Arm1. Bottom panels show the ratio to the true spectra.

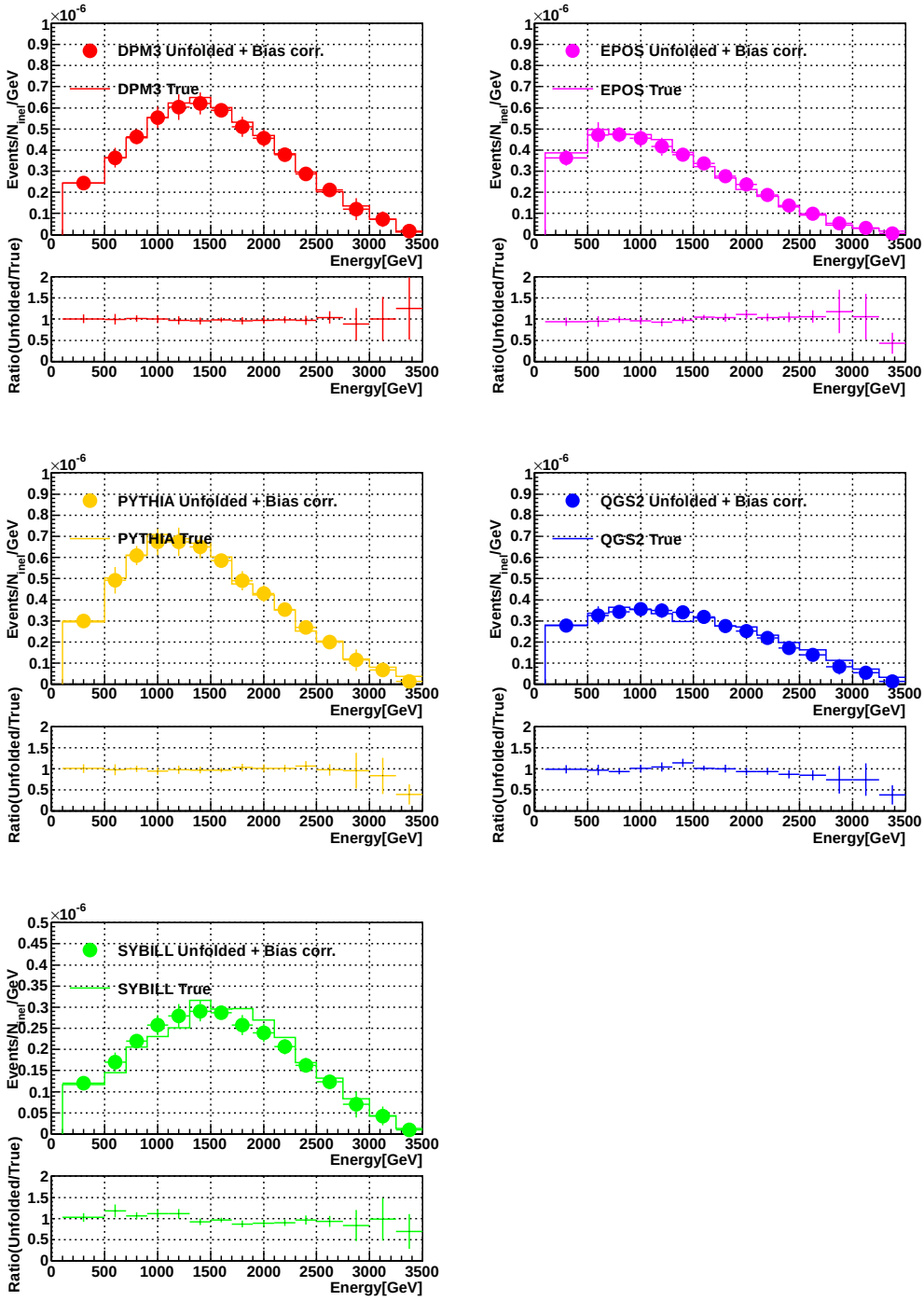

Figure 4.8: The unfolded spectra applying the bias correction and the true spectra for the DPMJET 3.04, the EPOS 1.99, the PYTHIA 8.145, the QGSJET II-03, and the SYBILL 2.1 models at the large tower B of Arm1. Bottom panels show the ratio to the true spectra.

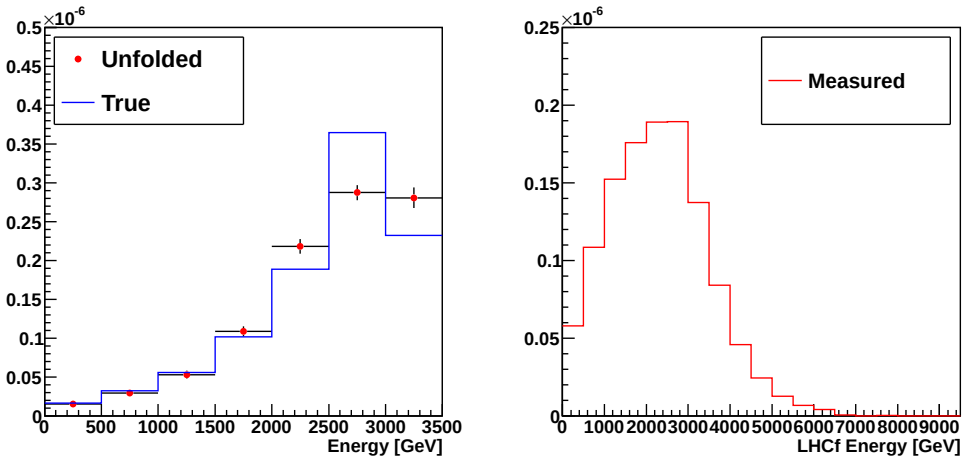

Figure 4.9: The dummy energy distribution made according to the ISR like PDF.

could not reproduce the true distribution in case that the true distribution have such a shape structure. Therefore, we have to taken into account this additional effect. However, because the mean values are quite similar between the true and the unfolded spectra, we can discriminate the unfolded results are consistent with the previous results or not.

As discussed in Chapter 3.2, the energy resolution of the LHCf detectors were tested at less than 350 GeV. On the other hand, the energy resolutions up to 3.5 TeV were estimated by using the MC simulations. If the actual energy resolution in the energy more than 350 GeV is completely different from the MC predictions, the unfolded method cannot reproduce the real spectra, because the training process is depend on the MC simulation. The reliability of the energy resolution was tested by comparing measured energy spectra with artificially smeared spectra. Because the unfolded LHCf spectra have similar shape with ISR results as discussed in Chapter 6.3, the initial energy distribution of LHCf was assumed to be same as ISR. Figure 4.9 shows the dummy energy spectra made according to the ISR like PDF (probability density function). Then each event was smeared by the 35%, 45%, 55% and 65% energy resolution. Figure 4.10 shows the comparison between the LHCf measured spectra and smeared spectra. The black thick line correspond to the measured spectra and the colored lines show the smeared spectra. The spectra smeared by the 55% and 65% resolutions clearly inconsistent with measured spectra. On the other hand, the measured spectra relay between the smeared spectra by the 35% and 45% resolutions. Thus if the true energy distribution of LHCf is similar to the ISR distribution, the

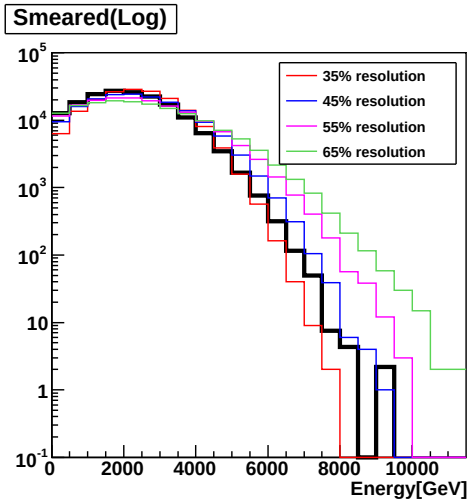

Figure 4.10: Smeared dummy energy distributions (colored lines) and the spectra measured by the LHCf Arm1 small tower (black line).

energy resolutions of the LHCf could range 35% to 45%. This is consistent with the MC estimations.

Chapter 5

Analysis of data for $\sqrt{s} = 7$ TeV p-p collisions at the LHC

5.1 Data used in this analysis

At the end of March 2010, the operation with the LHC p-p collisions at $\sqrt{s} = 7$ TeV were successfully started. The data used in this analysis were obtained on 15 May 2010 during the proton-proton collisions at $\sqrt{s} = 7$ TeV with zero degree beam crossing angle (LHC Fill# is 1104). The typical luminosity corresponding to this fill was $(6.3 - 6.5) \times 10^{28}\text{cm}^{-2}\text{s}^{-1}$ for three crossing bunches. The data taken during a luminosity optimization scan were eliminated from the analysis.

As described in Chapter 2.4, the three levels of the data acquisition triggers were generated in the LHC p-p collisions as following. The first level triggers (L1T) were generated by beam pickup signals from the BPTX (Beam Pick-up Timing for Experiments) installed 170m away from IP1. Shower triggers were generated when any successive 3 scintillation layers of any calorimeters exceeded a predefined threshold. Then the second level trigger for shower events (L2TA) was issued unless the data acquisition system was busy. Data were recorded with the third level trigger (L3T), when all the other types of second level triggers (pedestal, laser calibration, etc.) were combined. The generation of the L2TA and L3T triggers, and hence the data recording, were performed independently for the Arm1 and Arm2 detectors. Data acquisition was carried out under 85.7% (Arm1) and 67.0% (Arm2) average live-times (ϵ_{DAQ}). The live-times were defined as $\epsilon_{DAQ} = N_{L2TA}/N_{shower}$ where N_{shower} and N_{L2TA} are the number of counts in the shower and L2TA triggers, respectively.

The absolute luminosity corresponding to this data set were calculated

by using the Front Counters by using Van der Meer scan method [32]. The integrated luminosity of the data set were 0.68 nb^{-1} and 0.53 nb^{-1} for the Arm1 and Arm2, respectively. The DAQ live-times were taken into account in this estimation. The numbers of inelastic collisions were estimated about 4.86×10^7 collisions for Arm1 and 5.63×10^7 collisions for Arm2, assuming $\sigma_{inel} = 71.5$ mb. Uncertainty of the integrated luminosity directly affects the absolute normalization of the energy spectra. The luminosity corresponding to the data taking period were derived from the counting rate of the Front Counters (FCs) that were installed in front of the LHCf detectors [34]. Considering the uncertainty from the calibration of the FCs [32] and the uncertainty of beam intensity, the systematic uncertainty of the integrated luminosity was assigned to be 6.1% as same as the previous photon study [36].

5.2 Event reconstruction

The basic calibrations such as the conversion to energy deposit from the measured ADC value were already performed with the electron and muon beams below 200 GeV at CERN-SPS as described in Chapter 2.5. The neutron analysis was also based on this calibration.

The event reconstruction procedure were summarized here. At first, the offline event selection which was more than 200 MIPs for successive three layers was applied for this analysis in addition to the experimental trigger. The transverse hit positions of incident particles on the detector were measured by using the position sensitive detectors. Then events hit within 2 mm from the calorimeter edge were removed from the analysis. The position depending lateral shower leakage effects were corrected using the transverse hit position. The longitudinal shower transition shape called transition curve was used in the Particle Identification (PID) process. Finally, incident energy was determined from the total deposited energy in the calorimeter depending on the PID result.

To compare Arm1 and Arm2, the events incident in the common rapidity region were selected as shown in Figure 5.1. Events entered within 6 mm from the beam center were selected for the small tower indicated as a red area in the figure. The large towers of Arm1 and Arm2 were divided into two regions. The inner region, called "Large tower A" (Green) was 28 mm to 35 mm from the beam center, while the outer region, called "Large tower B" (Blue) was 35 mm to 42 mm. The intervals of azimuthal angle were 360° and 20° for the small tower and the large tower, respectively.

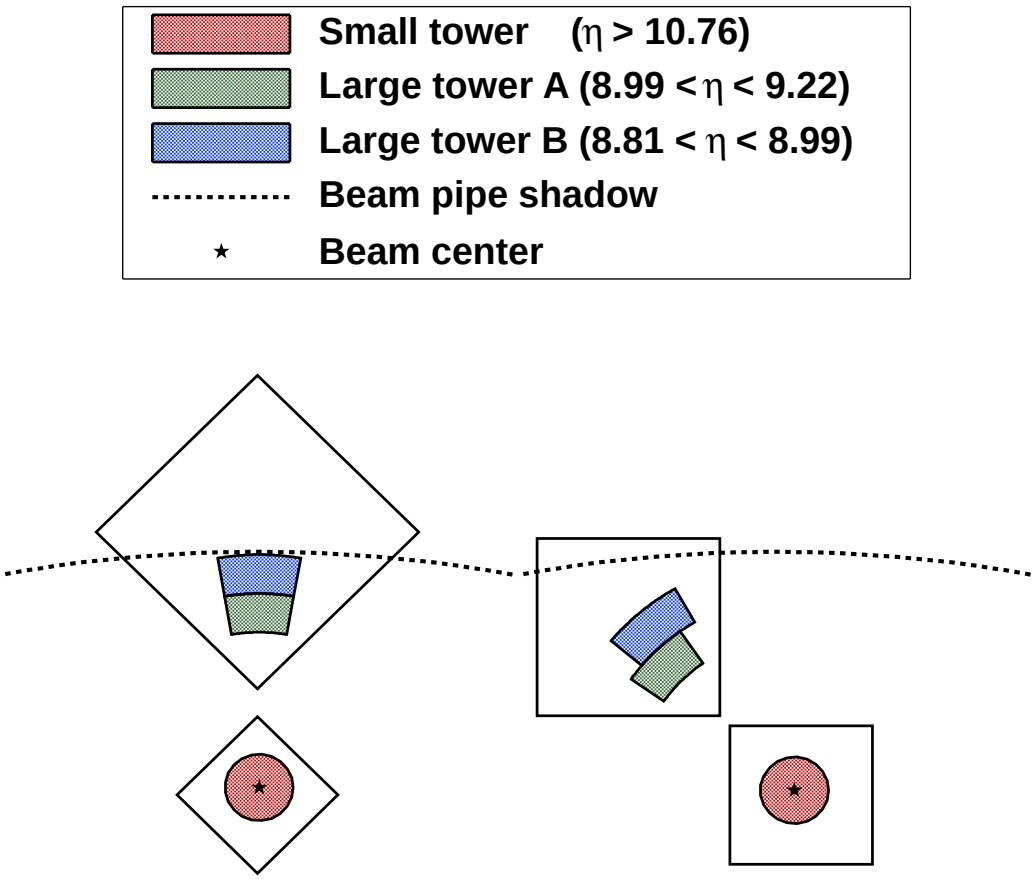

Figure 5.1: Fiducial area used in the combined analysis of Arm1 and Arm2. The left and right correspond to Arm1 and Arm2, respectively. The area above the dashed lines are behind by the beam pipes. The calorimeters divided into three common regions to compensate for the different geometry of the both arms. Here η means pseudo-rapidity. The red area correspond to small tower ($\eta > 10.76$). The green and blue area correspond to Large tower A ($8.99 < \eta < 9.22$) and Large tower B ($8.81 < \eta < 8.99$), respectively.

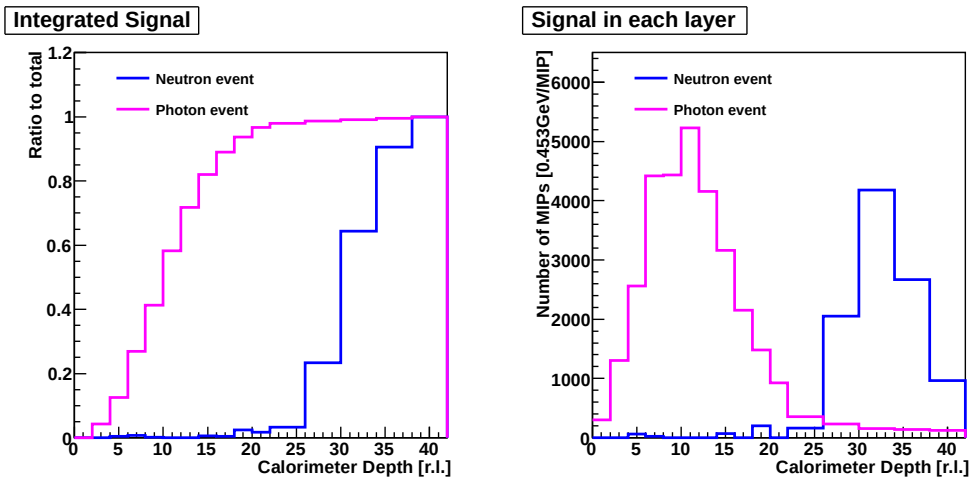

Figure 5.2: Typical transition curves of hadron-like(Blue) and photon-like(Magenta).Left panel is integrated energy deposit, and right is energy deposit in each layer.

5.2.1 PID

Electromagnetic showers can develop shallowly compared with hadronic showers. This difference is quite useful for the PID process and illustrated as Figure 5.2. Figure 5.2 shows typical shower transition curve in the calorimeter for hadron particles (blue curve) and photons (magenta) simulated by the MC simulations. Two simple parameters called $L_{20\%}$ and $L_{90\%}$ were introduced to characterize the transition curves as already discussed in Chapter 3.2.2. The $L_{20\%}$ and the $L_{90\%}$ parameters were defined as the depths containing 20% and 90% of the total deposited energy, respectively. The $L_{90\%}$ parameter can describe a shower depth well, and the $L_{20\%}$ parameter is able to show in which depth shower development started.

Figure 5.3 shows the correlation between the $L_{20\%}$ and $L_{90\%}$ of true photon (left panel) and true hadron (right panel) obtained by theMC simulations. In the $L_{20\%}$ and $L_{90\%}$ distribution for photons, there was a proportional relation between $L_{20\%}$ and $L_{90\%}$ because the longituddinal length of electromagnetic shower is constant given energy. On the other hand, the $L_{20\%}$ and $L_{90\%}$ distribution for hadrons widely spreaded and showed relatively deeper shower development compared to that for the photon distribution.

There are unavoidable contamination of photon events. In order to estimate and correct the PID effect, the purity and efficiency were studied. The efficiency E and the purity P were defined as below for the photon-like

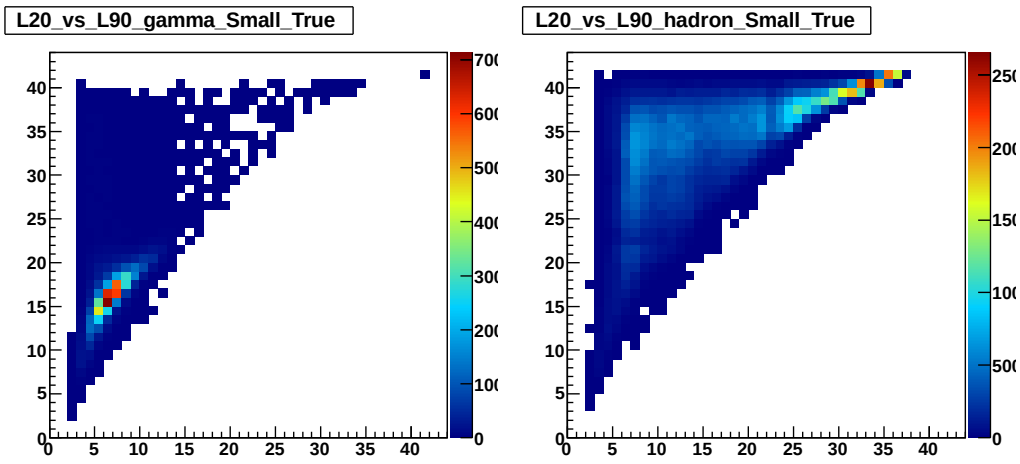

Figure 5.3: The correlation between the $L_{20\%}$ and the $L_{90\%}$ parameters obtained by MC simulation for $\sqrt{s} = 7$ TeV p-p collision with the QGSJET II-03 model. The left panel correspond to photons, while the right is hadron. Horizontal axis shows the $L_{20\%}$ and vertical axis shows the$L_{90\%}$.

events and the hadron-like event;

$$E_{photon} = \frac{N_{good\,photon}}{N_{good\,photon} + N_{bad\,photon}}, \tag{5.1}$$

$$P_{photon} = \frac{N_{good\,photon}}{N_{good\,photon} + N_{bad\,hadron}}, \tag{5.2}$$

$$E_{hadron} = \frac{N_{good\,hadron}}{N_{good\,hadron} + N_{bad\,hadron}}, \text{and} \tag{5.3}$$

$$P_{hadron} = \frac{N_{good\,hadron}}{N_{good\,hadron} + N_{bad\,photon}}. \tag{5.4}$$

There are events which correctly PID-ed as a photon-like event (shown $N_{good\,photon}$ in the above equation) or a hadron-like event ($N_{good\,hadron}$) and a miss PID-ed events ($N_{bad\,photon}$ and $N_{bad\,hadron}$) under a certain PID criteria.

In order to separate two components more efficiently with less contamination, a two dimensional PID method using $L_{20\%}$ and $L_{90\%}$ parameters was employed. The function defined as below was used in this PID cut,

$$f(x) = ax + b. \tag{5.5}$$

The best PID selection parameter (a,b) were chosen so that the efficiency times the purity becomes maximum based on the MC simulation.

The parameter 'a' ranged between 0 to 1.0, and 'b' ranged between 10.0 to 25.0. At first PID efficiency was calculated, then purity was evaluated for the parameter region for the 'a' and the 'b' by which more than 90% efficiency. Figure 5.4 shows the efficiency(left) and the purity(middle) and the product of efficiency and purity(right).

To maximize purity, the parameter 'a' was determined as 0.25. For example, Figure 5.5 shows the case of a = 0.25 and b = 23.5. The red and black points correspond to photon and hadron particles, respectively. Sloped cut in the left panel is equivalent to the vertical cut in the right panel. The right panel is the projection of the 2D histogram in left panel along to the black line. A optimized parameter L_{2D} defined as $L_{2D} = L_{90\%} - 1/4 \times L_{90\%}$ was introduced as mentioned before. Figure 5.5 shows L_{2D} distributions. The black points represent the observed L distribution. The histograms represent the L_{2D} of pure photons (red) and pure neutrons (black).

5.3 Systematic uncertainties

5.3.1 Energy scale and uncertainty from π^0 mass reconstruction

When the both calorimeters in one detector record a single photon shower, the invariant masses of the photon pair were calculated using the energies and transverse impact positions of the two photons assuming their vertex is at the interaction point. In the MC simulations with the full detector response and the analysis process, the reconstructed mass had peak at 135.2 ± 0.2 (stat) MeV in Arm1 and 135.0 ± 0.2(stat) MeV in Arm2, corresponding to the π^0 meson mass [45].

On the other hand, the reconstructed invariant mass of photon pairs of the experimental data were 145.8 ± 0.1 (stat) MeV (Arm1) and 140.0 ± 0.1 (stat) MeV (Arm2). The 7.8% and 3.8% invariant mass excess compared to the π^0 mass reconstructed in the MC simulations were found. A part of the invariant mass excess could be explained by the well understood systematic uncertainties of the absolute energy scale which estimated to be ±3.5%. This 3.5% systematic error was dominated by the errors in the conversion factors of measured charge to deposited energy and the errors in corrections for non-uniform light collection efficiency. Uncertainties in determining the opening angle of a photon pair and the shower leakage-in correction, typically ±1% and ±2% respectively, were also sources of error in the mass reconstruction. The squared sum of these known elements correspond to a systematic mass shift by 4.2% and can not explain the mass excess for Arm1.

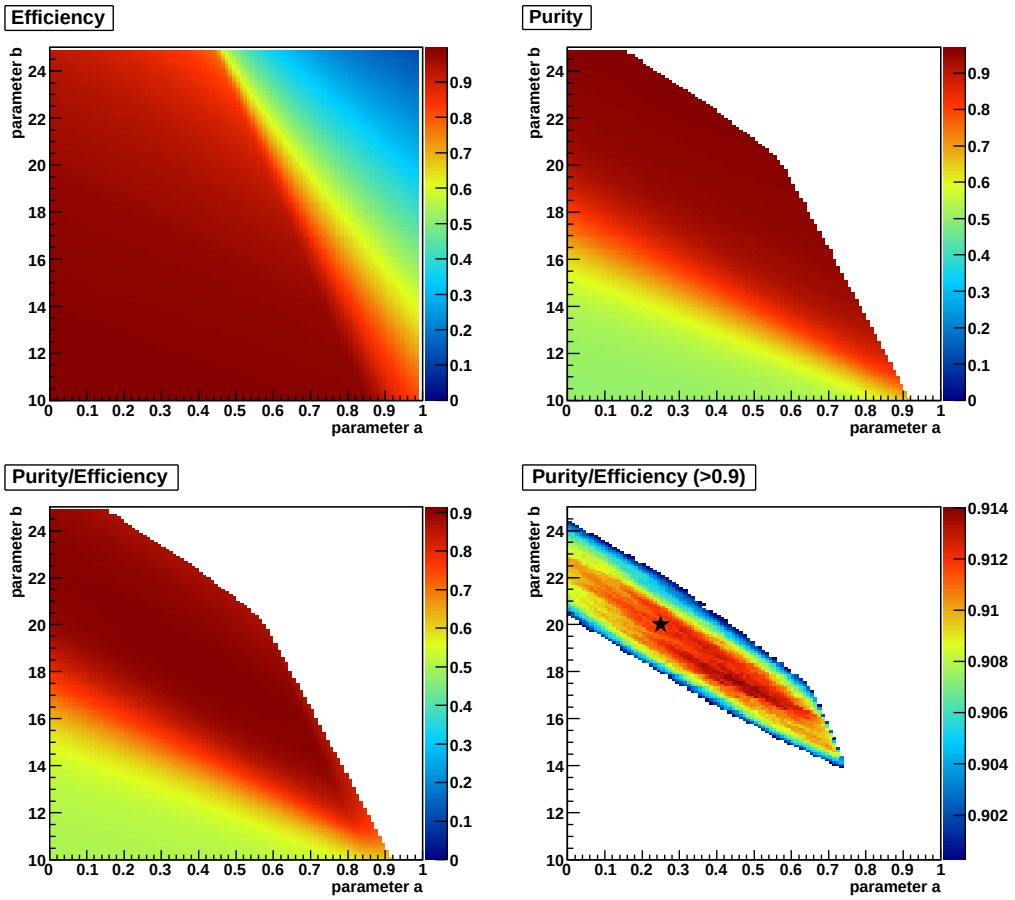

Figure 5.4: The efficiency and purity as functions of the parameter 'a' and 'b' in the function f(x) = 0.25x + 23.5. The upper left panel corresponds to the efficiency, while the left corresponds to the purity for the parameter region for the 'a' and the 'b' by which more than 90% of the efficiency. The bottom panels correspond to the purity divided by the efficiency. In case that Purity/Efficiency exceeds 0.9 are drawn in the bottom right panel.

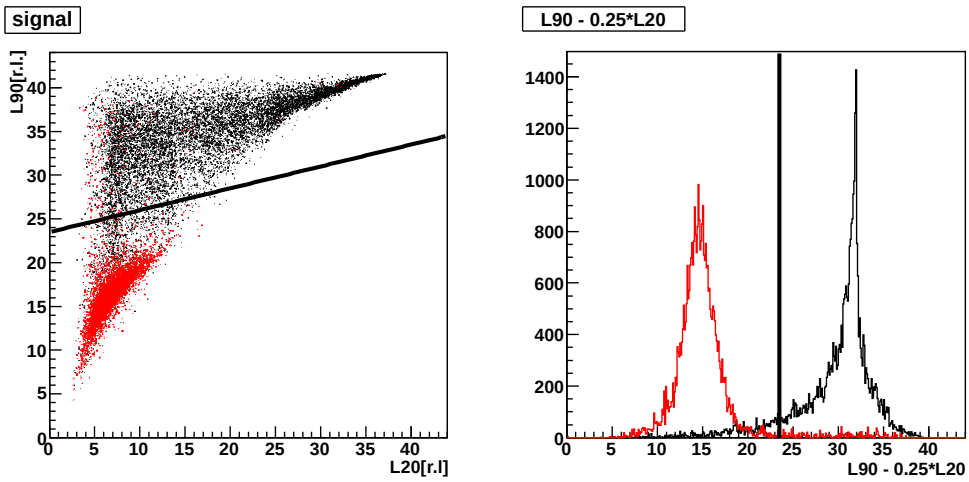

Figure 5.5: The left panel is scatter plot of $L_{20\%}$ and $L_{90\%}$. The right panel is L_{2D} distribution of photon and hadron particles.

On the other hand, +3.5% (Arm1) and -6.5% (Arm2) difference in the reconstructed energy of 350 GeV protons between the beam test results performed in CERN-SPS and the MC simulation was found [46], and included as a part of energy scale uncertainties.

Therefore, we assigned systematic errors of the energy scale as [+10.8%, -2.6%] for Arm1 and [+6.6%, -2.2%] for Arm2. Here we assumed uniform and Gaussian probability distributions for the energy scale errors estimated from the mass shift (+8.1% for Arm1 and 3.7% for Arm2), the known systematics (3.5%) and the SPS calibrations (3.5% for Arm1 and -6.5% for Arm2), respectively. After the standard deviations of two components were quadratically added, the systematic error bands were assigned with respect to the central value of the mass shift. In order to determine the systematic errors in the final energy spectra, we reconstructed two energy spectra by scaling the energy using the two extremes quoted above. The differences from the non-scaled spectrum to the two extreme spectra were assigned as systematic errors in each energy bin.

5.3.2 PID

The ratio of the photon component and the hadron component are different between the experimental data and the MC data. So we have to scale each normalization for photons and hadrons to fit the data distribution. The gray hatched area in the left panel of Figure 5.7 shows the weighted sum of the

scaled photon and hadron components of MC to reproduce the experimental data. In this estimation, the prepared library for the template fitting in the ROOT frame work based on [47] was used.

In order to avoid energy dependence, L_{2D} distributions were divided into 8 bins by reconstructed energy. Figure 5.6 shows the scatter plot of L_{2D} and reconstructed energy. Only events that have reconstructed energy more than 100GeV and hit within 2 mm from calorimeter edge are plotted.

Figure 5.7 shows L_{2D} parameters obtained by MC calculations of $\sqrt{s} = 7$ TeV *p*-*p* collisions with the QGSJET II-03 model, where the red and the blue histograms correspond to the photon and hadron events, respectively. The experimental data (black points) are also plotted. The gray histograms are the fitting results of the MC predictions for photons and hadrons obtained by two different methods.

Purity was evaluated after re-weighting with these value was applied. Note that the efficiency does not depend on scaling. The differences between the data and the weighted sum of the both components are not negligible. In order to estimate systematic uncertainties, we estimate the PID efficiency and the purity by two different methods, "Method A" and "Method B". In 'Method A', the L_{2D} of photon and hadron for MC are scaled independently to give the best match to the L_{2D} distribution of the experimental data. In "Method B" on the other hand, the MC templates were not only scaled but also horizontally shifted and smeared to match the data. The " Method B" is illustrated in the right panel in Figure 5.7. The PID correction for the data analysis was carried out base on the "Method B". The difference between "Method A" and "Method B" was assumed to give systematic uncertainty. The main reasons are the longitudinal shift caused from the uncertainty of interaction length and the fluctuation is different between the experiment and the MC simulation. The energy dependent PID systematic uncertainties were from 0.1% to 15%. They are listed in the Table 5.1 together with the efficiency and the purity. These numbers were estimated by using the five different MC samples (DPMJET 3.04, EPOS 1.99, PYTHIA 8.145, QGSJET II-03, and SYBILL 2.1) in order to increase statistics.

The L_{2D} distributions for the pseudo-rapidity regions corresponding to the small tower, the large tower A, and the large tower B are summarized in Figures 5.8, 5.9, and 5.10. In each figure, panels correspond to the energy ranges from 0-500 to more than 3500 GeV from left top to right bottom.

5.3.3 Multi-hit

In a *p*-*p* collision at the LHC, a lot of particles were generated at the interaction point, and only a few particles reached to the LHCf acceptance. When

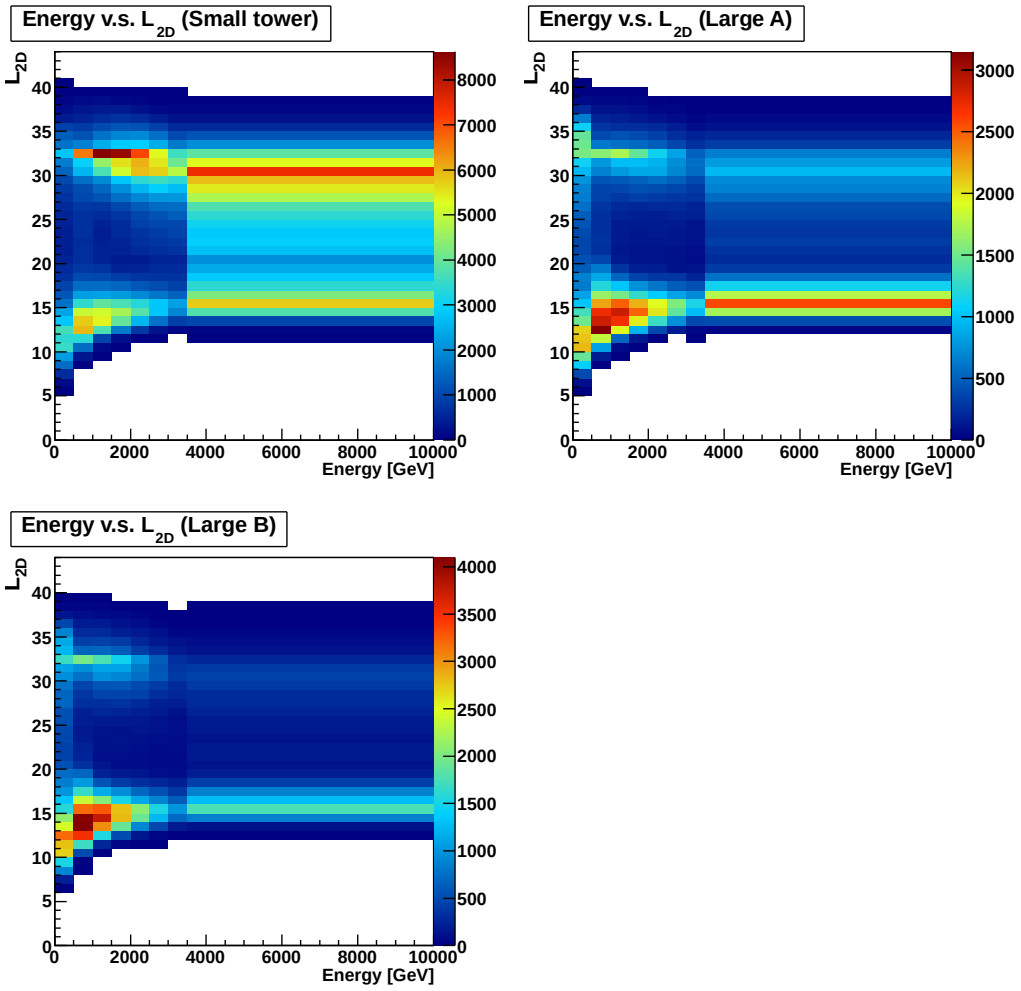

Figure 5.6: The scatter plot of the L_{2D} and the reconstructed energy of the data for the small tower, the large tower A, and the large tower B.

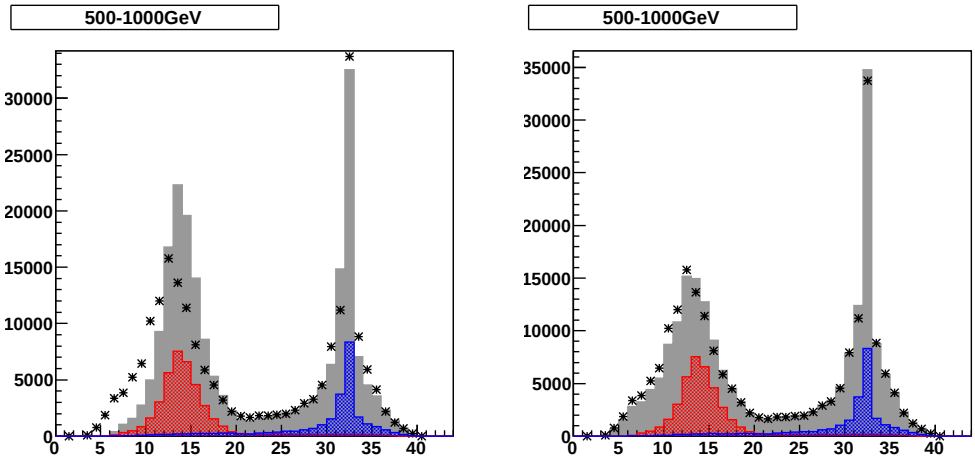

Figure 5.7: The L_{2D} distributions of the MC and the experimental data. Events with the reconstructed energy from 500 GeV to 1000 GeV were selected in these plots. The blue and red histograms in left and right figures correspond to the MC photons and hadrons, respectively. The black markers correspond to the experimental results. Gray histograms are fitting results of MC predictions for photons and hadrons obtained by two different methods.

LHCf Energy [GeV]	100 -500	500 -1000	1000 -1500	1500 -2000	2000 -2500	2500 -3000	3000 -3500	3500<
	Small Tower Method A							
Efficiency	0.881	0.919	0.954	0.964	0.978	0.979	0.978	0.945
Purity	0.830	0.910	0.972	0.980	0.958	0.959	0.960	0.970
P/E	0.942	0.990	1.019	1.017	0.979	0.980	0.981	1.027
	Small Tower Method B							
Efficiency	0.800	0.882	0.932	0.951	0.973	0.976	0.975	0.936
Purity	0.819	0.905	0.968	0.978	0.953	0.956	0.957	0.968
P/E	1.025	1.026	1.038	1.028	0.979	0.980	0.981	1.034
Ratio B/A	-8.1%	-3.4%	-1.8%	-1.1%	0.0%	0.0%	0.0%	-0.7%
	Large Tower Method A							
Efficiency	0.901	0.910	0.939	0.946	0.943	0.952	0.965	0.906
Purity	0.748	0.845	0.977	0.985	0.989	0.984	0.952	0.980
P/E	0.829	0.929	1.040	1.042	1.049	1.034	0.987	1.081
	Large Tower Method B							
Efficiency	0.741	0.802	0.893	0.927	0.936	0.946	0.959	0.895
Purity	0.714	0.830	0.974	0.986	0.989	0.984	0.946	0.979
P/E	0.964	1.034	1.091	1.063	1.057	1.040	0.987	1.093
Ratio B/A	-13.9%	-10.2%	-4.7%	-2.0%	-0.8%	-0.6%	0.1%	-1.2%
	Large Tower B Method A							
Efficiency	0.893	0.911	0.942	0.951	0.952	0.956	0.963	0.906
Purity	0.815	0.893	0.976	0.984	0.986	0.974	0.927	0.975
P/E	0.912	0.980	1.036	1.036	1.035	1.019	0.962	1.076
	Large Tower B Method B							
Efficiency	0.702	0.787	0.903	0.939	0.946	0.950	0.958	0.895
Purity	0.778	0.878	0.973	0.985	0.987	0.972	0.918	0.975
P/E	1.109	1.115	1.078	1.049	1.043	1.023	0.958	1.089
Ratio B/A	-17.8%	-12.1%	-3.9%	-1.3%	-0.7%	-0.5%	0.4%	-1.2%

Table 5.1: Systematic error from the PID process together with the PID efficiency and the purity. "P/E" means the ratio of the purity to the efficiency. Ratio B/A means the ratio of P/E for the method B to that for the method A.

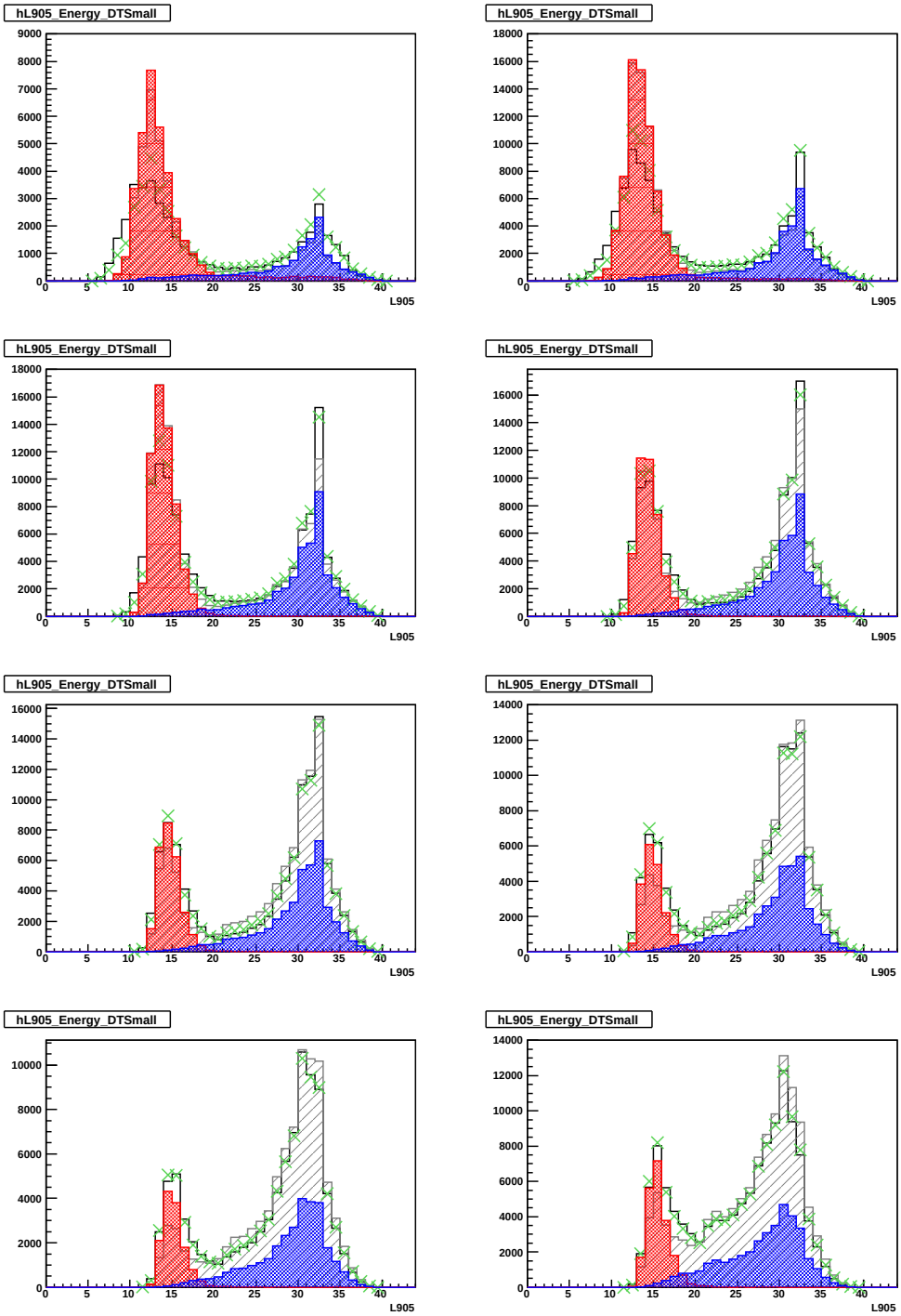

Figure 5.8: The L_{2D} distributions for the pseudo-rapidity region corresponding to the small tower.

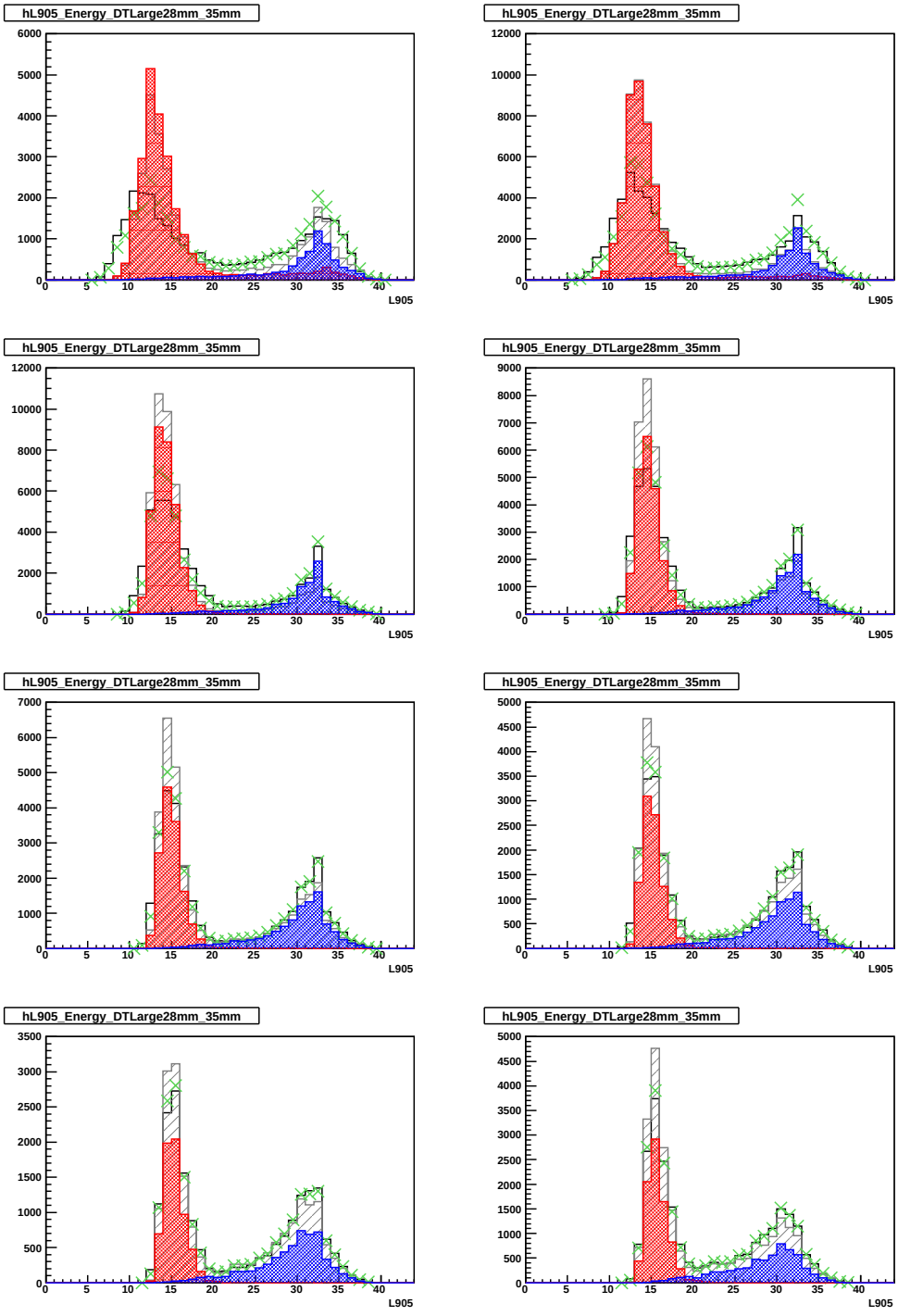

Figure 5.9: The L_{2D} distributions for the pseudo-rapidity region corresponding to the large tower A.

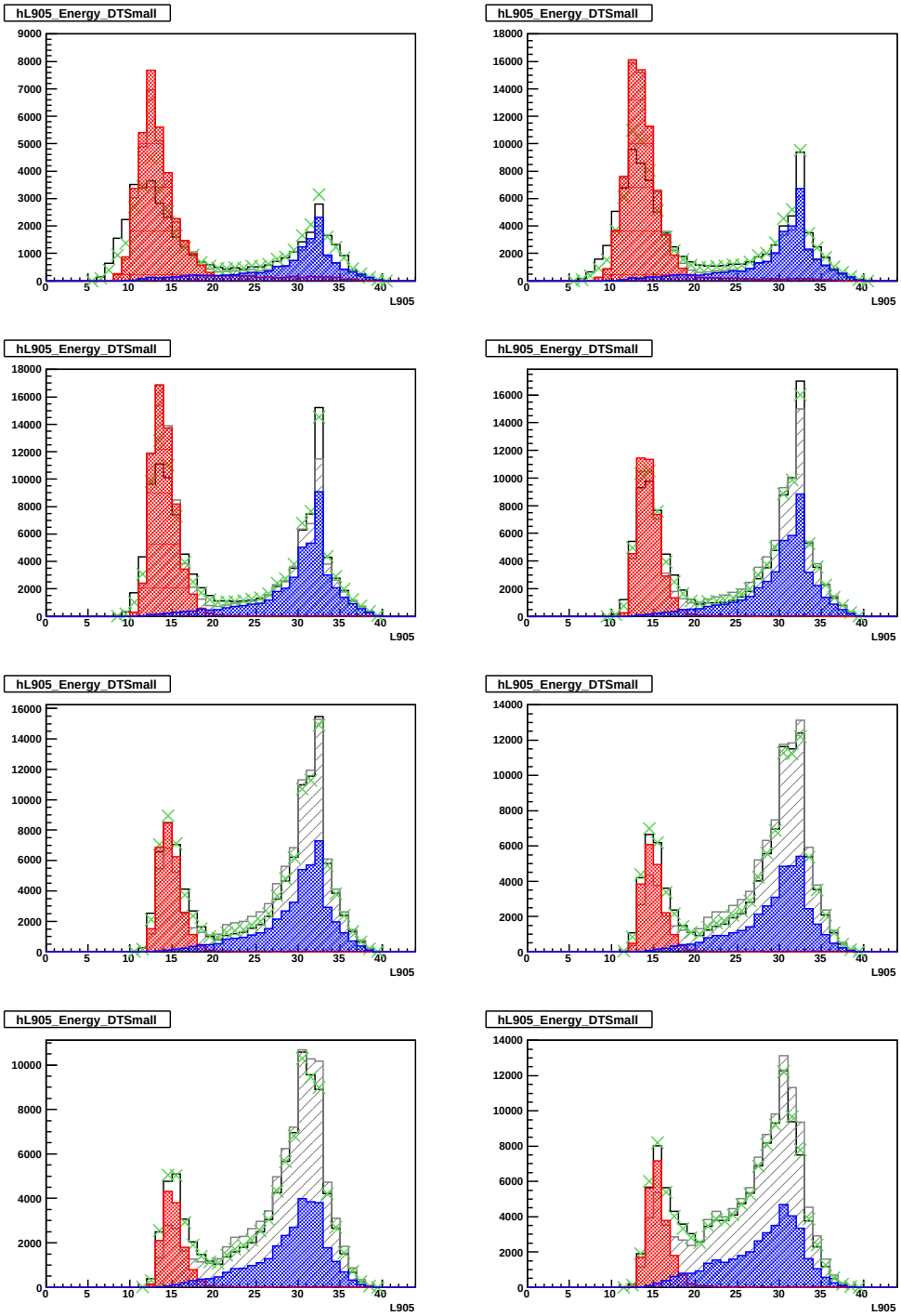

Figure 5.10: The L_{2D} distributions for the pseudo-rapidity region corresponding to the large tower A.

LHCf Energy [GeV]	Small tower	Large tower A	Large tower B
100 - 500	18.0%	9.5%	8.8%
500 - 1000	5.6%	5.1%	2.3%
1000 - 1500	1.8%	-0.4%	1.3%
1500 - 2000	0.1%	0.4%	-0.5%
2000 - 2500	0.1%	0.2%	-0.3%
2500 - 3000	0.3%	-0.9%	-4.7%
3000 - 3500	-0.1%	-2.5%	-2.4%
3500 - 4000	-2.5%	-4.3%	-1.5%
4000 - 5000	-2.2%	-4.0%	-6.5%
5000 <	-3.6%	-2.4%	- %

Table 5.2: Systematic error from the multi-hit events. Small, Large A and Large B correspond to the rapidity ranges of 10.76 to infinity, 8.99 to 9.22 and 8.81 to 8.99, respectively.

two or more particles hit the single LHCf calorimeter, these events were called the "multi-hit" event. Reconstruction of the multi-hit events and estimation of incident energy and incident position was much difficult compared with the single-hit event. We had to consider additional technique to reconstruct the multi-hit event correctly. Because the performance to discriminate single or multi hit event were not sufficient for the LHCf detector, a multi-hit events selection rather caused much larger systematic uncertainty. Therefore, all the events were regarded as single hit events, because the typical multiplicity at the LHCf acceptance was predicted to be small number by the MC simulations in case of the $\sqrt{s} = 7$ TeV p-p collision.

The systematic uncertainty from multi-hit contamination was estimated in as follows. If the multi-hit events were regarded as single hit events, they were recognized as one high energy events. For example, when two particles with the energy E1 and E2 hit the detector simultaneously, they seem a particle with the energy E1+E2. Thus, the systematic uncertainty from the multi-hit events was estimated by comparing the energy spectra with or without a multi-hit selection by using the MC simulation. Here, the multi-hit selection was defined as following. The reconstructed energy E_{rec} of two particles with the true energy E1 and E2 was distributed to both particles by the ratio of E1 to E2. The difference between the spectra with the multi-hit selection and without the multi-hit selection was considered as a part of systematic uncertainties. They are summarized in the Table 5.2.

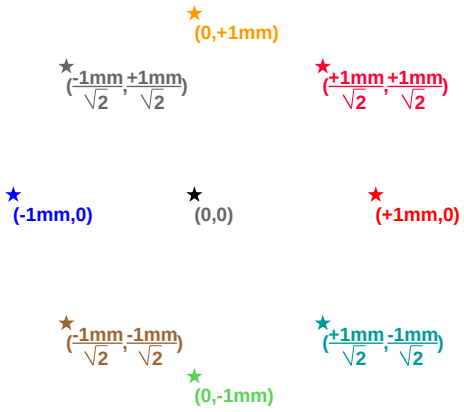

Figure 5.11: The 1 mm shifted beam center positions around the original center position. Each color correspond to the histogram in Figure 5.12

5.3.4 Beam related systematic errors

Here the systematic uncertainties caused by beam condition are discussed. The events containing more than one collision in a bunch crossing were called "pile-up events". Owing to the low luminosity at the operation for this data set, the provability of the pile-up events (P($n \geq 2$)) was calculated to be 7.2% by assuming the Poisson probability distribution. Considering the acceptance of LHCf for inelastic collisions, the fraction of pile-up events was less than 0.2% [36], and we concluded that pile-up does not affect this analysis.

The position of the zero degree collision Angle projected on the transverse plane of the LHCf detectors, called "beam-center" hereafter, could move from fill to fill, because beam transverse position and crossing angles at the IP slightly fluctuated. The beam center position was determined within 1 mm accuracy by two different methods of the distribution of particle hit position measured by the LHCf detectors and the Beam Position Monitors (BPMSW) installed 21 m away from the IP1 [48]. We checked the changes of the energy spectra by shifting the beam center position by 1 mm in the data spectra for the fiducial area cut. Figure 5.11 illustrated the original beam center and the 1 mm shifted positions. Figure 5.12 show the energy spectra (left) and ratios (right) to the original center for each center position as shown in Figure 5.11. Top panels correspond to the energy spectra and the ratio for the small tower, while middle and bottom panels correspond to the large tower A and

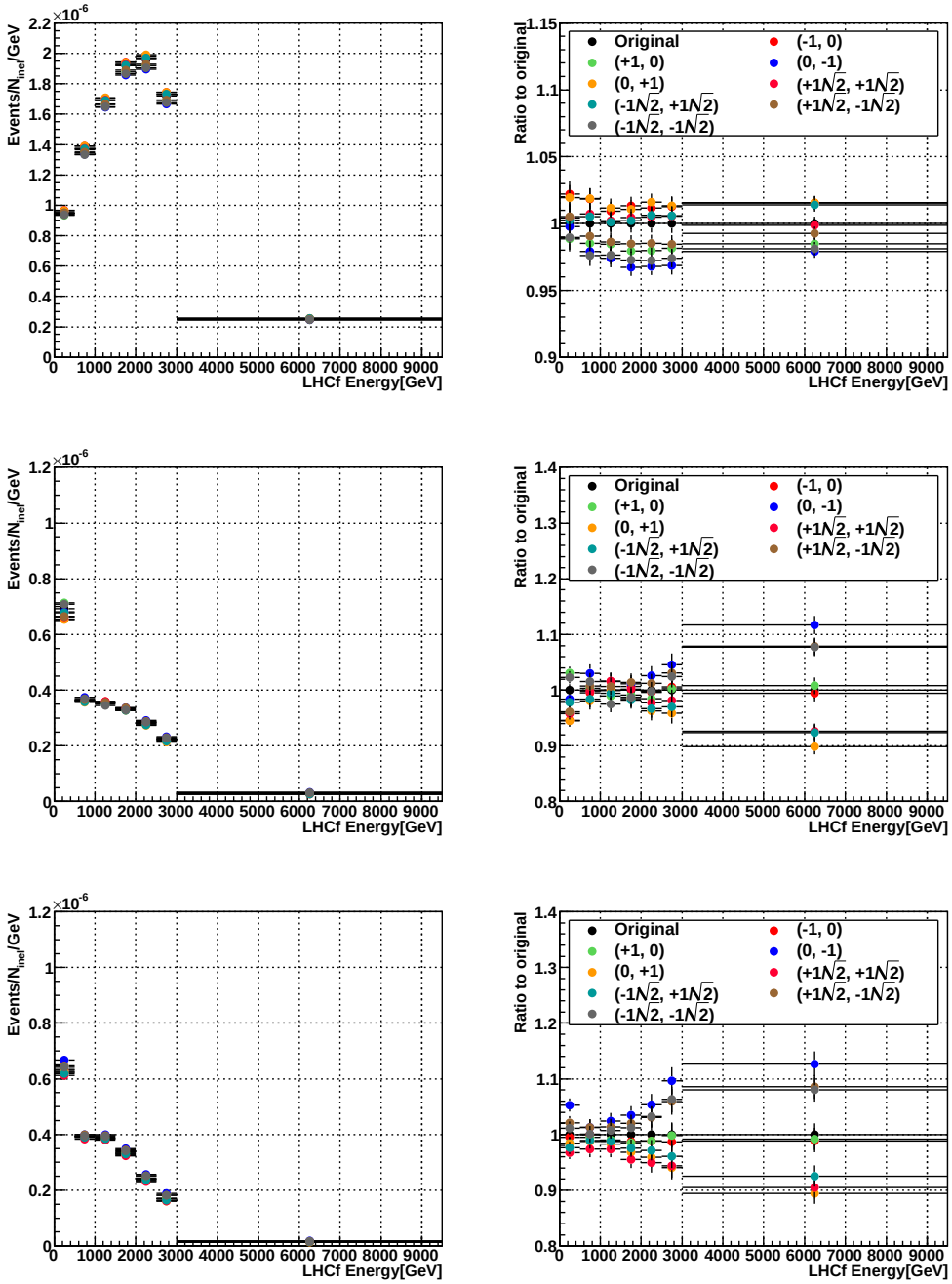

Figure 5.12: The energy spectra (left) for each beam center position and the ratios (right) to the original center. Top panels correspond to the energy spectra and the ratio for the small tower, while middle and bottom panels correspond to the large tower A and B, respectively. Each color represents the shifted center position in Figure 5.11

B, respectively. The largest difference in the ratios were considered as a part of systematic uncertainty in the final energy spectra.

5.3.5 Tail of position resolution

The resolution of transverse hit position of the LHCf detector for neutrons is about 0.1 mm to 1.3 mm depending on the neutron energy as discussed in Chapter 3.1.3. There were, however, some events reconstructed as hit to the position which shifted largely from the actual hit position. Therefore, particles hit in the outside of the fiducial area can contaminate to the energy spectra due to the tail of position resolution. Figure 6.1 shows the true incident position distribution at each fiducial area for the MC simulation with the EPOS 1.99 model. The upper, the middle and the bottom panels show the distribution of true incident position of the neutron events in the fiducial regions of the small tower, the large tower A, and the large tower B, respectively. Horizontal and vertical axes represent the transverse distance from the beam center position. Depending on the incident neutron energy, mis-reconstructed events affect to the energy and p_T spectra.

The effect of position resolution to the final energy spectra was estimated by using the MC simulations. The black and red histogram in Figure 5.14 correspond to the energy spectra in each fiducial region selected by using the SciFi measured hit positions (E_{posrec}) and the MC true position information ($E_{postrue}$) obtained by the EPOS 1.99 model. Figure 5.15 shows the ratio between the (E_{posrec}) and the ($E_{postrue}$) estimated by each hadronic interaction model. The vertical axis represent ration of (E_{posrec})/($E_{postrue}$). These error taken into accounts a part of systematic errors.

5.4 Analysis of the models

The MC predictions were generated with the models QGSJET II-03 [17], EPOS 1.99 [14], DPMJET 3.04 [13], PYTHIA 8.145 [15, 16], and SYBILL 2.1 [18] to compare with the experimental result. The model spectra were reconstructed with same method with the data analysis after the full MC simulation with the COSMOS 7.49 and EPICS 8.81 they are the tool kit of MC simulation. The MC simulations consist of following parts; 1) generation of a proton-proton collision with specific model, 2) the beam pipe transportation process from IP1 to TANs, and 3) the detector simulation process. The geometrical configurations, magnetic field of D1 dipole magnets, and particle decay were considered in 2) the transportation part. In 3) the detector simulation process, ununiformity of the calorimeters and the

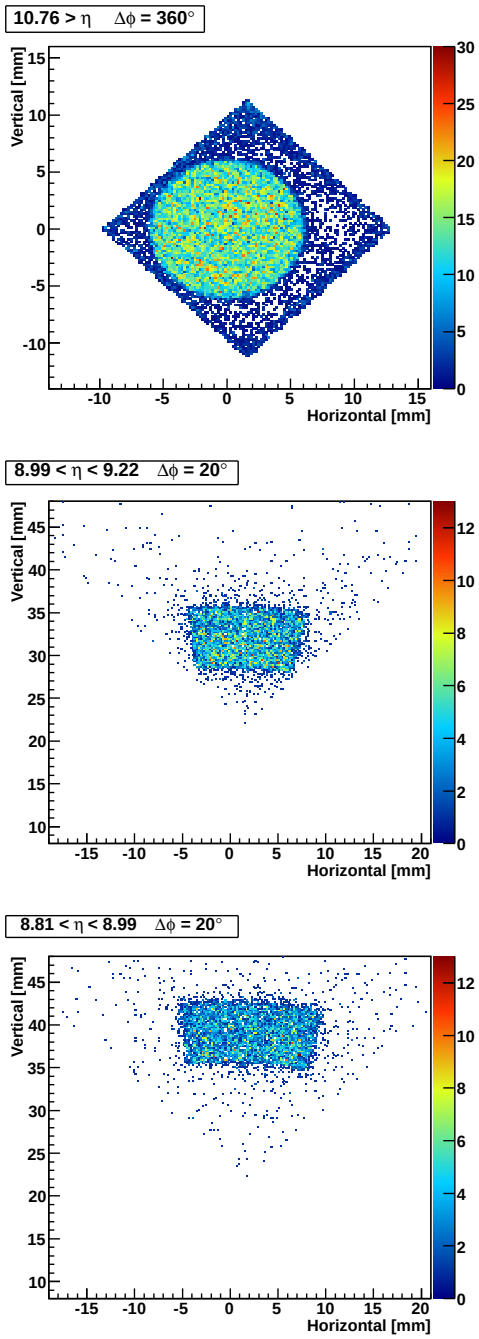

Figure 5.13: The true incident position distributions for the events in which hit position was reconstructed in each fiducial area obtained by using the EPOS 1.99 model. Horizontal and vertical axes represent the transverse distance from the beam center position.

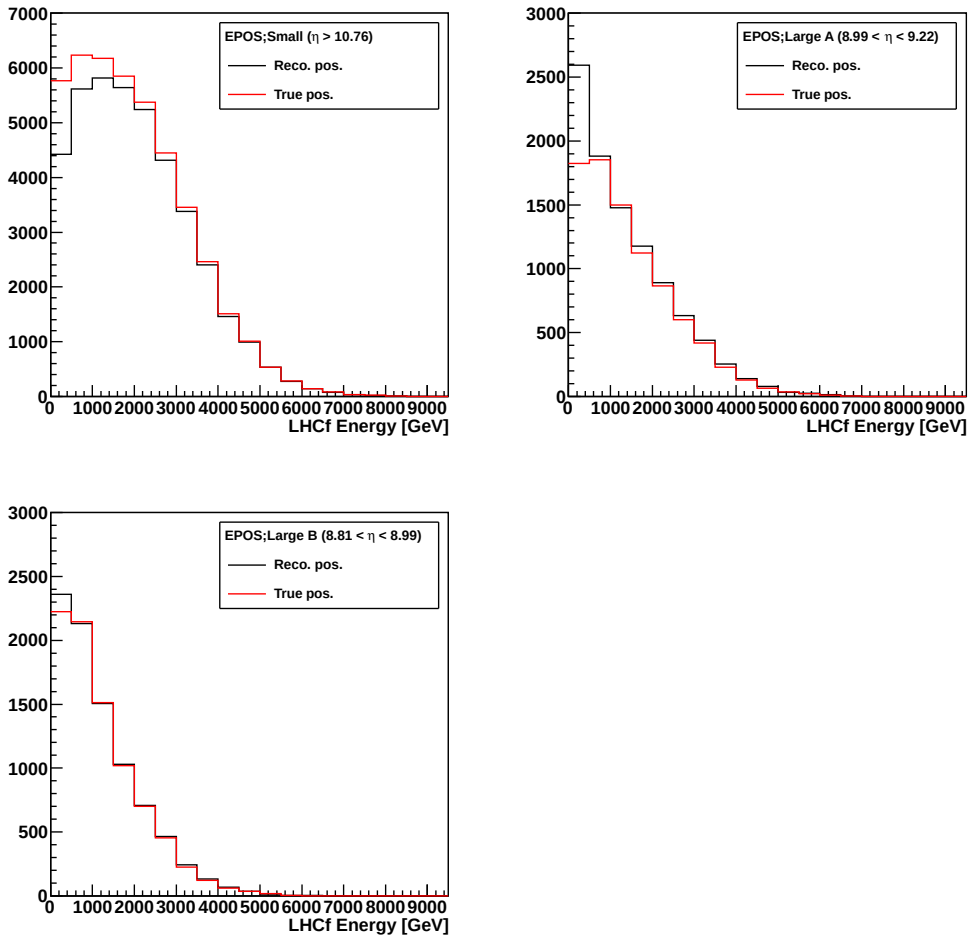

Figure 5.14: Energy spectra using measured hit position and true hit position. Black and red histogram show the energy spectra the neutron events in the fiducial area selected by measured hit position and true hit position, respectively.

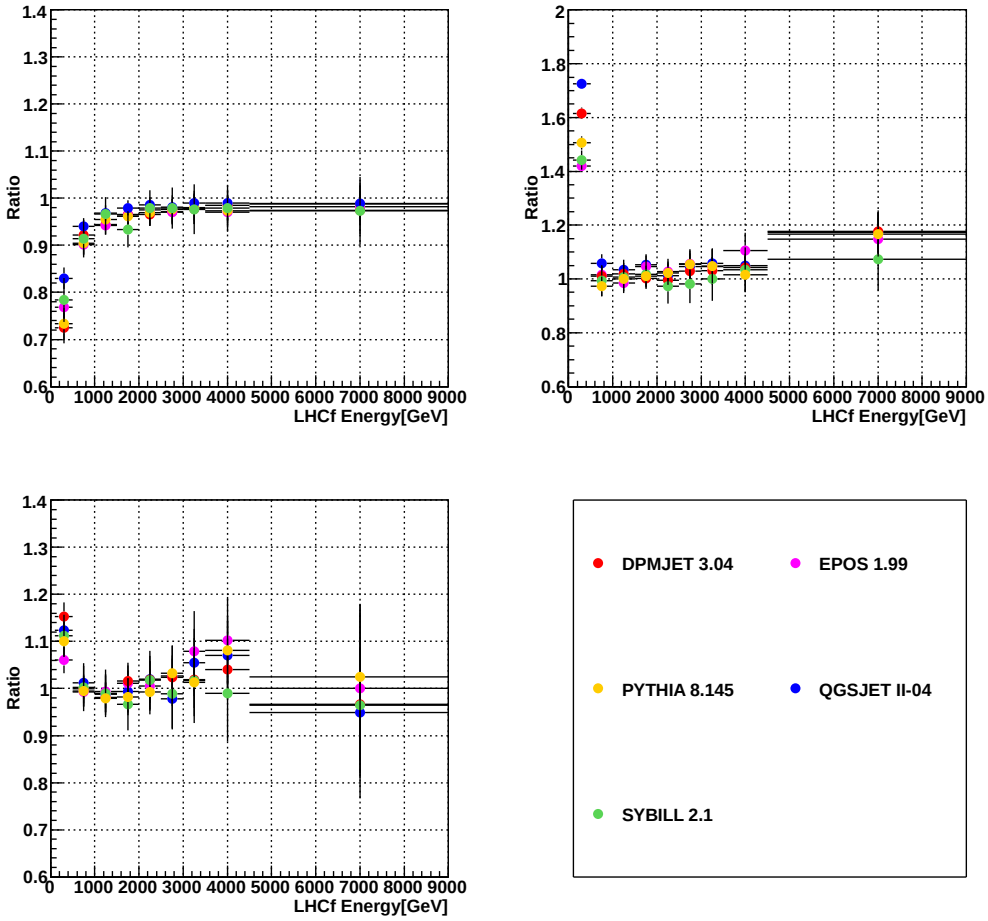

Figure 5.15: The ratio between the (E_{posrec}) and the ($E_{postrue}$) estimated by each hadronic interaction model. The upper left, the upper right, and the bottom panels correspond to the small tower, the large tower A, and large tower B, respectively.

LHCf Energy [GeV]	100 -500	500 - 1000	1000 - 1500	1500 - 2000	2000 - 2500	2500 - 3000	3000 - 3500	3500<
Small tower								
EPOS 1.99	-23.4%	-9.4%	-5.5%	-3.3%	-2.3%	-2.7%	-2.5%	-2.2%
QGSJET II-03	-17.2%	-5.9%	-2.8%	-1.9%	-1.5%	-1.6%	-0.8%	-1.1%
SYBILL 2.1	-21%	-8.8%	-3.7%	-5.1%	-2.7%	-1.1%	-1.5%	-2.4%
DPMJET 3.04	-27.2%	-8.3%	-5.1%	-3.6%	-2.4%	-2.6%	-2.2%	-0.4%
PYTHIA 8.145	-26.3%	-9.2%	-4.5%	-3.8%	-2.4%	-2.8%	-0.4%	-2.2%
Large Tower A ($8.99 < \eta < 9.22$)								
EPOS 1.99	36.0%	0.4%	0.6%	4.1%	3.9%	2.4%	5.9%	-0.5%
QGSJET II-03	63.1%	5.2%	6.2%	4.5%	0.2%	5.9%	2.0%	2.9%
SYBILL 2.1	34.4%	3.7%	1.4%	0.8%	-4.7%	2.0%	-9.1%	1.2%
DPMJET 3.04	51.0%	2.6%	1.9%	0.1%	1.4%	1.4%	-2.1%	2.2%
PYTHIA 8.145	40.7%	-1.9%	2.5%	0.7%	2.4%	3.8%	-2.1%	0.0%
Large tower B ($8.81 < \eta < 8.99$)								
EPOS 1.99	6.3%	-0.2%	-0.3%	1.7%	-1.2%	5.0%	7.5%	6.3%
QGSJET II-03	12.4%	1.3%	-0.7%	-1.5%	2.4%	-1.5%	8.7%	-0.3%
SYBILL 2.1	11.2%	0.6%	-0.6%	-3.3%	0.9%	-3.0%	2.3%	-1.8%
DPMJET 3.04	15.1%	0.8%	-1.3%	1.1%	2.7%	0.1%	2.4%	1.1%
PYTHIA 8.145	10.3%	0.5%	-2.9%	-0.5%	-2.4%	0.8%	6.0%	4.8%

Table 5.3: Systematic error from the position resolution.

pedestal fluctuation assumed in the experimental situation were taken into accounts and the QGSJET II-03 model was employed as a interaction model.

Figure 5.16 shows the initial energy spectra of neutral baryons for each model at the three different pseudo-rapidity regions at the LHCf detectors. Each model correspond to a color indicated in the figure, and vertical axes are the numbers of particles per 10^7 collisions per GeV. Very large discrepancy can be identified not only in shapes of spectra but also in absolute neutron yields among the models. However, the detector response must be considered due to the finite resolution and some inefficiencies.

Event reconstructions of the MC predictions were carried out with the same method as mentioned in Chapter 3.1. The generated MC samples were also used to estimate systematic uncertainties.

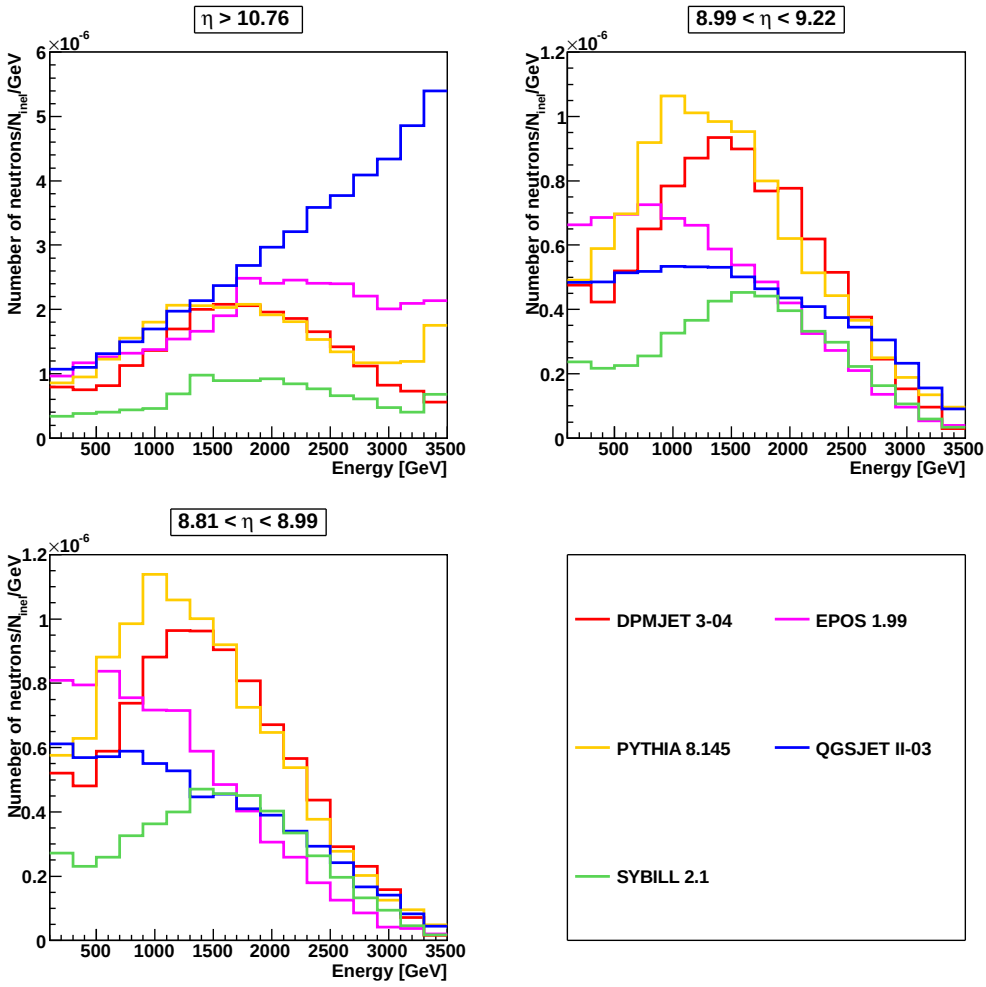

Figure 5.16: The initial energy spectra of neutrons. Each color represents the hadronic interaction model. Left panel correspond to the small tower spectra, and right correspond to the large tower spectra.

Chapter 6

Results of the $\sqrt{s} = 7$ TeV data analysis

The analysis of forward neutron events were carried out independently for Arm1 and Arm2 using the data taken by LHCf experiment at LHC $\sqrt{s} = 7$ TeV proton-proton collisions. The same analysis procedure were applied for the both Arm 1 and Arm2 data. The obtained spectra are compared with the model prediction spectra generated by MC simulation and discussed in Section6.2. The measured energy spectra were unfolded by using the two dimensional unfolding method discussed in Chapter 4.

6.1 Measured data

Here the measured observable before applying the analysis selections were summarized. The total number of triggered events was 2916495 in this data set without the offline selection nor the edge cuts. The numbers of the events selected by the offline event cut and the calorimeter edge cut in the data set are summarized in Table 6.1. The hadron-like events were discriminated from the photon-like events by the PID method discussed in Chapter 5.2.1.

Figure 6.1 shows the incident position distributions (hit-map) of the

	hadron-like	photon-like
Small tower	642749	364771
Large tower	336724	474775

Table 6.1: The numbers of the hadron-like events and the photon-like events at both the small and the large towers.

hadron-like events at the small tower (bottom) and large tower (right). The calorimeter edge cut were applied in this figures. The border in the hit-map of the large tower above 42 mm was caused from the projection of the beam pipe.

Figure 6.2 show the numbers of events as functions of the distance from the beam center position for photon-like (left) and hadron-like (right). The red hatched areas were excluded from the analysis, due to the nonuniform acceptance of the calorimeters.

Figure 6.3 shows the measured transverse momentum p_T and rapidity Y distribution for the hadron-like events.

6.2 Measured Energy spectra

To combine the results of Arm1 and Arm2, events hit in the common rapidity region as shown in Figure 5.1 were selected. Figure 6.4 shows the energy spectra of forward neutrons measured by the Arm1 and Arm2 detectors at the LHC $\sqrt{s} = 7$ TeV p-p collisions. The left, middle, and right panels correspond to the pseudo-rapidity range of $\eta > 10.76$, $9.22 > \eta > 8.99$, and $8.99 > \eta > 8.81$. Although quantitative comparison was not possible for this plot because of the different response of the both detectors, it was confirmed that the similar physical quantities was observed by the Arm1 and Arm2 detectors.

The measured spectra were also compared with the MC predictions. Figure 6.5 is the comparison of the energy spectra measured by the Arm1 detector and the MC model predictions. The colored lines indicate MC predictions by DPMJET 3.04 (red), EPOS 1.99 (magenta), PYTHIA 8.145 (yellow), QGSJET II-03 (blue) and SYBILL 2.1 (green). MC spectra were obtained by the full MC simulation and the reconstruction procedure same as the experimental data analysis except the PID process. The vertical axes were normalized to events per number of inelastic collision per GeV. No model matches with the experimental data perfectly. The QGSJET II-03 model predicted similar neutron energy spectra with the experiment at the small tower.

The systematic uncertainty caused by the energy scale uncertainty is not considered here, and is discussed in the next chapter.

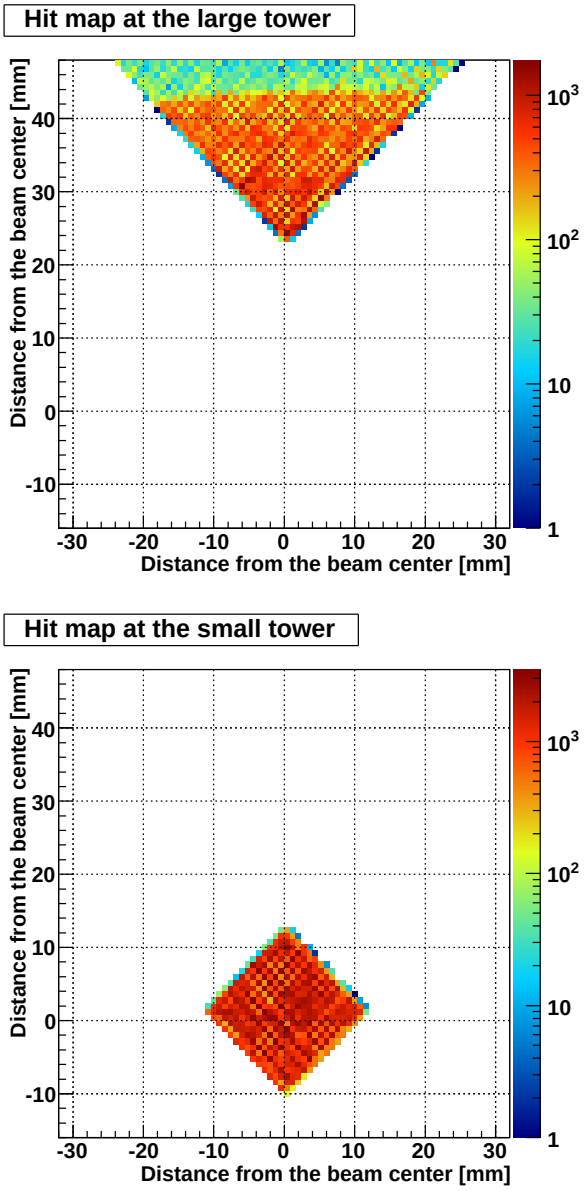

Figure 6.1: The incident position distributions (hit-map) of the hadron-like events at the small (bottom) and large (right) towers

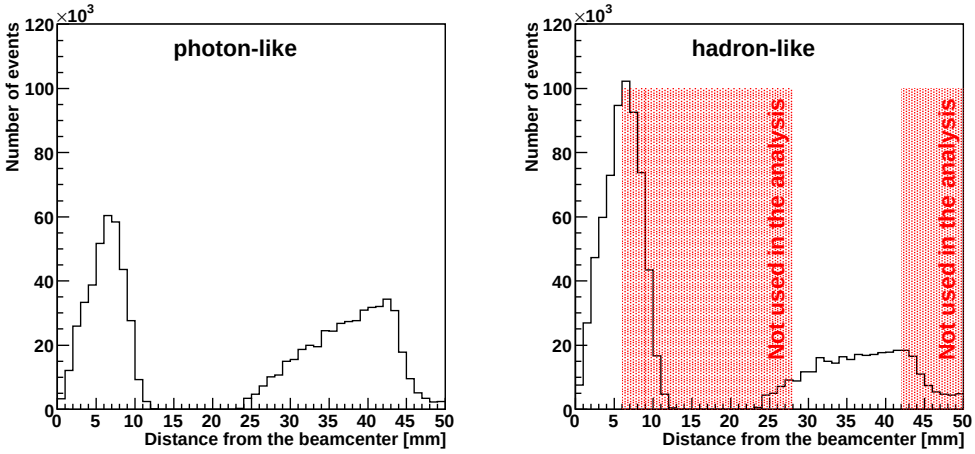

Figure 6.2: The numbers of events as functions of the distance from the beam center position for photon-like (left) and hadron-like (right). The red hatched areas were excluded from the analysis.

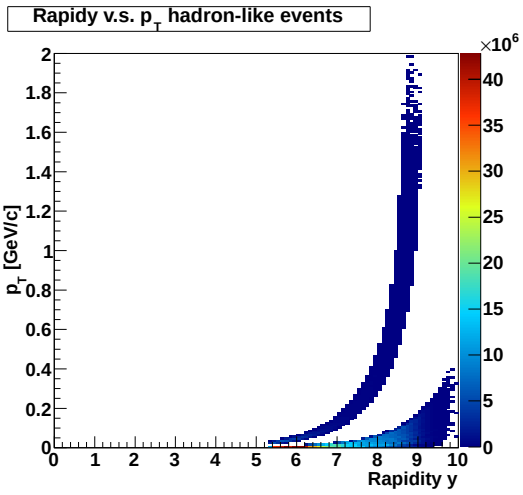

Figure 6.3: The measured transverse momentum p_T and rapidity Y distribution of the hadron-like event.

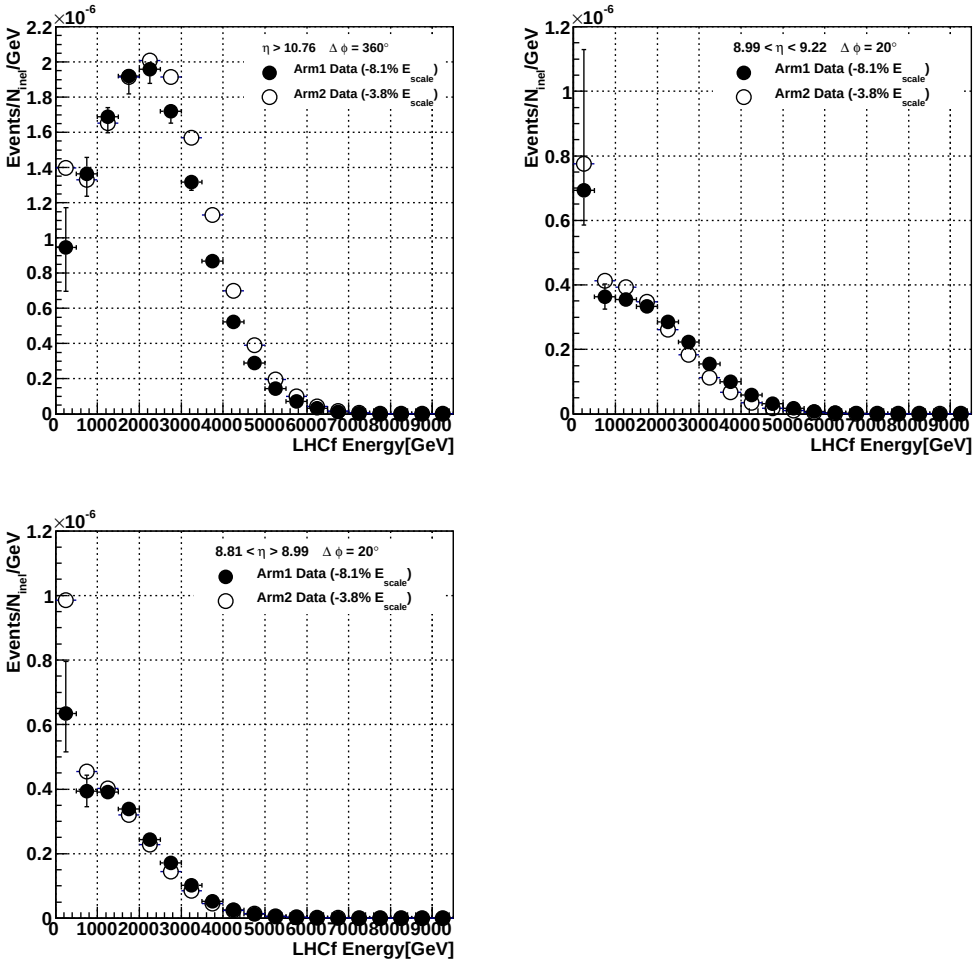

Figure 6.4: The measured energy spectra of the hadron-like events. The left, center, and right panels show the results for the small tower, the large tower A ,and the large tower B, respectively. The vertical bars represent the systematic uncertainties for Arm1.

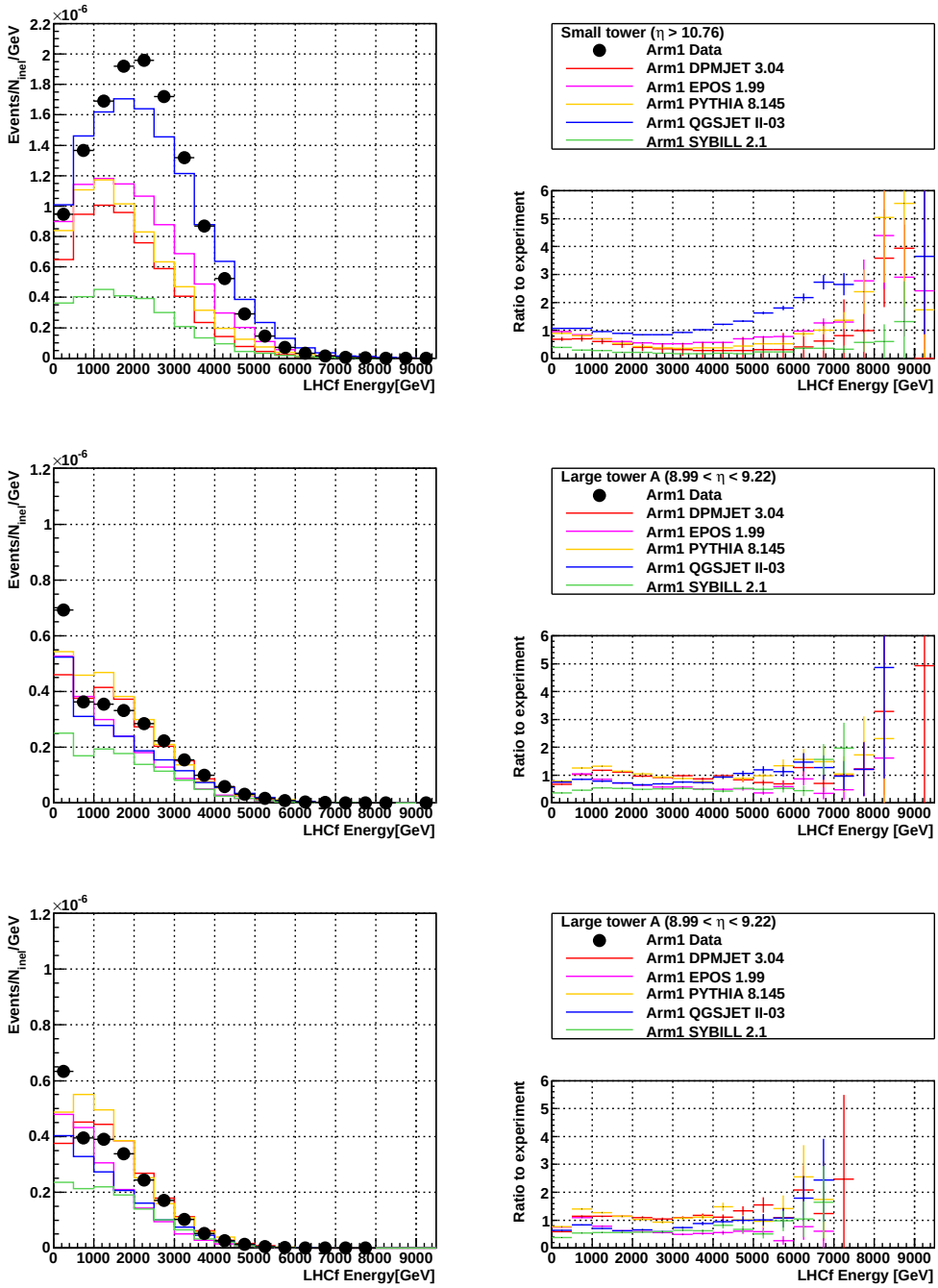

Figure 6.5: The measured Arm1 energy spectra of the hadron-like events together with the MC predictions. The left, center, and right panels show the results for the small tower, the large tower A, and the large tower B, respectively. The vertical bars represent the statistical uncertainties. Systematic uncertainty which indicated in Figure 6.4 is not included here.

N_n/N_γ	Small	Large A	Large B
Data	3.05±0.19	1.26±0.08	1.10±0.07
DPMJET 3.04	1.05	0.76	0.74
EPOS 1.99	1.80	0.69	0.63
PYTHIA 8.145	1.27	0.82	0.79
QGSJET II-03	2.34	0.65	0.56
SYBILL 2.1	0.88	0.57	0.53

Table 6.2: The hadron to photon ratio for the experiment and the MC models. The number of neutrons were divided by the number of photons. The rapidity intervals corresponding to the small, large A and large B were $\eta > 10.76$, $9.22 > \eta > 8.99$ and $8.99 > \eta > 8.81$, respectively.

6.3 Unfolded spectra

The measured spectra were unfolded by the method discussed in Chapter 4. The systematic effect in the unfolded spectra caused from the energy scale uncertainty was estimated by applying the unfolding method to the energy spectra obtained by five different energy scales. The lowest one (89.2%) corresponds to the lower band of the systematic uncertainty of the energy scale, and highest energy scale (102.7%) is vice versa. The energy scale of 91.9% is nominal energy scale considering the π^0 mass shift effect. The two intermediate energy scale (95.1% and 100%) were also employed, in order to understand the change of spectrum shapes.

Figure 6.6 shows the unfolded energy spectra with each energy scale for the small tower, the large tower A, and the large tower B. Each color represents different energy scale (see legend). The difference between the spectra calculated by the lowest energy scale and the highest energy scale were considered as the systematic uncertainties from the energy scale.

The neutron to photon ratio (N_n/N_γ) were summarized in Table 6.2. Here N_n and N_γ are the number of neutrons and photons, respectively. The PID efficiency and detection efficiency were taken into account for the estimation of number of neutrons. The Experimental results show the highest neutron ratio against the hadronic interaction models at all rapidity regions.

Figure 6.7 shows the unfolded energy spectra for the hadron-like events at the Arm1 small tower, large tower A, and large tower B, respectively. In each area, the detection efficiency of neutron events and the PID efficiency and purity were taken into account. Each colored histogram shows the model predictions.

The differential neutron production cross sections $d\sigma_n/dE$ were calculated

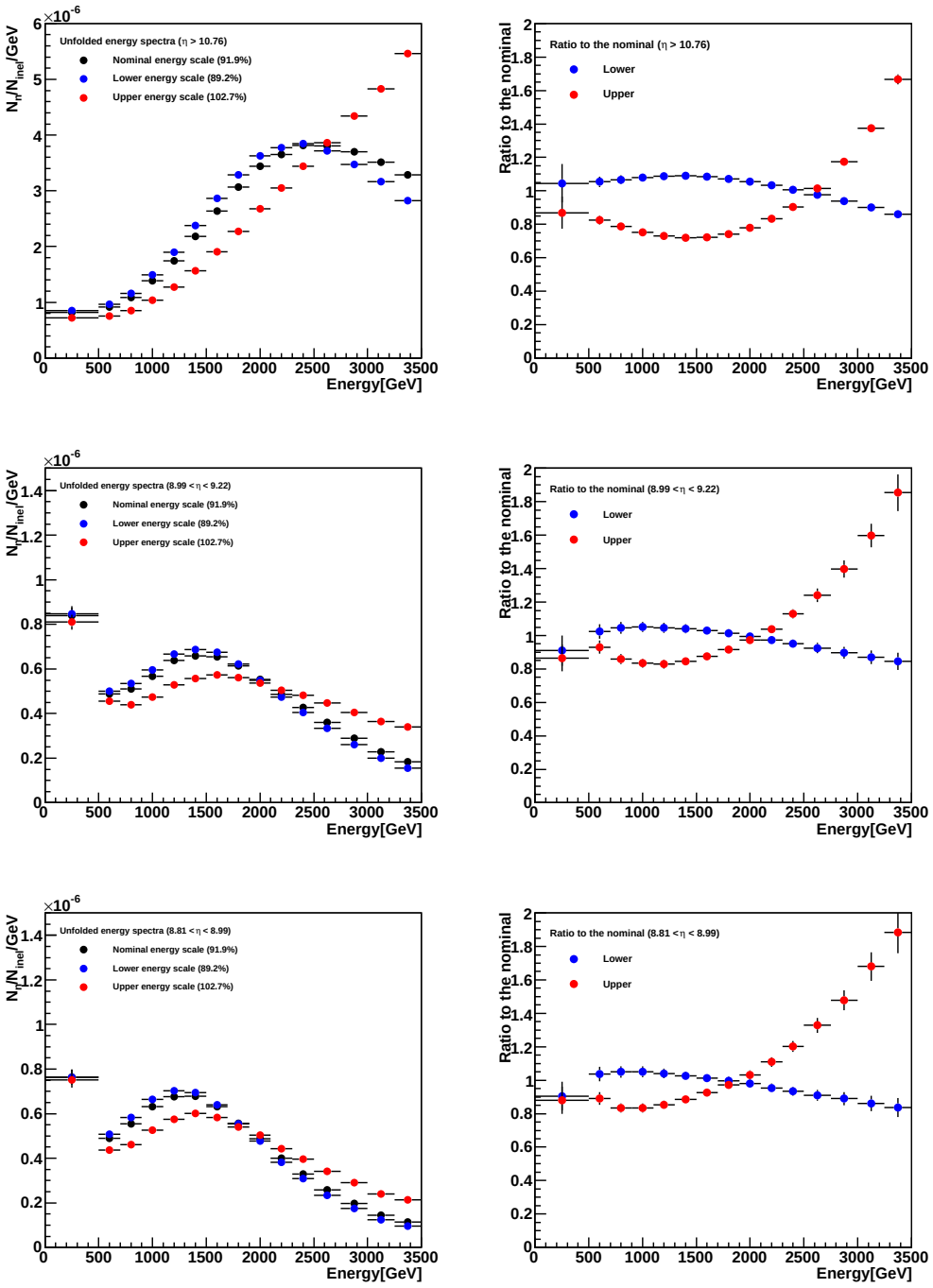

Figure 6.6: The unfolded energy spectra with each energy scale and the ratio to the nominal energy scale for the small tower, large tower A and large tower B from top to bottom.

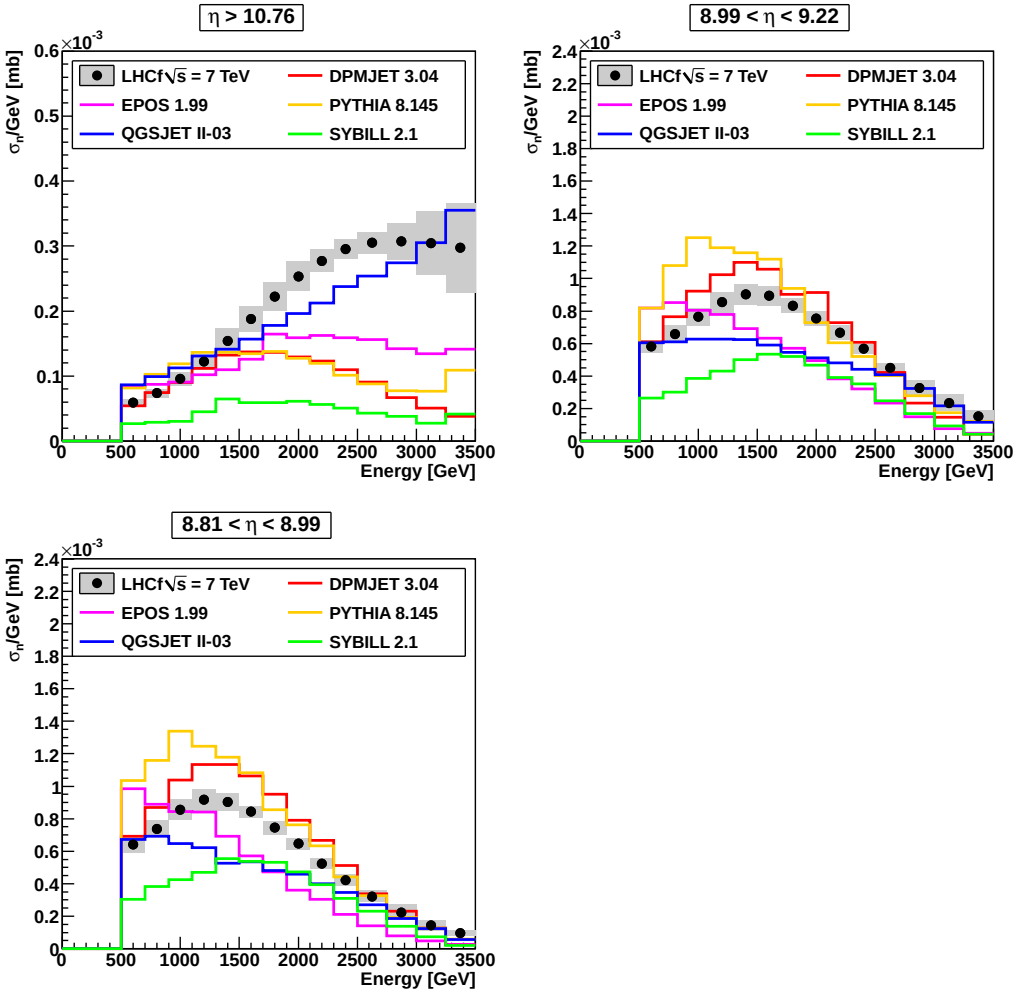

Figure 6.7: Unfolded energy spectra of the small tower ($\eta > 10.76$) and the large tower ($8.99 < \eta < 9.22$ and $8.81 < \eta < 8.99$). The hatched areas show systematic errors.

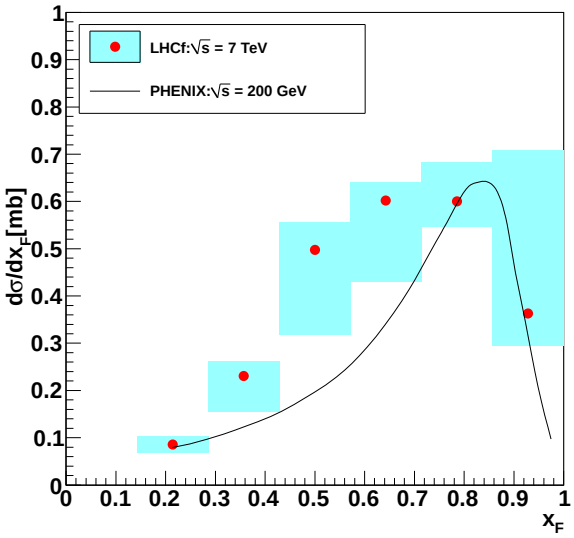

Figure 6.8: x_F distribution of neutrons at p_T range $0 < p_T < 0.11 x_F GeV/c$ at LHCf and ISR (PHENIX) [25]. The systematic uncertainties of the LHCf are shown as hatched area.

form the unfolded experimental spectra and given as below,

$$d\sigma_n/dE = \frac{dN(\Delta\eta\Delta E)}{dE}\frac{1}{L} \times \frac{2\pi}{d\phi}\,[\mathrm{mb}], \tag{6.1}$$

where $dN(\Delta\eta\Delta E)$ means the number of neutrons observed in the each rapidity range and each energy binning, L is the integrated luminosity corresponding to the data set. The last term is correction of the azimuthal interval. The cross sections are summarized in Table 6.3. Experiment shows most hard spectra than each model, the QGSJET II-03 model predicted similar neutron production rate compared with the experiment at the small tower. On the other hand, PYTHIA 8.145 predicted the neutron production rate similar to the experimental results at the large towers.

The experimental results were also compared with the ISR and PHENIX results [25]. Figure 6.8 shows the x_F distributions at p_T range $0 < p_T < 0.11 x_F$GeV/c for the LHCf and PHENIX results. The shape of the LHCf measurement was strongly depend on the energy scale correction. The systematic uncertainty was indicated as hatched area. The uncertainty of absolute normalization of 6.1% for the LHCf result and 9.7% for the PHENIX measurement were not included. The LHCf results show similar results with the previous experiments considering the change of spectra by the choice of energy scale within the systematic uncertainty.

Small tower ($\eta > 10.76$)

Energy [GeV]	Data	DPMJET 3.04	EPOS 1.99	PYTHIA 8.145	QGSJET II-03	SYBILL 2.1
500-700	$5.91\times10^{-5}\pm5.20\times10^{-6}$	5.40×10^{-5}	8.34×10^{-5}	8.13×10^{-5}	8.66×10^{-5}	2.65×10^{-5}
700-900	$7.39\times10^{-5}\pm6.52\times10^{-6}$	7.45×10^{-5}	8.73×10^{-5}	1.03×10^{-4}	9.89×10^{-5}	2.89×10^{-5}
900-1100	$9.58\times10^{-5}\pm1.00\times10^{-5}$	9.00×10^{-5}	9.10×10^{-5}	1.19×10^{-4}	1.12×10^{-4}	3.03×10^{-5}
1100-1300	$1.22\times10^{-4}\pm1.23\times10^{-5}$	1.12×10^{-4}	1.02×10^{-4}	1.37×10^{-4}	1.30×10^{-4}	4.53×10^{-5}
1300-1500	$1.54\times10^{-4}\pm1.89\times10^{-5}$	1.32×10^{-4}	1.10×10^{-4}	1.36×10^{-4}	1.41×10^{-4}	6.46×10^{-5}
1500-1700	$1.88\times10^{-4}\pm1.97\times10^{-5}$	1.37×10^{-4}	1.26×10^{-4}	1.35×10^{-4}	1.57×10^{-4}	5.92×10^{-5}
1700-1900	$2.22\times10^{-4}\pm2.16\times10^{-5}$	1.36×10^{-4}	1.65×10^{-4}	1.38×10^{-4}	1.78×10^{-4}	5.90×10^{-5}
1900-2100	$2.53\times10^{-4}\pm2.28\times10^{-5}$	1.29×10^{-4}	1.59×10^{-4}	1.27×10^{-4}	1.96×10^{-4}	6.12×10^{-5}
2100-2300	$2.77\times10^{-4}\pm1.74\times10^{-5}$	1.23×10^{-4}	1.62×10^{-4}	1.20×10^{-4}	2.12×10^{-4}	5.60×10^{-5}
2300-2500	$2.95\times10^{-4}\pm1.52\times10^{-5}$	1.10×10^{-4}	1.59×10^{-4}	1.01×10^{-4}	2.37×10^{-4}	5.08×10^{-5}
2500-2750	$3.05\times10^{-4}\pm1.68\times10^{-5}$	9.04×10^{-5}	1.56×10^{-4}	8.80×10^{-5}	2.54×10^{-4}	4.28×10^{-5}
2750-3000	$3.07\times10^{-4}\pm2.76\times10^{-5}$	6.71×10^{-5}	1.42×10^{-4}	7.73×10^{-5}	2.75×10^{-4}	3.77×10^{-5}
3000-3250	$3.04\times10^{-4}\pm4.91\times10^{-5}$	5.07×10^{-5}	1.35×10^{-4}	7.66×10^{-5}	3.05×10^{-4}	2.75×10^{-5}
3250-3500	$2.98\times10^{-4}\pm6.90\times10^{-5}$	3.83×10^{-5}	1.41×10^{-4}	1.09×10^{-4}	3.55×10^{-4}	4.14×10^{-5}

Large tower A ($8.99 < \eta < 9.22$)

Energy [GeV]	Data	DPMJET 3.04	EPOS 1.99	PYTHIA 8.145	QGSJET II-03	SYBILL 2.1
500-700	$5.83\times10^{-4}\pm3.93\times10^{-5}$	6.10×10^{-4}	8.19×10^{-4}	8.19×10^{-4}	6.05×10^{-4}	2.65×10^{-4}
700-900	$6.59\times10^{-4}\pm5.45\times10^{-5}$	7.66×10^{-4}	8.53×10^{-4}	1.08×10^{-3}	6.10×10^{-4}	3.01×10^{-4}
900-1100	$7.65\times10^{-4}\pm5.36\times10^{-5}$	9.22×10^{-4}	8.03×10^{-4}	1.25×10^{-3}	6.28×10^{-4}	3.84×10^{-4}
1100-1300	$8.55\times10^{-4}\pm6.09\times10^{-5}$	1.02×10^{-3}	7.78×10^{-4}	1.19×10^{-3}	6.27×10^{-4}	4.31×10^{-4}
1300-1500	$9.04\times10^{-4}\pm6.19\times10^{-5}$	1.10×10^{-3}	6.92×10^{-4}	1.16×10^{-3}	6.25×10^{-4}	5.01×10^{-4}
1500-1700	$8.93\times10^{-4}\pm6.03\times10^{-5}$	1.06×10^{-3}	6.33×10^{-4}	1.12×10^{-3}	5.90×10^{-4}	5.33×10^{-4}
1700-1900	$8.31\times10^{-4}\pm4.33\times10^{-5}$	9.04×10^{-4}	5.72×10^{-4}	9.41×10^{-4}	5.46×10^{-4}	5.20×10^{-4}
1900-2100	$7.53\times10^{-4}\pm4.37\times10^{-5}$	9.15×10^{-4}	4.94×10^{-4}	7.30×10^{-4}	5.13×10^{-4}	4.66×10^{-4}
2100-2300	$6.65\times10^{-4}\pm4.25\times10^{-5}$	7.28×10^{-4}	3.83×10^{-4}	6.05×10^{-4}	4.80×10^{-4}	3.92×10^{-4}
2300-2500	$5.68\times10^{-4}\pm2.75\times10^{-5}$	6.07×10^{-4}	3.21×10^{-4}	5.22×10^{-4}	4.41×10^{-4}	3.51×10^{-4}
2500-2750	$4.51\times10^{-4}\pm2.58\times10^{-5}$	4.22×10^{-4}	2.33×10^{-4}	4.02×10^{-4}	4.07×10^{-4}	2.47×10^{-4}
2750-3000	$3.27\times10^{-4}\pm4.93\times10^{-5}$	2.34×10^{-4}	1.48×10^{-4}	2.78×10^{-4}	3.22×10^{-4}	1.69×10^{-4}
3000-3250	$2.35\times10^{-4}\pm5.17\times10^{-5}$	1.46×10^{-4}	7.64×10^{-5}	1.74×10^{-4}	2.18×10^{-4}	9.22×10^{-5}
3250-3500	$1.53\times10^{-4}\pm3.43\times10^{-5}$	4.35×10^{-5}	4.69×10^{-5}	1.20×10^{-4}	1.17×10^{-4}	4.27×10^{-5}

Large tower B ($8.81 < \eta < 8.99$)

Energy [GeV]	Data	DPMJET 3.04	EPOS 1.99	PYTHIA 8.145	QGSJET II-03	SYBILL 2.1
500-700	$6.40\times10^{-4}\pm5.28\times10^{-5}$	6.93×10^{-4}	9.86×10^{-4}	1.04×10^{-3}	6.72×10^{-4}	3.05×10^{-4}
700-900	$7.37\times10^{-4}\pm5.14\times10^{-5}$	8.68×10^{-4}	8.88×10^{-4}	1.16×10^{-3}	6.93×10^{-4}	3.84×10^{-4}
900-1100	$8.54\times10^{-4}\pm6.34\times10^{-5}$	1.04×10^{-3}	8.43×10^{-4}	1.34×10^{-3}	6.48×10^{-4}	4.26×10^{-4}
1100-1300	$9.17\times10^{-4}\pm6.78\times10^{-5}$	1.13×10^{-3}	8.41×10^{-4}	1.25×10^{-3}	6.21×10^{-4}	4.71×10^{-4}
1300-1500	$9.04\times10^{-4}\pm5.61\times10^{-5}$	1.13×10^{-3}	6.93×10^{-4}	1.18×10^{-3}	5.26×10^{-4}	5.54×10^{-4}
1500-1700	$8.45\times10^{-4}\pm3.69\times10^{-5}$	1.06×10^{-3}	5.71×10^{-4}	1.08×10^{-3}	5.35×10^{-4}	5.38×10^{-4}
1700-1900	$7.45\times10^{-4}\pm4.17\times10^{-5}$	9.50×10^{-4}	4.73×10^{-4}	8.54×10^{-4}	4.82×10^{-4}	5.31×10^{-4}
1900-2100	$6.47\times10^{-4}\pm3.64\times10^{-5}$	7.90×10^{-4}	3.60×10^{-4}	7.61×10^{-4}	4.59×10^{-4}	4.73×10^{-4}
2100-2300	$5.23\times10^{-4}\pm3.25\times10^{-5}$	6.66×10^{-4}	3.05×10^{-4}	6.33×10^{-4}	4.01×10^{-4}	3.94×10^{-4}
2300-2500	$4.23\times10^{-4}\pm3.44\times10^{-5}$	5.13×10^{-4}	2.11×10^{-4}	4.43×10^{-4}	3.45×10^{-4}	3.11×10^{-4}
2500-2750	$3.22\times10^{-4}\pm3.39\times10^{-5}$	3.39×10^{-4}	1.41×10^{-4}	3.26×10^{-4}	2.71×10^{-4}	2.31×10^{-4}
2750-3000	$2.23\times10^{-4}\pm4.90\times10^{-5}$	2.32×10^{-4}	7.79×10^{-5}	1.92×10^{-4}	1.86×10^{-4}	1.37×10^{-4}
3000-3250	$1.45\times10^{-4}\pm3.21\times10^{-5}$	1.28×10^{-4}	4.90×10^{-5}	1.28×10^{-4}	1.25×10^{-4}	7.23×10^{-5}
3250-3500	$9.66\times10^{-5}\pm1.66\times10^{-5}$	2.64×10^{-5}	2.52×10^{-5}	6.02×10^{-5}	5.69×10^{-5}	1.90×10^{-5}

Table 6.3: Differential neutron production rate σ_n/GeV [mb] for each rapidity range.

6.3.1 p_T distribution

The p_T distribution of forward neutron is also important observables to verify the hadron interaction models. The p_T spectra were obtained by using the multi dimensional unfolding method described in Chapter 4. Figure 6.9 shows the unfolded p_T spectra for the pseudo-rapidity regions corresponding to the small tower, the large tower A and the large tower B. The left hand panels shows the dependence on the energy scale. The lower band corresponds to 89.2% and upper band corresponds to 102.7%, respectively. The nominal 91.9% is the energy scale considering the π^0 mass shift effect (Details are described in Chapter 5.3). The right hand panels show the comparison with the model predictions. The hatched areas show energy scale uncertainty, while the other systematic effects does not included. The vertical axes were the number of neutrons per number of inelastic collisions per GeV/c.

The QGSJET II-03 model which predicts similar energy spectra with the experimental results at the small tower region, shows, however, quite different distribution with respect to the p_T spectra. The EPOS 1.99 model predicts similar distribution shape with the data, while the absolute neutron production rate is quite different.

Figure 6.10 shows the unfolded p_T spectra for the pseudo-rapidity regions for more than 500 GeV events.

6.4 Discussion; impact on air shower

Here we discuss about the impact of the LHCf neutron results for cosmic-ray showers. We reported the very hard neutron energy spectra compared with the hadronic interaction models at $\eta > 10.76$ corresponding to small tower. Neutron production cross sections in the large tower regions were also larger than the model predictions, but the differences were much smaller than that of the small tower rapidity. The sum of the neutron cross-section which summarized in Table 6.3 at the three rapidity regions as shown in Figure 5.1 were 6.2 mb for the experimental data and 5.0 mb for the DPMJET 3.04. About 20% more neutrons were generated than the prediction by the DPMJET 3.04 model in this rapidity regions. While the difference in the rapidity range corresponding to large tower is about 15% (Data; 5.5 mb, DPMJET 3.04; 4.76 mb). Therefore we assumed the inelasticity k can be varied up to +15% or +20% from the original value assumed in the DPMJET 3.04 model. The impact by the change of inelasticity to the development of cosmic-ray showers was studied.

To simplify the discussions, a one dimensional toy MC simulation for air

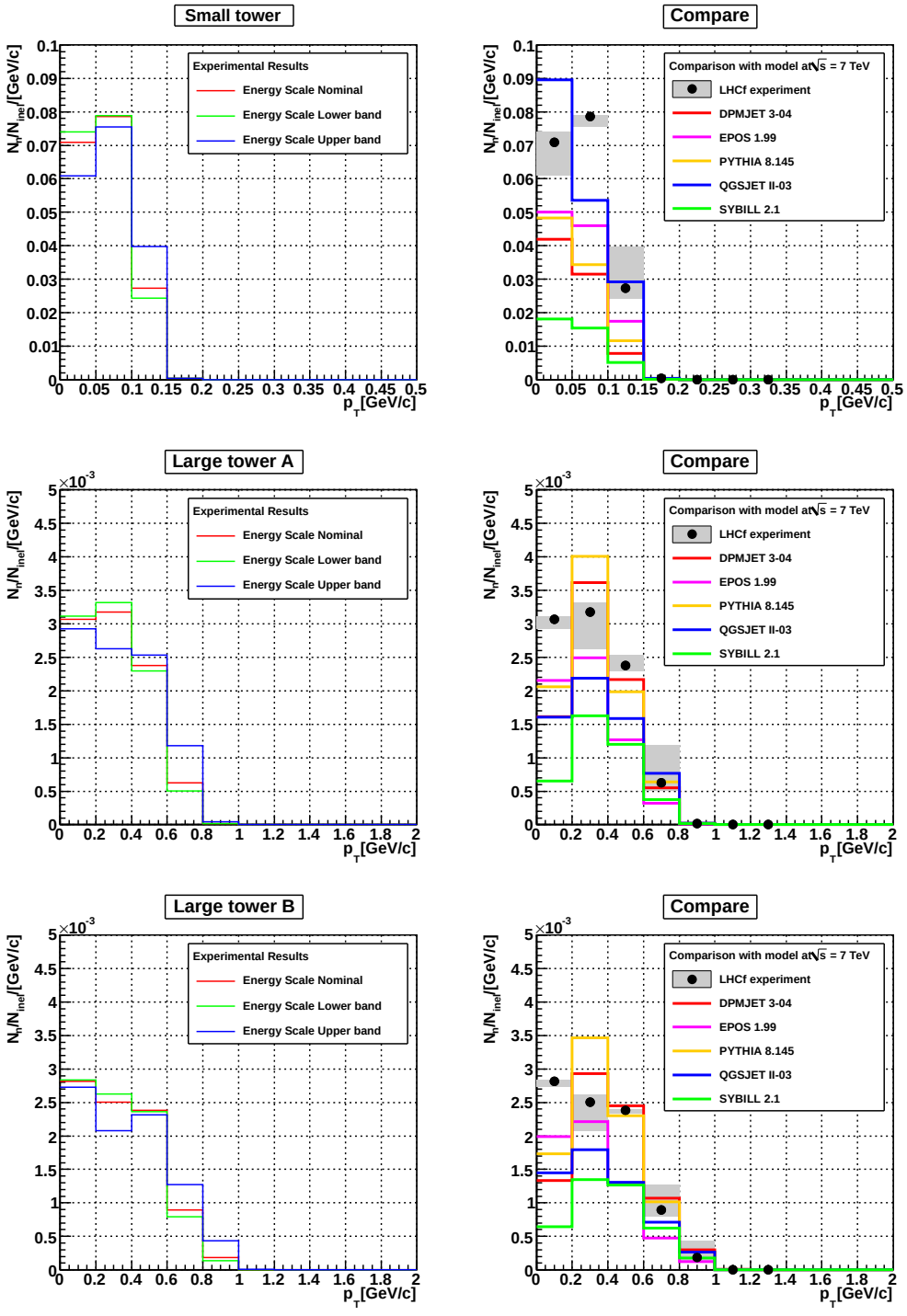

Figure 6.9: The p_T spectra for the pseudo-rapidity regions corresponding to the small tower, the large tower A and the large tower B.

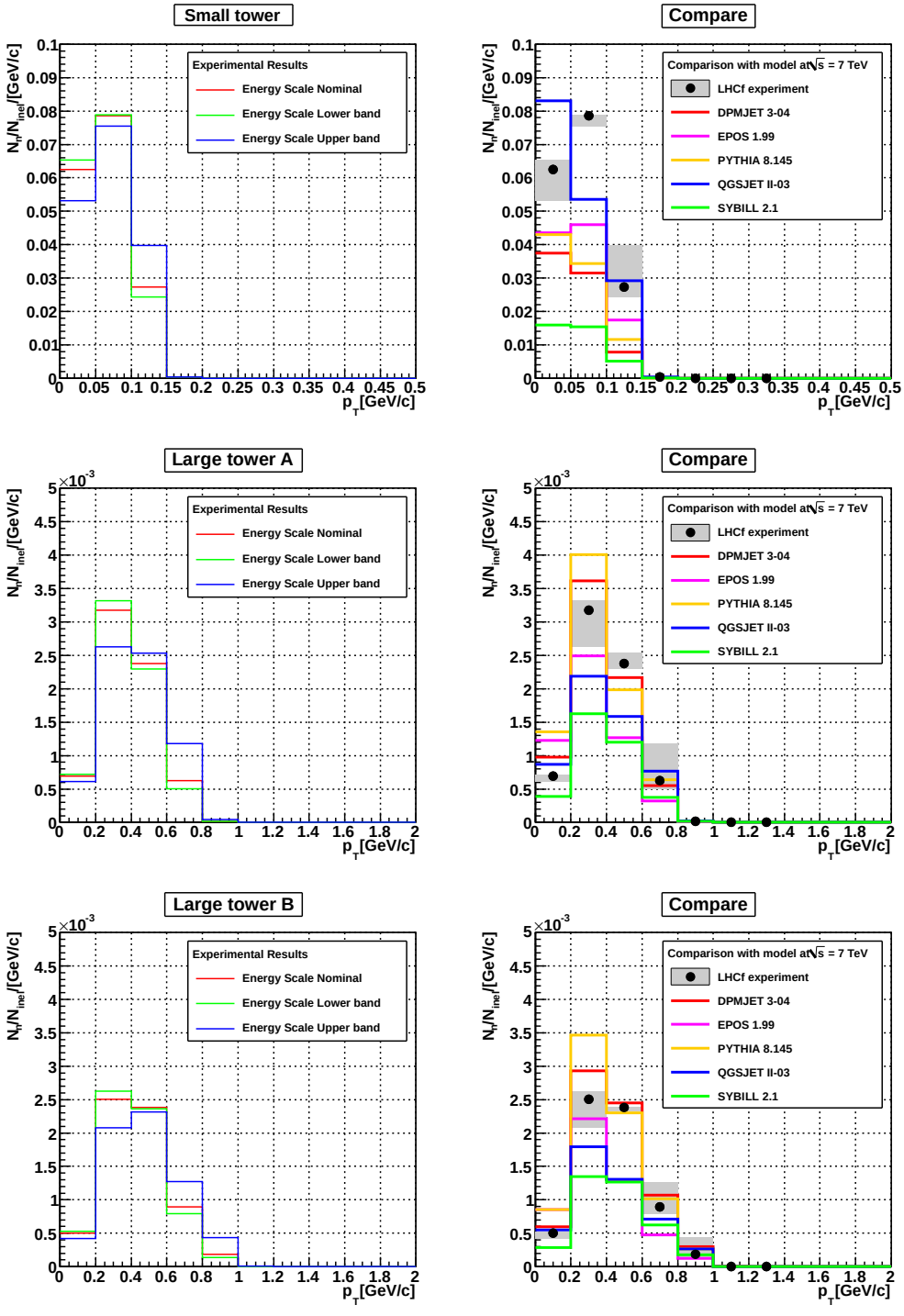

Figure 6.10: The p_T spectra for the pseudo-rapidity regions corresponding to the small tower, the large tower A and the large tower B. Only more than 500 GeV events were selected in this figure.

shower development was introduced as similar to [50]. In the calculation of air shower development, only hadronic particles were produced at interactions and electromagnetic cascades induced by photons from π^0 decay were considered. The number of air shower particles $N(E_0, t)$ as a function of vertical depth and cosmic-ray energy is well described by the Greisen formula [51];

$$N(E_0, t) = \frac{0.31}{\beta_0^{\frac{1}{2}}} \exp\left[t(1 - \frac{3}{2}\log s)\right], \tag{6.2}$$

where E_0 is the energy of the primary cosmic-ray, t is the vertical depth x divided by radiation length X_0 (about 36.7g/cm^2), s is called the age parameter defined as $s = 3t/(t + 2\beta_0)$, and $\beta_0 = \log E_0/\epsilon$ is the depth of shower maximum. ϵ called the critical energy of electromagnetic interaction in air and is about 80 MeV.

In this toy simulation, interactions by hadrons with energy of E_0 were assumed as following.

- Only protons were assumed to be primary cosmic-ray.
- Hadronic interaction with air nuclei occurs at every interaction length step.
- Charged and neutral pions were generated by the interactions according to a given x_F distribution with $\pi^{\pm} : \pi^0 = 2 : 1$.
- One leading baryon is also generated with energy of $(E_0 - E^{\pi}_{total})$, where E^{π}_{total} is the total energy carried by π mesons.
- Inelasticity k can be calculated as E^{π}_{total}/E_0.
- Neutral pions immediately decay into two photons with same energy.
- The interaction length and the x_F distribution of pions not depend on the collision energy.

The original x_F distribution was assumed by using DPMJET 3.04 model, and the inelasticity is calculated to be 0.50. Then the inelasticity was artificially modified according to the LHCf neutron results and shower development were simulated with the 10^{19} eV proton primaries. The left panel of Figure 6.11 shows the changes of shower transition shape for air shower by changing inelasticity. While the right panel shows the atmospheric depth X_{max} at which the number of shower particles reaches maximum as a function of inelasticity. The X_{max} value increasing as decreasing inelasticity. The X_{max} value for each inelasticity parameter is summarized in Table 6.4. The impact of the change of inelasticity in the X_{max} value is less than 40 g/cm^2.

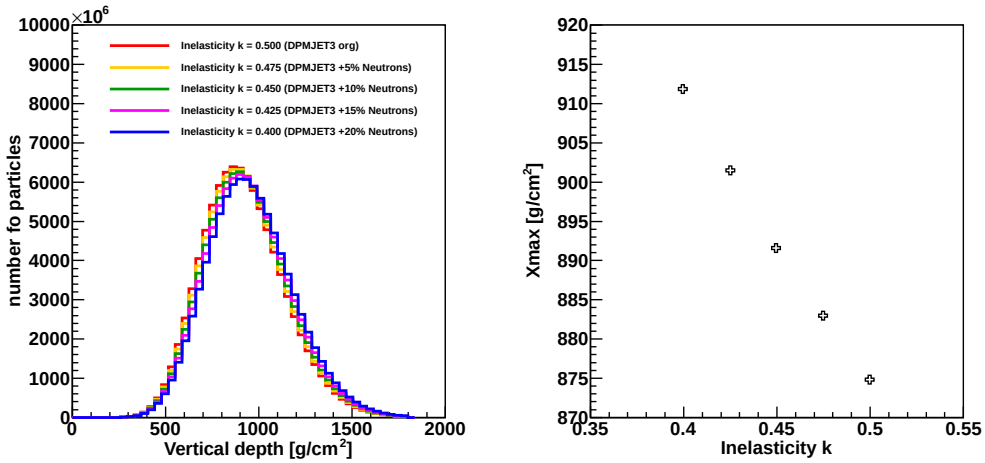

Figure 6.11: The left panel shows the number of particles as a function of vertical depth for each inelasticity value. The right panel represents X_{max} as a function of inelasticity.

Inelasticity k	X_{max} [g/cm^2]	Difference [g/cm^2]
0.500	874.8	-
0.475	883.0	8.15
0.450	891.6	16.8
0.425	901.5	26.7
0.400	911.8	37.0

Table 6.4: The X_{max} value for each inelasticity parameter obtained by the 1 dimensional Toy MC study.

6.5 Analysis summary

The first analysis results of the neutron spectra at the very forward rapidity of the LHC are presented in this thesis. The data used in this study were taken in May 2010 at the LHC $\sqrt{s} = 7$ TeV proton-proton collisions. The integrated luminosity of the data set are 0.68 nb^{-1} and 0.53 nb^{-1} for Arm1 and Arm2, respectively. The neutron candidate events were selected by the L_{2D} method developed in this study with more than 90% of purity for neutrons above 1 TeV. The consistent results from the two independent calorimeters of Arm1 and Arm2 were obtained in the three different rapidity regions. The experimental results were compared with the MC predictions of QGSJET II-03, EPOS 1.99, DPMJET 3.04, PYTHIA 8.145, and SYBILL 2.1. The experimental results indicated the highest neutron production rate compared with the MC models at the most forward rapidity and the QGSJET II-03 model predicted similar neutron production rate compared with the experiment at the small tower. On the other hand, PYTHIA 8.145 predicted neutron production rate similar to the experiment at the large towers. The measured spectra were unfolded by using the two dimensional unfolding method based on the Bayesian theory, and were also compared with the ISR and PHENIX results. The experimental results have a broad peak at $x_F = 0.6$ to 0.8 within the systematic errors. The LHCf results show similar results with the previous experiments considering the change of spectra by the choice of energy scale within the systematic uncertainty.

Chapter 7

Conclusion

Acceleration mechanism, origin, and propagation mechanism of ultra-high energy cosmic-rays "UHECRs" of which energy reach to 10^{20} eV are big mysteries in cosmic-ray physics. Owing to the huge cascade shower in the atmosphere developed by UHECRs, indirect measurement is possible at the ground. The hadronic interaction models play a very important roll in the interpretation of the measurements of cosmic-rays, and detail understanding of the particle production at the very forward region is essential to understand the development of cosmic-ray showers. However, the lack of knowledge on the forward particle productions in the energy region near UHECRs associates with a large uncertainty in the estimation of the energy and chemical composition of observed cosmic-rays in UHECR region.

Proton-proton collisions with the energy 10^{17} eV at laboratory frame is feasible at the LHC. The LHCf experiment is designed to verify these models using the LHC. We have verified hadronic interaction models used in air shower simulation of UHECRs by measurement of photon production at the very forward region of the LHC. Forward baryon production is one of the crucial point to understand the relationship between development of air showers and the hadronic interaction models. However, because the LHCf detectors are optimized for photon measurement, the performance for hadron measurement has not been studied in detail.

The performance of the LHCf detectors for hadronic showers were studied using 350 GeV proton test beams at CERN SPS and MC simulations for the first time. We compared the SPS experimental data with two different MC configurations using DPMJET 3.04 or QGSJET II-03 hadronic interaction models. The QGSJET II-03 model showed better agreement with the experimental test beam data. The 36% sumdE resolution of experimental data was consistent with the prediction of MC simulations. The energy scale was checked by comparing the sumdE distribution of the SPS data with the MC

simulations. The 3.5% (6.5%) difference in sumdE for Arm1 (Arm2) between the experimental result and the MC prediction with the QGSJET II-03 model were observed and further included as a part of systematic uncertainty. The detection efficiency was greater than 70% for neutrons above 500 GeV for both towers of the Arm1 and Arm2 detectors. The energy resolution was about 40% above 500 GeV weakly depending on energy. The linearity of the energy scale was achieved as $\pm$ 2%. The resolution of transverse hit position was less than 1 mm above 500 GeV and improved slowly with increasing the neutron energy.

In order to extract the true energy distribution from the measured energy spectra which was smeared by the finite detector response, two dimensional unfolding method based on the iterative Bayesian method was studied. The performance of the unfolding method with the flat training distribution was checked carefully by applying it to the MC spectra in consideration of full detector response. We observed the small training bias in the unfolded results owing to the difference of initial distributions between the training sample and the tested sample, and we confirmed that this bias did not strongly depend on the model. By applying bias correction determined from the average of the five models, the true energy distribution can be reconstructed with 20-60% accuracy depending on the energy.

We also analyzed the data taken in May 2010 at the LHC $\sqrt{s} = 7$ TeV proton-proton collisions. The integrated luminosity of the data set are 0.68 nb^{-1} and 0.53 nb^{-1} for the Arm1 and Arm2, respectively. The neutron events were selected by using the two dimensional PID selection method developed in this study with more than 90% purity to neutrons of the energy more than 1TeV. The neutron energy spectra were unfolded for its energy resolution and then compared in the three different rapidity regions with the MC predictions QGSJET II-03, EPOS 1.99, DPMJET 3.04, PYTHIA 8.145, and SYBILL2.1. No model can reproduce the experimental result perfectly. The experimental results show the most abundant neutron production compared with the known models at $\eta > 10.76$. Only the QGSJET II-03 model indicates similar energy spectra at $\eta > 10.76$. On the other hand, the some of the models show similar neutron production rate at $8.81 < \eta < 9.22$.

The performance of the LHCf detectors for neutron measurement has been confirmed in this study for the first time. It was also demonstrated that it is possible to verify the hadronic interaction models using the neutron energy spectrum obtained by LHCf.

Acknowledgments

First of all, I would like to thank my supervisor Prof. Yoshitaka Itow for giving me the opportunity of studying this work. He providing me the essential support for this thesis.

I would also express my sincere thanks to Prof. M. Harada, Prof. K. Masuda, Prof. H. Tajima and Prof. M. Tomoto for reviewing my thesis carefully and providing many valuable advice.

I would also like to thank the member of the LHCf collaboration. The experiment would not have succeeded without their efforts. I therefore thank Prof. O. Adriani, Prof. R. D'Alessandro, Prof. K. Masuda, Prof. T. Tamura, Prof. S. Torii, Prof. A. Tricomi, T. Sako, L. Bonechi, M. Bongi, S. Ricciarini, A-L. Perrot, and Prof. K. Kasahara, for their hard works. Especially, I wish to special thanks to Prof. Y. Muraki, T. Sako, H. Menjo, G. Mitsuka and W.C. Turner for taking time to give me many comments and helps. I would like to appreciate to T. Mase, K. Taki, T. Suzuki, K. Fukatsu, K. Suzuki, T. Iso, Y. Makino and E. Matsubayashi for helping my study.

Finally, I would like to express my greatest appreciation and gratitude to my family. I believe this thesis would never exist without supports of everyone.

Bibliography

[1] J.W. Cronin. Rev. Mod. Phys. **S165**, (1999).

[2] Blandford, R. D. & Eichler, D., Phys. Rep. **154**, 1 (1987).

[3] S. Swordy, U. Chicago, NASA, http://apod.nasa.gov/apod/ap060814.html (2006).

[4] J. Abraham, *et al.*, Phys. Rev. Lett., **101** 061101 (2008).

[5] H. Sagawa, *et al.*, AIPC, **1367**, 17-22 (2011).

[6] J. Abraham, *et al.*. Phys. Lett. B **685**, 239-246 (2010).

[7] R. Abbasi, *et al.*, Astropart. Phys., **32**, 53-60 (2009).

[8] K. Greisen, Phys. Rev. Lett., **16**, 17 748-749 (1966).

[9] G. T. Zatsepin, V. A. Kuz'min, Sov. Phys. JETP Lett. **4**, 78 (1966).

[10] J. Abraham, *et al.*, Phys. Rev. Lett., **104**, 091101 (2010).

[11] VN. Gribov, Sov. Phys. JETP **26**, 414 (1968).

[12] T. Regge, Nuovo Ciment, **14**, 951-976 (1959).

[13] F. W. Bopp, J. Ranft R. Engel and S. Roesler, Phys. Rev., **C77**, 014904 (2008).

[14] K. Werner, F.-M. Liu and T. Pierog, Phys. Rev., **C74**, 044902 (2006).

[15] T. Sjöstand, S. Mrenna and P. Skands, JHEP05, **026** (2006).

[16] T. Sjöstand, S. Mrenna and P. Skands, Comput. Phys. Comm., **178**, 852 (2008).

[17] S. Ostapchenko, Phys. Rev., **D74**, 014026 (2006).

[18] E.-J. Ahn, R. Engel, T. K. Gaisser, P. Lipari and T. Stanev, Phys. Rev., **D80**, 094003 (2009).

[19] TOTEM Technical Design Report, CERN-LHCC-2004-002 (2004).

[20] G. Antchev *et al.*, EPL, **96**, 21002 (2011).

[21] R. Ulrich, Phys. Rev. D, **83**, 054026 (2011).

[22] J. Allen, et al. Proceedings of 32nd ICRC, Beijin (2011).

[23] T. Pierog, K. Werner Phys. Rev. Lett. **101**, 171101 (2008).

[24] H.J. Drescher, *et al.*, Physics Reports, **350**, 93-289 (2001).

[25] A. Adare, et al., Phys. Rev. D, **88**, 032006 (2013).

[26] J. Engler et al., Nucl. Phys. B **84**, 70 (1975).

[27] W. Flauger and F. Mönnig, Nucl. Phys. B, **109**, 347-356 (1976).

[28] A. Ferrando, *et al.*, Nucl. Instrum. Meth. A **390**, 63-78 (1997).

[29] P. Goettlicher *et al.*, Nucl. Instrum. Meth. A **623**, 225 (2010).

[30] L. EvansBlandford, D., New Journal of Physics. **9**, 335 (2007).

[31] LHCf Technical Design Report, CERN-LHCC-2006-004 (2006).

[32] k. Taki, et al., JINST, 7, T01003 (2012).

[33] T. Mase, *et al.*, Nucl. Instrum. Meth. A **671**, 129-136 (2012).

[34] O. Adriani, *et al.*, JINST, **3**, S08006 (2008).

[35] T. Mase, Doctoral Thesis, (2012).

[36] O. Adriani, *et al.*, Phys. Lett. B, **703** 128-137 (2011).

[37] O. Adriani, *et al.*, Phys. Rev. D, **86**, 092001 (2012).

[38] O. Adriani, *et al.*, Phys. Lett. B, **715**, 298 (2012).

[39] K. Kawade, *et al.*, JINST **6** T09004 (2011).

[40] K. Kasahara, EPICS web page, http://cosmos.n.kanagawa-u.ac.jp/.

[41] O. Adriani, *et al.*, JINST, **5**, P01012.

[42] O. Adriani, et al., Int. J. Mod. Phys. **28.25** 1330036 (2013).

[43] L. Bonechi, *et al.*, Proceedings of 29th ICRC, Pune,**vol.9**, 283 (2005).

[44] G. D' Agostini, Nucl. Instrum. Meth. A **362**, 487 (1995).

[45] K. Nakamura, *et al.* (Particle Data Group), J. Phys. G**37**, 075021 (2010).

[46] K. Kawade, *et al.*, JINST **9**, P03016 (2014).

[47] R. Barlow and C. Beeston, Comp. Phys. Comm. **77** 219-228 (1993).

[48] G. Vismara, CERN-SL-2000-056 BI (2000).

[49] A. Capella, J. Tran Thanh Van, and J. Kaplan, Nucl. Phys. B **97**, 493 (1975).

[50] H. Menjo, Doctoral Thesis, (2009).

[51] K. Greisen, Prog. Cosmic Ray Physics 3, 1 (1956).

Appendix A

Multi-it selection method

The number of incident particle can be measured by the position sensors of the SciFi detector for the Arm1 and the Silicon detector for the Arm2. Figure A.1 shows a typical sample of multi-hit event. Two different peaks can be recognized in both the plots for the X (left) and Y (right) axis.

Multi-hit event reconstruction was carried out by searching two peak then fitting with Function A.1. A event was flagged as a multi-hit event when the power of secondary peak exceeds more than 10% of the primary peak;

$$f(x) = \frac{1}{2} \times \frac{C_1 \times C_3}{((x - C_2)^2 + C_1)^{\frac{3}{2}}} + \frac{1}{2} \times \frac{C_4 \times C_6}{((x - C_5)^2 + C_4)^{\frac{3}{2}}}, \tag{A.1}$$

where $C_2(C_5)$ and $C_3(C_6)$ describe the center and the power of primary(secondary) peak, respectively.

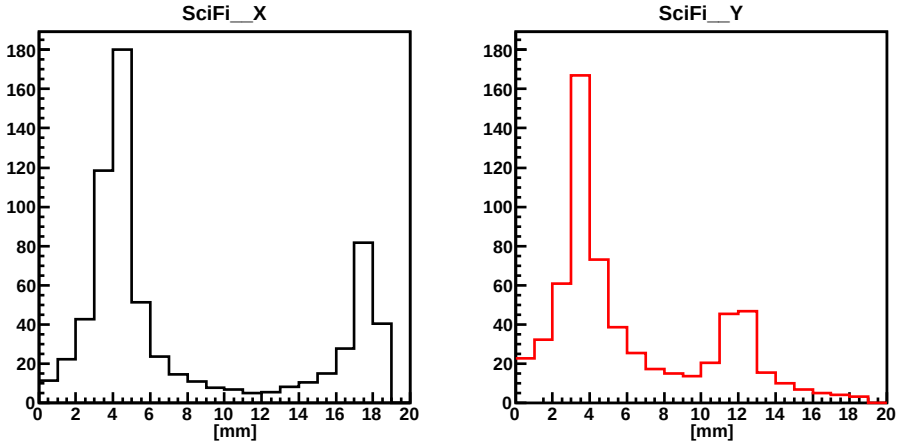

Figure A.1: A typical sample of SciFi hit map in multi hit event.